Fall 2016

Thermomechanical response of metal-ceramic graded composites for high-temperature aerospace applications

Phillip Eugene Deierling
University of Iowa

THERMOMECHANICAL RESPONSE OF METAL-CERAMIC GRADED COMPOSITES FOR HIGH-TEMPERATURE AEROSPACE APPLICATIONS

by

Phillip Eugene Deierling

A thesis submitted in partial fulfillment
of the requirements for the Doctor of Philosophy
degree in Mechanical Engineering in the
Graduate College of
The University of Iowa

December 2016

Thesis Supervisor: Professor Olesya I. Zhupanska

Graduate College
The University of Iowa
Iowa City, Iowa

CERTIFICATE OF APPROVAL

_____

PH.D. THESIS

_____

This is to certify that the Ph.D. thesis of

Phillip Eugene Deierling

has been approved by the Examining Committee for
the thesis requirement for the Doctor of Philosophy degree
in Mechanical Engineering at the December 2016 graduation.

Thesis Committee: _____
Olesya Zhupanska, Thesis Supervisor

_____
Shaoping Xiao

_____
Albert Ratner

_____
Jia Lu

_____
Salam Rahmatalla

To my family

ACKNOWLEDGEMENTS

I would like to express my sincere gratitude to my advisor, Professor Olesya Zhupanska, for her support, guidance and patience during my studies at The University of Iowa. The success of this dissertation and my future endeavors lie heavily on the encouragement received from her throughout our time together.

I would also like to thank the members of my dissertation committee, Professor Shaoping Xiao, Professor Albert Ratner, Professor Jia Lu and Professor Salam Rahmatalla for taking their valuable time to serve on this committee. Their advice has proven to be priceless during my academic and personal development.

A special thanks goes to Dr. Crystal Pasilliao for making this work possible and for her unwavering support during my research. For her patience, guidance and understanding throughout the development of this work I am forever indebted.

I would also like to express my gratitude to all of the members of the Air Force Research Laboratory Munitions Directorate for supporting this research. A special recognition goes to Dr. Lynn Neergaard, Zach Witeof and Dr. Daniel Reasor for their continuous backing and encouragement during this work.

Additionally, I would also like to thank all of the members of the Center for Computer-Aided Design for their support and kindness. I especially would like to thank Deborah Hampton, Jenny Simpson, Lisa Lang and Melanie Laverman for their aid and friendship.

Finally, deepest thanks to my family for their unwavering support during this and all of my undertakings. I especially thank my mom for instilling in me at a young age a desire for knowledge, encouraging me to always ask questions, continuing to support my education throughout my life and civility. These core values which I have obtained from her are principles that I will carry with me for the rest of my life and will strive to pass onto future generations.

ABSTRACT

Airframes operating in the hypersonic regime are subjected to complex structural and thermal loads. Structural loads are a result of aggressive high G maneuvers, rapid vehicle acceleration and deceleration and dynamic pressure, while thermal loads are a result of aerodynamic heating. For such airframes, structural members are typically constructed from steel, titanium and nickel alloys. However, with most materials, rapid elevations in temperature lead to undesirable changes in material properties. In particular, reductions in strength and stiffness are observed, along with an increase in thermal conductivity, specific heat and thermal expansion. Thus, hypersonic airframes are typically designed with external insulation, active cooling or a thermal protection system (TPS) added to the structure to protect the underlying material from the effects of temperature. Such thermal protection may consist of adhesively bonded, pinned and bolted thermal protection layers over exterior panels. These types of attachments create abrupt changes in thermal expansion and stiffness that make the structure susceptible to cracking and debonding as well as adding mass to the airframe.

One of the promising materials concepts for extreme environments that was introduced in the past is the so-called spatially tailored advanced thermal structures (STATS). The concept of STATS is rooted in functionally graded materials (FGMs), in which a directional variation of material properties exists. These materials are essentially composites and consist of two or more phases of distinct materials in which the volume fractions of each phase continuously change in space. Here, the graded material will serve a dual-purpose role as both the structural/skin member and thermal management with the goal of reducing the weight of the structure while maintaining structural soundness. This is achieved through the ability to tailor material properties to create a desired or enhanced thermomechanical response through spatial variation (e.g., grading).

The objective of this study is to present a computational framework for modeling and evaluating the thermomechanical response of STATS and FGMs for highly

maneuverable hypersonic (Mach > 5) airframes. To meet the objective of this study, four key steps have been defined to study the thermomechanical response of such materials in extreme environments. They involve: (1) modeling of graded microstructures; (2) validation of analytical and numerical modeling techniques for graded microstructures; (3) determination of effective properties of variable composition composites; (4) parametric studies to evaluate the performance of FGMs for use in the hypersonic operating environment; and (5) optimization of the material spatial grading in hypersonic panels aiming to improve the thermomechanical performance.

Modeling of graded microstructures, representing particulate reinforced FGMs, has been accomplished using power law distribution functions to specify the spatial variation of the constituents. Artificial microstructures consisting of disks and spheres have been generated using developed algorithms. These algorithms allow for the creation of dense packing fractions up to 0.61 and 0.91 for 2D and 3D geometry, respectively.

Effective properties of FGMs are obtained using micromechanics models and finite element analysis of representative volume elements (RVEs). Two approaches have been adopted and compared to determine the proper RVE for materials with graded microstructures. In the first approach, RVEs are generated by considering regions that have a uniform to slow variation in material composition (i.e., constant volume fraction), resulting in statistically homogenous piecewise RVEs of the graded microstructure neglecting interactions from neighboring cells. In the second approach, continuous RVEs are generated by considering the entire FGM. Here it is presumed that modeling of the complete variation in a microstructure may influence the surrounding layers due to the interactions of varying material composition, particularly when there is a steep variation in material composition along the grading direction. To determine these effects of interlayer interactions, FGM microstructures were generated using three different types of material grading functions—linear, quadratic and square root—providing uniform, gradual and steep variations, respectively. Two- and three-dimensional finite element

analysis was performed to determine the effective temperature-dependent material properties of the composite over a wide temperature range. The outcome of the computational analysis shows that the similar effective properties are obtained by each of the modeling approaches. Furthermore, the obtained computational results for effective elastic, thermal and thermal expansion properties are consistent with the known analytical bounds.

The resulting effective temperature-dependent material properties were used to evaluate the time-dependent thermostructural response and effectiveness of FGM structural panels. Structural panels are subjected to time- and spatial-dependent thermal and mechanical loads resulting from hypersonic flight over a representative trajectory. Mechanical loads are the by-product of aggressive maneuvering at high air speeds and angles of attack. Thermal loads as a result of aerodynamic heating are applied to the material systems as laminar, turbulent and transitional heat flux on the outer surface. Laminar and turbulent uniform heat fluxes are used to evaluate the effectiveness of FGM panels graded in the through-thickness direction only. Transitional heat fluxes are used to evaluate the effectiveness of FGMs graded in two principal directions, e.g., through-thickness and the surface parallel to flow. The computational results indicate that when subjected to uniform surface heat flux, the graded material system can eliminate through-thickness temperature gradients that are otherwise present in traditional thermal protection systems. Furthermore, 2D graded material systems can also eliminate through-thickness temperature gradients and significantly reduce in-plane surface temperature gradients when subjected to non-uniform surface aerodynamic heating.

PUBLIC ABSTRACT

Aircraft operating in the hypersonic regime are subjected to complex thermal and structural loads. Airframes operating in this environment are typically constructed from structural materials protected from the effects of temperature by a thermal protection system (TPS) that is chemically or mechanically bonded over structural panels which can make structures susceptible to cracking and debonding. Thus the design of next-generation agile hypersonic airframes demands advanced materials capable of operating in extreme environments.

One promising material concept for extreme environments that was recently introduced is the idea of spatially tailored advanced thermal structures (STATS). The notion of STATS finds its roots in functionally graded materials (FGMs), in which spatial dependence of material properties exists. Particularly, metal-ceramic graded structures find novel applications as multifunctional thermostructural members through tailoring material properties to create desirable or enhanced thermostructural responses.

In the present thesis, a computational framework for modeling and evaluating the thermomechanical response of STATS for highly maneuverable hypersonic airframes is presented. The framework is formulated around the coupling of effective property estimation, thermostructural analysis and optimization. Numerical models based on micromechanical methods are used to confidently predict effective temperature- and spatial-dependent material properties. Using representative hypersonic loads, the thermostructural response is determined using finite element analysis (FEA) over a characteristic trajectory. Lastly, using surrogate modeling techniques, optimal material distribution is determined using optimization techniques to produce a minimum mass system capable of withstanding the extreme operating requirements.

TABLE OF CONTENTS

LIST OF TABLES

LIST OF FIGURES

CHAPTER 1

INTRODUCTION

1.1 Background and Motivation

Recent interest in high-speed intercept missiles and fast-response weapons operating in the hypersonic regime has resulted in considerable effort on the development of airframes capable of operating in this environment. One of the most difficult engineering challenges facing such development is the complex coupling of the fluid-thermal-structural interactions (FTSI) taking place at such high speeds [1]. In such flow fields, extreme temperatures are generated on the vehicle surface as a result of aerodynamic heating, while aerodynamic pressure places substantial external loading on the airframe structure. Moreover, highly maneuverable vehicles generate additional structural loads with aggressive trajectories, rapid acceleration and deceleration and erratic corrections in trajectory. As a result, a highly non-linear coupled thermomechanical response is generated. In current systems, the design engineering must rely on traditional materials, structural and thermal, to create structures capable of operating in such harsh environments. To bear the brunt of structural loads imposed on the airframe at these airspeeds, steel, titanium and nickel alloys are popular choices due to their high strength and temperature tolerance. However, with most materials, rapid elevations in temperature lead to undesirable changes in material properties. In particular, reductions in strength and stiffness are observed, along with an increase in thermal conductivity, specific heat and thermal expansion. To combat these issues, a thermal protection system (TPS) or a thermal barrier coating (TBC) is used to protect and/or mitigate the underlying material from the effects of temperature.

Common materials for TPSs and TBCs are ceramics, carbon-carbon (C/C) composites and syntactic foams, bonded, laminated or mechanically fastened to the

underlying skin material. While thermal ceramics have high stiffness and temperature tolerance, these desirable characteristics come at the expense of high density. Light-weight C/C composites also have high service temperatures but have poor insulation efficiency. Lastly, syntactic foams, particularly silicone-based ones, have low density, high operating temperature and high insulation efficiency, but provide little to no structural value to airframes. Moreover, because TPSs/TBCs are layered onto the skin surface, a strong discontinuity exists on the interfacial layer between the two materials. This discontinuity can give rise to stress concentrations as a result of large differences in the material's thermal expansion and elastic properties, resulting in an overdesigned structure, increased weight, reduced performance, decrease in service life, etc. Therefore, efficient operation in this environment requires materials capable of withstanding extreme thermal and structural environments. Ideal materials would possess combinations of desirable characteristics from structural materials as well as thermal TPS/TBC materials.

A material concept recently introduced to meet these desirable material characteristics for airframes operating in this extreme environment is spatially tailored advanced thermal structures (STATS) [2]. The concept of spatial tailoring is rooted in the notion of functionally graded materials (FGMs), in which directional variation of material properties (typically in one direction) exists. FGMs are a unique class of heterogeneous composite materials consisting of at least two phases, in which the volume fraction of each phase continuously varies in space. This unique attribute makes FGMs ideal material candidates for structures relying on traditional TPSs/TBCs, by combining the attributes of structural and thermal materials and reducing large differences in constituent material parameters. Furthermore, FGMs provide the capability to tailor the macroscopic structural response via spatial variation (i.e., grading) in the materials properties. Here a desired or enhanced structural response can be achieved using information about the anticipated thermal and structural loads. For example, in hypersonic applications, in

addition to the high through-thickness thermal gradients and structural loads, interaction of the flow field with skin surfaces results in non-uniform temperature distribution parallel to the flow field. Thus, further optimization of the airframe is possible with 2D and 3D continuous grading of the material by improving the thermal and structural properties of the structure.

1.2 Objectives of the Proposed Study

The primary objective of this study is to develop a computational framework for modeling and evaluating the thermomechanical response of FGMs for highly maneuverable hypersonic airframes. To meet the proposed objective four major research hurdles have been defined. They involve: (1) modeling of graded microstructures; (2) validation of analytical and numerical modeling techniques for graded microstructures; (3) determination of effective properties of variable composition composites; (4) parametric studies to evaluate the performance of FGMs for use in the hypersonic operating environment; (5) optimization of the material spatial grading in hypersonic panels aiming to improve the thermomechanical performance.

1.3 Organization of the Thesis Proposal

The thesis proposal is organized as follows. CHAPTER 2 presents a literature review on existing micromechanical theories, models and methods for predicting the effective elastic, thermoelastic and thermal properties of traditional composite materials. These material models are useful in establishing approximations as well as bounds on the overall effective composite material parameters.

CHAPTER 3 provides details on the mathematical modeling of FGMS needed for future analysis and direct applications. Here, mathematical representations of the continuous graded microstructures are defined for material variation in one and two dimensions.

CHAPTER 4 lays out a computational framework for determining the effective material properties of heterogeneous composite materials. This framework involves determining a proper definition for the representative volume element (RVE) for graded microstructures. This in-depth analysis involves comparing effective properties estimated by several numerical models to determine the effect of grading on the effective properties and the influence of particle interactions on the homogenization of the material response. Additionally, the hypothesis of using conventional micromechanical models for predicting the effective properties of traditional fixed volume fraction composites is examined. The obtained effective properties are verified using rigorous analytical methods and verified by means of experimentally obtained data available in the literature. Also, a numerical study is performed on the assumption of the transition zone of the two-phase graded composite system. This study aims to evaluate the local effective material properties of graded structures when information regarding the evolution of the material grading is not readily available. Finally, the two-phase framework is extended to three-phase composites (reinforcement, matrix and porosity) to investigate the effects of porosity or voids on the effective material response.

CHAPTER 5 provides parametric studies to evaluate the performance of FGMs for use as a multifunctional TPS/TBC and structural member operating in the hypersonic environment. This analysis begins with establishing a thermal and thermomechanical benchmark for a typical TPS/skin material system for a generic monocoque hypersonic missile over a representative flight trajectory. This benchmark consists of a titanium (Ti-6Al-4V) skin and Excelis Acusil® II TPS subjected to thermal and structural loads. The thermal and structural response of the system is then compared to that of varying material systems graded in the through-thickness direction only. Parametric studies are performed to evaluate material grading parameters and to evaluate the influence of grading on the thermostructural response. The analysis is also extended to include the effects of non-uniform in-plane surface temperatures by simulating the effects of a laminar to turbulent

(transitional) boundary layer. This simulation allows for the evaluation of the effects of 2D material grading on the thermostructural response. Using the aforementioned modeling technique, a series of constrained optimization analyses are performed to illustrate the potential for performance improvement by implementing spatially tailored materials into the thermostructural design.

CHAPTER 2

HOMOGENIZATION THEORIES AND METHODS: LITERATURE REVIEW

2.1 Homogenization Background

The aim of this chapter is to provide a review of some of the homogenization techniques developed for use with classical composite materials. The review is organized to include the following analytical and semi-analytical homogenization topics: (1) Effective elasticity, (2) Effective thermoelasticity, (3) Effective thermal conductivity and (4) Effective specific heat. While there exists a plethora of proposed models and theories in relevant literature, only a few directly relevant to the current study will be presented.

2.2 Theoretical Bounds on Elastic Constants

2.2.1 Analytical and Semi-Analytical Approaches

The estimation of effective elastic material constants has been by far the most widely investigated aspect of composite materials. The effective elastic constants are crucial to the design of structures and systems with composite materials. Many analytical and semi-analytical models have been developed with the aim of evaluating the effective elastic properties of different types of heterogeneous composites. In the case of most of the following methods, the bulk and shear elastic moduli are determined. For most practical applications, the Young's modulus or elastic modulus is the material constant of interest. Here, the Young's modulus, *E*, is determined through the well-known relation

$$E = \frac{9KG}{3K + G} \tag{2.1}$$

were *K* and *G* are the bulk and shear modulus, respectively.

2.2.2 Mixture Rules: Voigt and Reuss Bounds

Voigt [3] is typically credited with the earliest study of the effective mechanical properties of composite materials in 1889. Voigt assumed that the strain field in the composite was uniform throughout the material, leading to an average elastic tensor $\boldsymbol{C}$. Nearly 40 years later, Reuss [4] provided a complementary contribution to the work of Voigt on the subject matter. Reuss assumed that the stress field in the composite was uniform throughout, leading to an average compliance tensor $\boldsymbol{S}$. The Voigt estimation for the effective elastic tensor $\boldsymbol{C}^*$ is given by

$$\boldsymbol{C}^* = \sum_{i=1}^{N} \phi_i \boldsymbol{C}_i, \tag{2.2}$$

where $\boldsymbol{C}_i$ and ϕ_i are the elastic tensor and volume fraction of the i-th phase, respectively. Similarly, the Reuss estimation for the effective compliance tensor $\boldsymbol{S}^*$ is given by

$$\boldsymbol{S}^* = \sum_{i=1}^{N} \phi_i \boldsymbol{S}_i, \tag{2.3}$$

where $\boldsymbol{S}_i$ is the compliance tensor of the i-th phase and $\boldsymbol{S}_i = \boldsymbol{C}_i^{-1}$. Later, in 1952, Hill [5] provided a significant contribution by proving that the arithmetic mean of Voigt and the harmonic mean of Reuss are the theoretical maximum and minimum potential effective properties. Thus, Voigt and Reuss are taken as the upper and lower bounds, respectively, for the effective elastic constants. These bounds are often, and in this document will be, referred to as the rule-of-mixtures (ROMs). Additionally, Hill provided an estimation of the effective property, by considering the average of the Voigt and Reuss approximations.

2.2.3 Theoretical Bounds of Hashin and Shtrikman

A fundamental shortcoming of the ROMs occurs when the elastic properties begin to differ by an order of magnitude or more (e.g., the stiffness of carbon fiber compared to a polymer matrix in carbon fiber polymer matrix composites). In this case, the bounds become quite wide, and estimation of the effective properties becomes problematic. Tighter bounds for linear elasticity were proposed by Hashin and Shtrikman [6] based on variational principles of the strain energy. They consider the minimum potential energy and the minimum complementary potential energy of the system. The bounds are asymptotic and are the tightest bounds for composites with isotropic phases when information about the geometry and distribution of the microstructure is not known. Furthermore, the bounds assume that the mixture of phases is statistically homogenous, and that there is perfect bonding between the matrix and reinforcement. For a multi-phase composite, the Hashin and Shtrikman (H-S) bounds for the effective elastic properties are calculated as follows:

$$K_1^* = K_1 + \frac{A_1}{1+\alpha_1 A_1}, \qquad K_2^* = K_n + \frac{A_n}{1+\alpha_n A_n}, \tag{2.4}$$

where

$$\alpha_1 = -\frac{3}{3K_1 + 4G_1}, \quad \alpha_n = -\frac{3}{3K_n + 4G_n}, \tag{2.5}$$

$$A_1 = \sum_{r=2}^{r=n} \frac{\phi_r}{\frac{1}{K_r - K_1} - \alpha_1}, \quad A_n = \sum_{r=1}^{r=n-1} \frac{\phi_r}{\frac{1}{K_r - K_n} - \alpha_n}, \tag{2.6}$$

resulting in the bulk modulus bounds

$$K_1^* < K < K_2^*, \tag{2.7}$$

where $K_1^*$and K_2^* are the lower and upper bounds of the bulk modulus K for the system with K_1 and K_n representing the minimum and maximum bulk modulus of the constituents, while n is the number of phases in the system. For the same multi-phase composite, the effective shear modulus is calculated using the minimum and maximum material phase shear modulus values G_1 and G_n, respectively. The resulting shear modulus bounds are as follows:

$$G_1^* = G_1 + \frac{1}{2}\left(\frac{B_1}{1+\beta_1 B_1}\right), \quad G_2^* = G_2 + \frac{1}{2}\left(\frac{B_n}{1+\beta_n B_n}\right), \tag{2.8}$$

where

$$\beta_1 = -\frac{3(K_1+2G_1)}{5G_1(3K_1+4G_1)}, \quad \beta_n = -\frac{3(K_n+2G_n)}{5G_n(3K_n+4G_n)}, \tag{2.9}$$

$$B_1 = \sum_{r=2}^{r=n} \frac{\phi_r}{\frac{1}{2(G_r-G_1)} - \beta_1}, \quad B_n = \sum_{r=1}^{r=n-1} \frac{\phi_r}{\frac{1}{2(G_r-G_n)} - \beta_n}, \tag{2.10}$$

resulting in the shear modulus bounds

$$G_1^* < G < G_2^*. \tag{2.11}$$

It has been shown that K_1^* is the exact result for the effective bulk modulus for a two-phase composite $(n = 2)$, in which a matrix first-phase is embedded with a spherical inclusion second-phase material distributed in a particular way. In a similar fashion, K_2^* is

the exact result when spherical inclusions of the first phase are embedded in a matrix comprised of the second-phase material. The same proof also applies to the effective shear modulus of the same two-phase system in which G_1^* or G_2^* is the exact result. For this two-phase composite, the effective elastic moduli are calculated using $n = 2$ in Eqs. (2.4-2.10). The resulting bounds for the effective bulk modulus are:

$$K_1^* = K_1 + \frac{\phi_2}{\frac{1}{K_2 - K_1} + \frac{3\phi_1}{3K_1 + 4G_1}}, \quad K_2^* = K_2 + \frac{\phi_1}{\frac{1}{K_1 - K_2} + \frac{3\phi_2}{3K_2 + 4G_2}} \tag{2.12}$$

and the effective shear modulus bounds are

$$G_1^* = G_1 + \frac{\phi_2}{\frac{1}{G_2 - G_1} + \frac{6(K_1 + 2G_1)\phi_1}{5G_1(3K_1 + 4G_1)}}, \tag{2.13}$$

$$G_2^* = G_2 + \frac{\phi_1}{\frac{1}{G_1 - G_2} + \frac{6(K_2 + 2G_2)\phi_2}{5G_2(3K_2 + 4G_2)}}.$$

The two-phase composite bounds of Eqs. (2.12) and (2.13) provide the tightest possible bounds for general isotropic materials without restrictions on the geometry of the microstructure.

2.2.4 Self-Consistent Model

The self-consistent method (SCM) is typically credited to Hill [7] and Budiansky [8], who were focusing on spherical particles and aligned fibers. In this scheme, the effective properties are determined by approximating the interactions among the constituents by those between the constituent and the homogenized composite. Simply put, the model assumes that the effective material properties are determined by the stress and strain states of the material surrounding one inclusion. The stress and strain fields are

assessed based on a single inclusion solution assuming that the inclusion is embedded in the matrix with unknown effective elastic constants. As shown by Lydzba [9], the SCM hydrostatic components of the strain localization tensor for the n-th phase $\boldsymbol{A}_{n,H}^{SC*}$ can be written as:

$$\boldsymbol{A}_{n,H}^{SC*} = \frac{K^* + \frac{4}{3}G^*}{K^n + \frac{4}{3}G^*}, \tag{2.14}$$

where K^n is the bulk modulus of the n-th phase and K^* and G^* are the bulk and shear moduli of the homogenized composite. Equation (2.14) must be satisfied for all components of the strain tensor $\langle \boldsymbol{\epsilon} \rangle^0$, resulting in:

$$\sum_{n=1}^{N} \phi_n (\boldsymbol{C}^* - \boldsymbol{C}_n) \boldsymbol{A}_n^{SC*} = 0. \tag{2.15}$$

For a macroscopically isotropic medium, Eq. (2.15) can be reduced to

$$\sum_{n=1}^{N} \phi_n (K^* - K_n) \boldsymbol{A}_{n,H}^{SC*} = 0. \tag{2.16}$$

$$\sum_{n=1}^{N} \phi_n (G^* - G_n) \boldsymbol{A}_{n,S}^{SC*} = 0. \tag{2.17}$$

Equations (2.16) and (2.17) create a non-linear system of equations to determine the effective homogenized bulk modulus K^* and shear modulus G^*. When spherical inclusion geometry is introduced into the above system, Eqs. (2.16) and (2.17) can be reduced to

$$\sum_{n=1}^{N} \phi_n \frac{(K^* - K_n)}{K_n + \frac{4}{3}G^*} = 0. \tag{2.18}$$

$$\sum_{n=1}^{N} \phi_n \frac{(G^* - G_n)}{G_n + \frac{G^*(9K^* + 8G^*)}{6(K^* + 2G^*)}} = 0. \tag{2.19}$$

This non-linear set of equations can be solved in an iterative process to determine the effective elastic constants. For reference, the strain localization tensors used in the Self-Consistent scheme have been tabulated by Lydzba [9] for spherical, needle and disk geometry.

2.3 Theoretical Bounds on Thermal Expansion

2.3.1 Coefficients of Thermal Expansion

For the most part, natural materials tend to expand when heated, which is referred to as thermal expansion. Thermal expansion on the macro scale is commonly defined as the change in a material's size as a result of a change in temperature. The linear coefficient of thermal expansion (CTE) is defined as:

$$\alpha_{ij} = \frac{\partial \epsilon_{ij}}{\partial T}, \tag{2.20}$$

where the strain, ϵ_{ij}, and CTE, α_{ij}, are second-order symmetric tensors and T is the temperature. Over a small differential temperature ΔT, the strain is typically taken as directly proportional to the CTE, and the constitutive thermo-mechanical relationship between the stress σ and strain ϵ and temperature change ΔT is given by:

$$\sigma_{ij} = \boldsymbol{C}_{ijkl}\epsilon_{ij} - \boldsymbol{C}_{ijkl}\alpha_{kl}\Delta T, \tag{2.21}$$

with $\boldsymbol{C}_{ijkl}$ containing the components of the fourth-order stiffness tensor.

2.3.2 Analytical and Semi-Analytical Approaches

The estimation of effective thermal properties of composite materials has been rigorously studied for many years. Many analytical and semi-analytical models have been developed with the aim of evaluating the effective coefficient of thermal expansion of different types of composite materials. Some of these models are restricted to composites made from isotropic phases [10-12], while others are developed with a more general approach [13, 14]. A few of these models that take into consideration the volume fraction and material properties of each phase are briefly discussed in the following sections.

2.3.3 Mixture Rules of Voigt and Reuss

In this case, the ROM is used as a first order-approximation of the effective CTE. The ROM models for CTE are extensions of the early Voigt and Reuss expressions for the estimation of the effective elastic moduli. Voigt and Reuss approximations are derived by assuming a uniform strain and stress, respectively. The Voigt approximation for the effective thermal expansion coefficient is given by:

$$\alpha_V^* = \frac{\langle E\alpha \rangle}{\langle E \rangle} = \frac{\phi_1 E_1 \alpha_1 + \phi_2 E_2 \alpha_2}{\phi_1 E_1 + \phi_2 E_2}, \tag{2.22}$$

where ϕ_i and α_i are the volume fraction and the coefficients of thermal expansion of the single isotropic phases of the composite, respectively, and E_i is the Young's modulus of the *i*-th phase. The Reuss approximation is defined as:

$$\alpha_R^* = \langle \alpha \rangle = \phi_1 \alpha_2 + \phi_2 \alpha_1. \tag{2.23}$$

The Voigt and Reuss approximations, Eqs. (2.23) and (2.22), respectively, are typically taken as the extreme bounds of the effective thermal expansion. While these bounds are some of the earliest and simplest, they are generally regarded as a poor approximation of the effective CTE. This is particularly emphasized when the material properties of the constituent materials differ greatly.

2.3.4 Turner Model

In 1946, Turner [10] developed a model for estimating the effective CTE based on the assumption that all phases in the composite have the same change in dimension and rate of change due to increased temperature. By assuming that shear deformation is negligible, equilibrium force balance gives rise to the first-order approximation given by:

$$\alpha_T^* = \frac{\langle K\alpha \rangle}{\langle K \rangle} = \frac{\phi_1 K_1 \alpha_1 + \phi_2 K_2 \alpha_2}{\phi_1 K_1 + \phi_2 K_2}, \tag{2.24}$$

where K_i is the bulk modulus of the *i*-th phase.

2.3.5 Schapery Model

Using thermoelastic energy principles, Schapery [13] derived upper and lower bounds for the effective CTE. The derivation assumes a composite made up of *n* phases, each of which has isotropic mechanical and thermal properties with the bounds $\alpha_S^{L*} \leq \alpha^* < \alpha_S^{U*}$ given as:

$$\begin{matrix}\alpha_S^{U*}\\ \alpha_S^{L*}\end{matrix}\} = \frac{1}{\langle 1/K\rangle - 1/\langle K\rangle}\{\langle\alpha\rangle\left(\frac{1}{K^*} - \frac{1}{\langle K\rangle}\right) + \frac{\langle K\alpha\rangle}{\langle K\rangle}\left(\langle\frac{1}{K}\rangle - \frac{1}{K^*}\right) \pm \phi\left(\langle\frac{1}{K}\rangle - \frac{1}{K^*}\right)^{\frac{1}{2}}\left(\frac{1}{K^*} - \frac{1}{\langle K\rangle}\right)^{\frac{1}{2}}\} \tag{2.25}$$

where

$$\phi = \left\{\left(\langle\frac{1}{K}\rangle - \frac{1}{\langle K\rangle}\right)\left(\langle K\alpha^2\rangle - \frac{\langle(K\alpha)^2\rangle}{\langle K\rangle}\right) - \left(\langle\alpha\rangle - \frac{\langle K\alpha\rangle}{\langle K\rangle}\right)^2\right\}^{1/2} \tag{2.26}$$

In the above equation, K^* is the effective composite bulk modulus, which can be determined using a variety of analytical approximations, bounds or experimentally obtained values. In the case of an isotropic two-phase composite, the bounds of Eq. (2.25) are reduced to

$$\alpha_S^{L*} = \alpha_2 + \frac{K_2}{K^U}\frac{(K_1 - K^U)(\alpha_2 - \alpha_1)}{(K_1 - K_2)} \tag{2.27}$$

and

$$\alpha_S^{U*} = \alpha_2 + \frac{K_2}{K^L}\frac{(K_1 - K^L)(\alpha_2 - \alpha_1)}{(K_1 - K_2)}. \tag{2.28}$$

Here α_S^{L*} and α_S^{U*} are the upper and lower Schapery bounds for the effective CTE, respectively, and K^U and K^L refer to the upper and lower bounds for the composite bulk modulus, respectively. Moreover, the second-order Schapery effective CTE bounds rely

on estimations of the effective bulk modulus. In these cases, a better prediction of the bulk modulus results in tighter bounds for the effective composite CTE. However, when disregarding geometric effects, the tightest bounds are created when using the bulk modulus bounds calculated by Hashin and Shtrikman as provided in Eq. (2.12).

2.3.6 Self-Consistent Approximation

In addition to the self-consistent scheme for effective elastic properties, Budiansky [15] in 1970 provided a self-consistent equivalent medium approach to the effective thermal expansion. For a composite mixture of *N* isotropic phases, the effective thermal expansion, α_{SC}^{*} is given by

$$\alpha_{SC}^{*} = \sum_{i=1}^{N} \phi_i \frac{\alpha_i K_i}{K^*} \left[1 - a + a\left(\frac{K_i}{K^*}\right)\right]^{-1} \tag{2.29}$$

where K^* is the effective bulk modulus of the mixture and a is defined as

$$a = \frac{1}{3}\left(\frac{1+\nu^*}{1-\nu^*}\right) \tag{2.30}$$

with the effective Poisson's ratio ν^* defined with the well-known relation

$$\nu^* = \frac{3K^* - 2G^*}{6K^* + 2G^*}. \tag{2.31}$$

Here, G^* is the effective shear modulus of the composite. In this formulation, K^* and G^* are calculated solving Eqs. (2.18) and (2.19).

2.4 Theoretical Bounds on Thermal Conductivity

2.4.1 Thermal Conductivity

Thermal conductivity is the ability of a material to transfer heat. Materials for thermal applications are selected based on their thermal conductivity. For instance, a heat sink for a computer processing unit (CPU) is designed to extract heat from the CPU to prevent overheating of the silicone transistors. Using materials that can absorb heat readily, such as copper and aluminum, results in an optimal design. On the other hand, TPSs for aerospace vehicles rely on the ability to resist heat flow through the thickness and transverse directions of the structure. Here, materials with low thermal conductivity are chosen (e.g., ceramics). The thermal conductivity k is used in the definition of Fourier's law

$$q = -k\nabla T, \tag{2.32}$$

where q is the heat flux density vector, ∇T is the temperature gradient and k is the second-order thermal conductivity tensor.

2.4.2 Analytical and Semi-Analytical Approaches

For the work presented here, the thermal conductivity is of particular interest as this property has significant impact on the coupled thermo-mechanical response of systems. In the following sections, a few models of the effective thermal conductivity of composite materials will be provided.

2.4.3 Mixture Rules of Wiener

As with other effective properties of composites, the ROM is used as a first-order approximation. However, in the case of thermal conductivity, credit is given to Wiener

[16] for the volume-weighted arithmetic and harmonic mean as opposed to the analogous elasticity ROMs [3, 4]. As with the Voigt and Reuss bounds for the effective elastic properties, the Wiener ROM bounds for the effective thermal conductivity are valid for arbitrary microstructures. The upper, k_W^{U*}, and lower, k_W^{L*}, Wiener bounds for a two-phase mixture are

$$k_W^{U*} = \langle k \rangle = \phi_1 k_1 + \phi_2 k_2 \tag{2.33}$$

and

$$k_W^{L*} = \frac{k_1 k_2}{\phi_1 k_2 + \phi_2 k_1}, \tag{2.34}$$

where k_i is the thermal conductivity of the *i*-th phase.

2.4.4 Bruggeman Model

Self-consistent schemes or effective medium approximations were first proposed by Bruggeman [17] and Landauer [18] in 1935 and 1952, respectively, and later generalized into the self-consistent framework by Hashin [19] in 1968. Bruggeman developed a model based on the implicit relationship between the thermal conductivities of the composite, the reinforcement and matrix. The theory is based on the self-consistent concept that the inclusion material can be regarded as being surrounded by an equivalent homogenous material whose properties are unknown and need to be determined. For a mixture of thermally isotropic materials (spherical inclusions) with interaction between particles, the approximation is given as

$$\phi_1 \left(\frac{k_1 - k_{SC}^*}{k_1 + 2k_{SC}^*} \right) + \phi_2 \left(\frac{k_2 - k_{SC}^*}{k_2 + 2k_{SC}^*} \right) = 0, \tag{2.35}$$

where k_{SC}^{*} is the self-consistent effective conductivity approximation.

2.4.5 Hashin and Shtrikman Model

Using variational methods on the principles of magnetic energy, Hashin and Shtrikman [20] developed rigorous bounds for the effective magnetic permeability. The analysis does not take into consideration geometry, only information on phase material and volume fraction. Additionally, the derivation considers the phase materials to be macroscopically homogenous and isotropic. Moreover, because of the mathematical analogy, the results can also be translated to the dielectric constant, electrical and thermal conductivity, and diffusivity for such systems. The H-S thermal conductivity bounds where $k_{HS}^{L*} \leq k^{*} < k_{HS}^{U*}$ for a multi-phase composite where k_1 and k_m are the smallest and largest values of k in the composite are given as:

$$k_{HS}^{L*} = k_1 + \frac{A_1}{(1 - \alpha_1 A_1)}$$
$$k_{HS}^{U*} = k_m + \frac{A_m}{(1 - \alpha_m A_m)} \tag{2.36}$$

where

$$\alpha_1 = (3k_1)^{-1} \qquad \alpha_m = (3k_m)^{-1} \tag{2.37}$$

and

$$A_1 = \sum_{i=1}^{m} \frac{\phi_i}{\frac{1}{k_i - k_1} + \alpha_1} \qquad A_m = \sum_{i=1}^{m-1} \frac{\phi_i}{\frac{1}{k_i - k_m} + \alpha_m} \tag{2.38}$$

In the case of a two-phase material with the assumption that $k_1 < k_2$, Eq. (2.36) can be expressed simply as:

$$k_{HS}^{L*} = k_1 + \frac{\phi_2}{\frac{1}{k_2 - k_1} + \frac{\phi_1}{3k_1}} \tag{2.39}$$

and

$$k_{HS}^{U*} = k_2 + \frac{\phi_1}{\frac{1}{k_1 - k_2} + \frac{\phi_2}{3k_2}}. \tag{2.40}$$

The results of Hashin and Shtrikman, Eqs. (2.39) and (2.40) provide the strictest analytical bounds on the effective thermal conductivity of statistically isotropic two-phase composites without consideration of the microstructure.

2.5 Theoretical Bounds on Specific Heat Capacity

2.5.1 Specific Heat Capacity

Creating a temperature change in a material requires a physical amount of heat or thermal energy. The amount of heat required is dictated by the physical property of the material to absorb energy and is known as the heat capacity C. If a unit mass of material is considered, the specific heat (or specific heat capacity) c is expressed as

$$c = \frac{1}{m}\frac{\partial Q}{\partial T}, \tag{2.41}$$

where m is the mass, and Q and T are the supplied heat and temperature, respectively. The heat capacity as derived from thermodynamic relations defines the heat capacity at constant volume C_V and the heat capacity at constant pressure C_P. The two are connected through the following relationship [21]:

$$C_P - C_V = T\left(\frac{\partial P}{\partial T}\right)_{V,N}\left(\frac{\partial V}{\partial T}\right)_{P,N}, \tag{2.42}$$

where T is the temperature, P is the pressure, V is the volume, and N is the number of particles. While the partial derivatives are taken at constant volume and particles, and constant pressure and particles. This can be rewritten to take the form [21]

$$C_P - C_V = VT\frac{\alpha^2}{\beta_T}, \tag{2.43}$$

where α is the coefficient of thermal expansion and β_T is the isothermal compressibility.

2.5.2 Analytical and Semi-Analytical Approaches

While a literature review of the prediction of effective composite material properties such as the elastic moduli, thermal conductivity and coefficient of thermal expansion has resulted in numerous analytical models, the same cannot be said for the specific heat capacity. To the best of the author's knowledge, there is very little literature concerning analytical expressions for the effective specific heat of composites. Rigorous mathematical bounds were presented by Rosen and Hashin in 1970 for multiphase thermo-elastic composites. Sevostianov and Kachanov [22] discussed the relationship between the effective linear elastic and thermal properties of heterogeneous materials. However, the expressions of the effective coefficient of thermal expansion and specific heat capacity were limited to the case of a two-phase composite, which in turn is shown to result in the bounds of Rosen and Hashin.

With few analytical expressions for the effective specific heat, research has turned to numerical approaches [23-27], similar to the work undertaken in the present study to solve the transient heat transfer problem. In the following sections, known models of the effective specific heat of heterogeneous materials will be provided.

2.5.3 Kopp's Law

As with other effective properties of composites, the ROM is used as a first-order approximation. As pointed out by Ochiai [28], the ROM is generally considered a starting point for predicting the effective specific heat. The ROM for specific heat at constant pressure is typically credited to Kopp [29] for his study of the boiling points of organic compounds. Kopp's law states that the molecular heat capacity of a solid composite material is the sum of the heat capacities of each phase. Thus, Kopp's approximation of the effective specific heat $c^*_{p,K}$ of an isotropic two-phase composite is:

$$c^*_{p,K} = \frac{\phi_1 \rho_1 c_p^1 + \phi_2 \rho_2 c_p^2}{\rho^*}, \tag{2.44}$$

where ϕ_i, c_p^i and ρ_i are the volume fraction, specific heat and density of each phase, and ρ^* is the effective composite density defined as

$$\rho^* = \phi_1 \rho_1 + \phi_2 \rho_2. \tag{2.45}$$

2.5.4 Rosen and Hashin Model

As stated by Rosen and Hashin [14], for a uniform temperature increase in a composite subjected to surface boundary conditions such as displacement or traction, there is no change in the average stress or strain, but local values may vary. This statement provides evidence that the effective specific heat of the composite is not the volume fraction weighted average of each phase-specific heat as provided in Eq. (2.44). Using the principles of thermodynamic energy balance, Rosen and Hashin found that there is a temperature-dependent correction to Kopp's law on the prediction of the effective composite specific heat. The temperature-dependent Rosen-Hashin predictions for an isotropic two-phase composite is given by

$$c_{p_{R-S}}^{U*} = \langle c_p \rangle + 9T_0 \left(\frac{\alpha_2 - \alpha_1}{\frac{1}{K_1} - \frac{1}{K_2}} \right)^2 \left[\langle \frac{1}{K} \rangle - \frac{1}{K^{L*}} \right] \tag{2.46}$$

and

$$c_{p_{R-S}}^{L*} = \langle c_p \rangle + 9T_0 \left(\frac{\alpha_2 - \alpha_1}{\frac{1}{K_1} - \frac{1}{K_2}} \right)^2 \left[\langle \frac{1}{K} \rangle - \frac{1}{K^{U*}} \right], \tag{2.47}$$

where T_0 is the reference temperature in Kelvin, K_i and α_i are the bulk modulus and the coefficient of thermal expansion of the *i*-th phase, respectively, and K^{U*} and K^{L*} are the upper and lower effective bulk moduli predicted by Eq. (2.12). The specific heat at constant volume can be found through the following relation [21]:

$$c_v^* = c_p^* + \frac{1}{\rho^*} \boldsymbol{C}_{ijkl}^* \alpha_{ij}^* \alpha_{kl}^* T_0 \,. \tag{2.48}$$

Here, $\boldsymbol{C}$ is the fourth-order elastic moduli tensor, and ρ^* and α^* are the effective density and CTE. The upper and lower bounds can be found by replacing the appropriate bounds for the CTE and elasticity tensor.

2.6 Direct Numerical Methods

While the analytical methods are based on rigorous mathematical and physical considerations, their application to the modeling of the effective properties of composite materials is somewhat limited due to the very restrictive assumptions introduced in the course of their derivations. Take, for example, a case when arbitrary geometry is used. Here, the majority of the models will not be useful in accounting for such influence. Moreover, consider the case when one, some, or all of the constituent materials do not exhibit linear-elastic behavior. One can also consider materials that exhibit anisotropy or material properties that are state dependent, such as the dependence of Young's modulus

on strain rate, for example. In these cases, more and more interest has been focused on numerical methods to estimate such properties. Numerical models have the advantage of considering the effects of geometry, stress concentrations, non-linear behavior, etc. However, these advantages can be mitigated at the expense of being computationally expensive. The following sections will outline procedures for numerically estimating the effective macro- or continuum-level properties.

2.6.1 Representative Volume Element

Regardless of the numerical approach taken, the majority of methods depends on the definition of a representative geometry to perform the numerical simulation. Here, RVE is used to classify a sample of a composite or heterogeneous material that is typical of the entire material on average and contains a sufficient amount of inclusions such that the apparent properties are independent of the surface traction and displacement, as stated by Hill [30]. The RVE behaves in such a way that the response is identical to or representative of the material as a whole. The volume of this element Ω_0 is divided up amongst the constituent materials as Ω_i, where $i = 1$ to the number of phase materials. With the increase in computing power at the desktop level, numerical techniques are becoming ever more popular to solve the field equations in the RVE; for this reason, the size of the RVE domain is important when considering numerical homogenization. Hill's condition [30] has been widely accepted as a measure of determining the appropriate RVE size. In the case of elastic response, this condition states that the energy at the micro level must be equivalent to the effective energy for the homogenized material over the volume if uniform stress or strain exists on the RVE boundary.

2.6.2 Image-Based Modeling

Researchers have developed computational models and approaches capable of modeling the RVE or the entire macrostructure and incorporating details of the material

microstructure. One popular technique to obtain the material microstructure is via scanning electron microscope (SEM) images. Here, images are taken of portions of the material under consideration and then exported to create discretized finite element models (FEM). This method has been used to determine the effective elastic response [31, 32], elastic and thermoelastic properties [33, 34], thermal conductivity [35] and failure [36, 37], to name a few.

2.6.3 Artificial Modeling

Another widely used approach to define the RVE is to artificially model the microstructure with simplified geometric representations of the actual or expected microstructure. Here researchers have exploited the simplified microstructure by assuming reinforcement phases as basic shapes such as spheres, disks, cylinders, ellipsoids, etc., resulting in a less complex analysis. The distribution of the reinforcement phases of the artificial microstructure can be based on actual images of the material or merely on random or particular distribution functions with either a periodic or non-periodic array. Ideally a researcher would base the decision on as much information on the microstructure that is known or anticipated during the manufacturing process.

2.6.4 Numerical Homogenization: Background

Regardless of the method used or the definition of the RVE, the aim of numerical homogenization is to determine the effective properties of heterogeneous materials when analytical models or experimental data are not valid or feasible. Numerical homogenization is carried out by volume averaging the response of each of the constituent materials to determine the effective material response. This technique assumes that the discretized material microstructure is adequately approximated. Some of the earliest numerical approximations were carried out using 2D finite difference schemes to determine the effective elastic properties of fiber-reinforced composites by

Adams and Doner [38, 39] in the late 1960s. However, with high computational power at the desktop level, researchers have the capability to approach the problem using various methods such as finite element [40-45], method of cells [46, 47] and Fourier transform-based methods [48-51], to name a few. Moreover, the concepts are not limited to elastic properties. The idea has also been applied to predict other effective properties such as thermal conductivity [23, 52, 53], thermal expansion [25, 41, 52, 54] and specific heat [23, 25].

2.6.5 Numerical Homogenization: Elasticity

The elastic modulus of the RVE is estimated by applying a tensile load to the RVE and volume averaging the strain and stress throughout the RVE. Thus, the effective elastic moduli tensor $\boldsymbol{C}^*$ is determined as

$$\boldsymbol{C}^* = \frac{\bar{\sigma}_{ij}}{\bar{\epsilon}_{ij}} \tag{2.49}$$

where average stress, $\bar{\sigma}$, and average strain, $\bar{\epsilon}$, are computed as

$$\bar{\sigma}_{ij} = \frac{1}{V}\int_V \sigma_{ij} dV \tag{2.50}$$

and

$$\bar{\epsilon}_{ij} = \frac{1}{V}\int_V \epsilon_{ij} dV \tag{2.51}$$

and V is the volume of the RVE. The tensile load is applied via prescribed displacement and appropriate boundary conditions. In a discretized FEM, the average stress and strain, Eqs. (2.50) and (2.51), can be written as

$$\bar{\sigma}_{ij} = \sum_{k=1}^{N} \sigma_{ij}^{k} \Omega^{k}, \tag{2.52}$$

$$\bar{\epsilon}_{ij} = \sum_{k=1}^{N} \epsilon_{ij}^{k} \Omega^{k}. \tag{2.53}$$

Here σ_{ij}^{k}, ϵ_{ij}^{k} and Ω^{k} denote the stress, strain and integration volume of the *k*-th element, respectively. Equations (2.49)-(2.53) can be applied to other material properties with substitution of the proper field equations. Specific details of each will be provided in the forthcoming sections.

2.6.6 Numerical Homogenization: Thermal Conductivity

The effective RVE thermal conductivity is assessed by applying a specified temperature gradient across two faces of the RVE while insulating the remaining faces and assuming a steady-state condition. The temperature gradients and heat fluxes are then volume averaged to determine the effective thermal conductivity k^{*} as determined by

$$k^{*} \nabla \bar{T} = -\bar{q} \tag{2.54}$$

where the average temperature gradient, $\nabla \bar{T}$, and average heat flux, $\bar{q}$, are calculated in a fashion similar to Eqs. (2.50)-(2.53). The temperature gradient is enforced using appropriate boundary conditions to create a difference across two of the RVE faces while maintaining equivalent temperature change across the remaining faces of the RVE.

2.6.7 Numerical Homogenization: Thermoelasticity

The CTE of the RVE is estimated by applying a thermal load to the RVE and volume averaging the stress and strain throughout the domain. Thus, assuming a linear CTE and zero strain at reference temperature T_0, the effective CTE α^* is determined as

$$\bar{\epsilon}_{th} = \alpha^*(T - T_0) \tag{2.55}$$

where the average thermal strain, $\bar{\epsilon}_{th}$, is computed in a fashion similar to Eq. (2.51) or Eq. (2.53) with a specified temperature T imposed on the domain. In addition to the previous description, the effective thermal expansion can also be calculated using a combined elastic and thermal analysis by evaluating the contributions to thermal and mechanical stress/strain separately.

2.6.8 Numerical Homogenization: Specific Heat

The effective RVE specific heat is determined by applying a uniform heat source to the body and assuming a transient condition. The temperature gradients and heat fluxes are then volume averaged to determine the effective specific heat c_p^* given as

$$\bar{Q} = C_p^* \, \bar{\rho} \, \overline{\frac{dT}{dt}} \tag{2.56}$$

where the average heat body flux, $\bar{Q}$, and average temperature change with respect to time, $\overline{dT}/dt$, can also be determined using appropriate variables and procedures previously described. The effective density, $\bar{\rho}$ is calculated using the ROM given by Eq. (2.45). Additionally, the effective specific heat and thermal conductivity can be determined collectively in one model using a transient thermal analysis. Here, once the domain reaches a steady-state, the effective thermal conductivity can be evaluated. With this information, the effective specific heat can then be back calculated.

2.7 Boundary Conditions

With any numerical or analytical model, boundary and initial conditions must be specified. The initial conditions in most cases are fairly straight-forward: the system is typically taken at a zero state, e.g., a uniform temperature that results in zero initial strain, and zero heat transfer. The choice of boundary conditions can have a significant impact on the response of the model. Moreover, different choices in boundary conditions can lead to different results for the same model. Ideally the choice of boundary conditions will reflect the real-world conditions. However, this is not always practical or possible as many different types of boundary conditions can be present on the body or region of interest. The main goal when implementing boundary conditions is to, as closely as possible, model the behavior of the system in its natural setting while limiting the influence of nonphysical behavior on the system. In the case of an RVE, the goal is to model the representative volume in such a way that the response would mimic the response of the material as a whole. To achieve this goal, one of three types of boundary conditions is typically chosen: (1) Kinematic Uniform Boundary Conditions (KUBCs), (2) Static Uniform Boundary Conditions (SUBCs), and (3) Periodic Boundary Conditions (PBCs). In some cases, combinations of two or more of the boundary conditions, known as “mixed boundary conditions,” [55, 56] may be chosen when appropriate. Other types of RVE boundary conditions are also possible. The only general requirement in the formulation is that they should be consistent with the homogenization theorem(s) applied.

2.7.1 Homogenous Boundary Conditions

Of the three types of boundary conditions, KUBCs (Dirichlet) and SUBCs (Neumann) are lumped into what is referred to as homogenous boundary conditions (HBCs). According to Hill [30], an RVE is said to be well defined when the effective response using HBCs (KUBCs/SUBCs) coincides. In numerical models, HBCs offer the advantage of reduced computation time due to the reduced number of constraint

equations. This makes this class of boundary conditions useful for material models with a large number of finite elements and/or degrees of freedom (DOF). However, because HBCs simulate the entire macro structure with its phase materials (as opposed to PBCs, which simulate the entire macro structure with micro level periodically repeating cells), the convergence of effective properties becomes a function of the domain (RVE) size. Determination of the minimum size of the RVE has been studied in the works of such authors as Huet [57], Amieur et al. [58] and Huet [59]. The size of the RVE has been found to be a function of the behavior of the constituent materials, inclusion size, geometry effects, etc. The following sections will provide details of the development and construction of elastic, thermoelastic and thermal HBCs used in this work.

2.7.1.1 Elastic Homogenous Boundary Conditions

According to Aboudi [46] HBCs can be either kinematic or static. Kinematic uniform boundary conditions are defined as an imposed displacement $\boldsymbol{u}_i$ at each point $\boldsymbol{x}_i$ on the boundary Γ such that

$$u_i(\Gamma) = \boldsymbol{\epsilon}^0 x_i. \tag{2.57}$$

Here $\boldsymbol{\epsilon}^0$ is a constant global strain tensor. Static uniform boundary conditions are defined as an imposed traction $\boldsymbol{t}_i$ at each point $\boldsymbol{x}_i$ on the boundary Γ such that

$$\boldsymbol{t}_i(\Gamma) = \boldsymbol{\sigma}^0 \boldsymbol{n_i}, \tag{2.58}$$

where $\boldsymbol{\sigma}^0$ is a constant stress tensor and $\boldsymbol{n}_i$ is the outward normal on Γ. In this work, the kinematic formulation has been adopted for models when homogenous boundary conditions are used.

Homogenous boundary conditions are implemented into FEMs by creating reference nodes and linking the DOF of each face to a reference node, similar to that of an earlier study by Kassem [60]. A total of six reference nodes are created with each constrained to nodal sets on each of the six cube faces. Each reference node is constrained to the corresponding cube face using the Abaqus command **TIE* [61]. This formulation allows for the model to be subjected to either a tensile or compressive perturbation (uni-axial or multi-axial) or shear loading. A schematic of the reference nodes on an RVE is shown below in Fig. 2.1 with the reference point locations provided in Table 2-1 assuming a unit RVE.

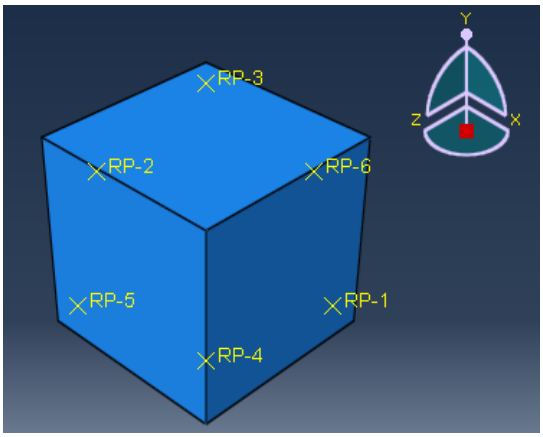

Figure 2.1. FEM HBC reference point definition.

Table 2-1. HBC reference point locations.

Face	Coords. (x, y, z)	Ref. Point
Left	(0, y, z)	RP-1
Right	(1, y, z)	RP-2
Bottom	(x, 0, z)	RP-3
Top	(x, 1, z)	RP-4
Rear	(x, y, 0)	RP-5
Front	(x, y, 1)	RP-6

Tensile loads with HBCs are implemented by fixing reference points normal to the applied load and applying tensile perturbation to one or all of the remaining reference

points or surface traction to remaining faces. For example, consider a tensile perturbation in the x^+ direction that leads to the conditions in Table 2-2.

Table 2-2. Example of tensile perturbation boundary conditions.

Face	Ref. Point	u_x	u_y	u_z
Left	RP-1	*0*	*free*	*0*
Right	RP-2	$u^0{}_x$	*free*	*free*
Bottom	RP-3	*free*	*0*	*free*
Top	RP-4	*free*	$u^0{}_y$	*free*
Rear	RP-5	*free*	*free*	*0*
Front	RP-6	*free*	*free*	$u^0{}_z$

Here u_i^0 is the applied displacement for the *x*, *y* and *z* directions. These boundary conditions are easily modified to accommodate loading in various directions and shear loading.

2.7.1.2 Thermal Homogenous Boundary Conditions

The concepts of the mechanical HBCs are extended to the thermal analysis with thermal uniform temperature gradient (UTG) defined as an imposed temperature $\boldsymbol{T}_i$ at each point $\boldsymbol{x}_i$ on the boundary Γ such that

$$T_i(\Gamma) = \nabla \mathbf{T}^0 x_i, \tag{2.59}$$

where $\nabla \boldsymbol{T}^0$ is an applied temperature gradient. Similarly, as in the mechanical case, the thermal uniform heat flux (UHF) as expressed as

$$q_i(\Gamma) = \boldsymbol{Q}^0 \boldsymbol{n}_i. \tag{2.60}$$

Here q_i is the microscopic heat flux, $\boldsymbol{Q}^0$ is a constant heat flux vector and $\boldsymbol{n}_i$ is the outward normal vector on Γ. For the extent of the work presented, HBCs are not used for thermal models unless noted otherwise. The benefits of these boundary conditions are not realized for the size of numerical models analyzed.

2.7.1.3 Thermoelastic Homogenous Boundary Conditions

Homogenous thermoelastic boundary conditions are applied in the same manner as the elastic HBCs in Section 2.7.1.1, but the global strain vector, $\boldsymbol{\epsilon}^0$, is specified as zero, and a uniform temperature is imposed on the RVE domain, resulting in thermal strains throughout the body. In situations where a non-uniform thermal load is desired, the thermal HBCs of Section 2.7.1.2 can also be incorporated into the thermomechanical analysis.

2.7.1.4 Specific Heat Homogenous Boundary Conditions

In this work, HBCs for determining the effective specific heat of a material are the same as the thermal HBCs of Section 2.7.1.2.

2.7.2 Periodic Boundary Conditions

While PBCs can be computationally more expensive per iteration than HBCs, they do offer some advantages, such as size independence and ability to evaluate the macro-level effective properties. The dependence off cell size on the convergence of effective properties can be seen graphically in Fig. 2.2. The following section will provide details on the development and implementation of PBCs into FEM.

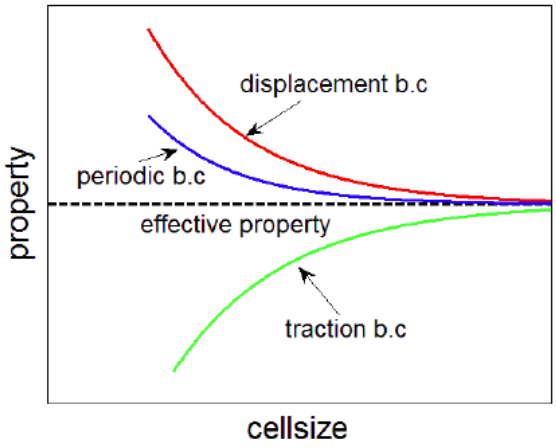

Figure 2.2. Convergence of effective material properties [62].

2.7.2.1 Elastic Periodic Boundary Conditions

As noted by Kassem [60], consider a structure assumed to be periodic consisting of a periodic array of repeating cells subjected to macro-level strain tensor $\boldsymbol{\epsilon}^0$. The displacement for the structure u_i is expressed as

$$u_i = \boldsymbol{\epsilon}^0 x_i + u_i^*. \tag{2.61}$$

Here u_i and x_i are the displacement and position vector of the *i*-th node. The last term on the right side, u_i^*, represents a periodic function that is a modification of the linear displacement field due to the material heterogeneity. Moreover, the displacement of the structure can be thought of as the contributions from the slowly varying macroscopic fields and variations in the microscopic response. Because the structure represents a continuous body of material, there are two conditions that must be satisfied by the RVE. First, the displacements must be continuous along the boundary of the RVE. In a physical sense, this condition requires that, when assembled after deformation, gaps or penetration between neighboring RVEs do not exist. This requirement is used to eliminate the

periodic displacement function u_i^*, which is typically not known. The elimination can be derived by considering the displacement of two opposite faces

$$u_i^{k^+} = \boldsymbol{\epsilon}^0 x_i^{k^+} + u_i^*, \tag{2.62}$$

$$u_i^{k^-} = \boldsymbol{\epsilon}^0 x_i^{k^-} + u_i^*. \tag{2.63}$$

Here the k^+ and k^- superscripts denote parallel and opposite faces (node pairs in context of finite element analysis (FEA)) with subscript *i* vector components. Because the periodic displacement function is common between the two faces, the difference of Eqs. (2.62) and (2.63) results in the following:

$$u_i^{k^+} - u_i^{k^-} = \boldsymbol{\epsilon}^0 \left(x_i^{k^+} - x_i^{k^-} \right) = \boldsymbol{\epsilon}^0 \Delta x_i^k \tag{2.64}$$

Additionally, because $x_i^{k^+}$ and $x_i^{k^-}$ are constants for each pair of nodes and the global strain vector $\boldsymbol{\epsilon}^0$ is defined, the right-hand side becomes a constant. Thus, implementation of elastic PBCs into FEMs is simplified by constructing a series of constraint equations for each node pair and their respective components. This is realized using the commercial FEA code Abaqus, with the input file flag **EQUATION* and correct specification of the respective node pairs. The global strain vector is applied to a so-called dummy or reference node located outside of the geometric domain. A 2D representation of this effect subjected to the tensile perturbation is presented graphically in Fig. 2.3.

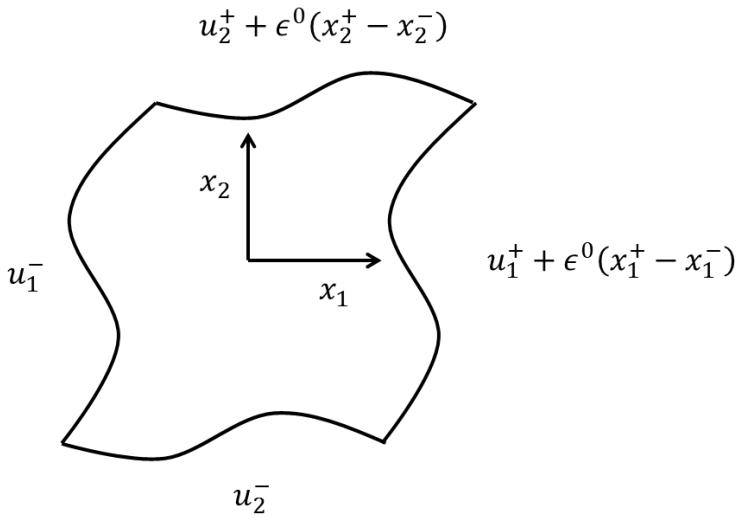

Figure 2.3. 2D periodic boundary condition example.

The second condition requires that the surface tractions on the RVE surface be symmetric between opposite faces, that is,

$$t(x_i^+) - t(x_i^-) = 0. \tag{2.65}$$

This condition implies that, when the cells are assembled, the traction distribution along the boundaries will also be continuous.

2.7.2.2 Thermal Periodic Boundary Conditions

As mentioned above, for the extent of this work, PBCs are used when evaluating thermal models. Considering the same array of repeating cells' periodic structures mentioned previously, the temperature of the structure T_i subjected to a macro-level temperature gradient $\nabla \boldsymbol{T}^0$ is expressed as

$$T_i = \nabla \boldsymbol{T}^0 x_i + T_i^*. \tag{2.66}$$

Here, T_i and x_i are the nodal temperature and position vector of the *i*-th node, while T_i^* is a periodic function representing a modification to the temperature field. Following the same procedure as in Section 2.7.2.1, the periodic function T_i^* can be eliminated, resulting in the following condition between parallel opposing faces:

$$T_i^{k^+} - T_i^{k^-} = \nabla \boldsymbol{T}^0 \left(x_i^{k^+} - x_i^{k^-} \right) = \nabla \boldsymbol{T}^0 \Delta x_i^k \tag{2.67}$$

Once again, due to $x_i^{k^+}$ and $x_i^{k^-}$ being constant for each pair of nodes and a specified global temperature gradient vector $\nabla \boldsymbol{T}^0$ applied, the right-hand side becomes a constant. Additionally, when the collection of RVEs is assembled heat flux compatibility must also be satisfied:

$$q(x_i^+) + q(x_i^-) = 0. \tag{2.68}$$

This condition implies that, when the cells are assembled, the heat flux along the boundaries will also be continuous and conserved. Thermal PBCs are implemented into the chosen FEA code using the same procedure used in the case of elastic PBCs.

2.7.2.3 Thermoelastic Periodic Boundary Conditions

Thermoelastic PBCs are formulated in a similar manner as the elastic boundary conditions in Section 2.7.2.1 except the global strain vector, $\boldsymbol{\epsilon}^0$, is taken as zero. This modification, along with a prescribed uniform temperature, forces an equivalent response for each face or pairs of nodes of the RVE, resulting in thermal strain within the body. In the case when a non-uniform temperature is prescribed, the thermal PBCs of Section 2.7.2.2 can also be incorporated into the thermoelastic analysis to evaluate the effective thermomechanical response when subjected to spatially dependent thermal loads.

2.7.2.4 Specific Heat Periodic Boundary Conditions

In this work, PBCs for determining the effective specific heat of a material are the same as those used for thermal PBCs in Section 2.7.2.2.

CHAPTER 3

MODELING OF GRADED MICROSTRUCTURES

3.1 Functionally Graded Materials

Functionally graded materials are heterogeneous composite materials consisting of two or more distinct phases characterized by continuously varying material properties along at least one spatial direction (typically the thickness). They were first conceptualized by a group of Japanese material scientists in the early 1980s while attempting to find thermal protection materials capable of withstanding a 2000 K surface temperature with a 1000 K gradient through a 10 mm thick section [63]. To accomplish this, they employed the notion of gradually transitioning from one material to another. This gradual variation or spatial variation (i.e., grading) is accomplished by continuously varying the volume content of each of the constituents in space. Grading provides design engineers the opportunity to create structures that possess material properties and multi-functionality not found in classical materials and conventional engineering composites.

The most appealing aspect of FGMs is the ability to tailor material properties to specific demands. Because of this attribute, FGMs have been gaining substantial traction in the automotive and aerospace industries due to their unique ability to tailor thermomechanical properties and performance, particularly for high-temperature environments. Such practical applications are disc brake rotors for automobiles, where a material with high toughness, light weight, excellent thermal properties and hardness is desired. In the aerospace industry, FGMs show promise as TPSs, TBCs, engine components and structural members [64], where tailoring of mechanical and thermal properties can yield enhancement of the thermomechanical structural response.

3.2 Functionally Graded Material Modeling

One of the most appealing and predominant characteristics of FGMs is the ability to tailor material properties or behavior with the end goal of optimizing and/or producing a desired system response. Thus, the anticipated loading and operating environment seen by the structure will strongly influence the types of materials used and the manner in which they are varied. For the extent to this work, FGMs are mathematically modeled as continuously variable composition composites. For a 1D graded two-phase material, the reinforcement through-thickness distribution, v_2, can be described by the power law as

$$v_2(z) = \eta_z \left(\frac{z}{h}\right)^{n_z}, \tag{3.1}$$

where z and h are the thickness coordinate and total thickness, and η_z and n_z are parameters controlling the maximum phase-one material (e.g., ceramic in the metal-ceramic composite) content and the grading profile in the thickness direction, respectively. In the case of 2D graded materials, the through-thickness and in-plane distribution can be defined by the following:

$$v_2(x, z) = \eta_{max} \left\| \eta_x \left(\frac{x}{l}\right)^{n_x} + \eta_z \left(\frac{z}{h}\right)^{n_z} \right\|. \tag{3.2}$$

Here, x and L are the longitudinal axis coordinate and total panel length, and η_x and n_x are parameters controlling the phase-one material (e.g. ceramic in the metal-ceramic composite) content and the grading profile in the longitudinal direction, respectively. While, η_{max} is a parameter controlling the maximum overall inclusion volume fraction. Additionally, for all composite material systems, the following condition must also be met:

$$\sum_{i=1}^{N} v_i = 1. \tag{3.3}$$

3.3 Artificial Representative Volume Elment Generation

This section presents the techniques and algorithms developed and/or adopted in this study to model RVEs for fixed volume fraction and graded composite microstructures. These two-phase material models consist of simplified geometry (disks and spheres) representing both 2D and 3D models.

The RVE of two-phase fixed volume fraction composites used throughout this work is taken as a cube or square of unit length $L = 1$ with monodispersed and polydispersed spherical or disk particles to model the inclusion material. Furthermore, both partial and whole inclusions are used with periodic and non-periodic boundary conditions with a thorough comparison of both presented in this work. Cubic geometry is often chosen when investigating the effective mechanical properties of composites due to the ease of model creation [44, 45, 51]. The goal of this work is to develop and implement algorithms capable of generating artificial material microstructures with the highest possible inclusion volume fraction at the lowest computational cost. In this case, minimizing the amount of time to generate microstructures is crucial as a large number of models can be examined depending on the type of analysis. Furthermore, the generated RVEs must satisfy displacement and traction continuity requirements and be statistically isotropic, all of which are explained and investigated in the following sections. To generate the artificial microstructures needed for numerical models, two types of methods are used. For inclusion volume fractions below the jamming limit, which is calculated by Torquato [65] as 0.55 and 0.38 for randomly close packed disks and spheres using PBCs (closer to 0.48 and 0.30 for hard wall boundary conditions), a Random Sequential Adsorption (RSA) [66] algorithm is adopted. Here, particles are given random

coordinates and accepted if a minimum distance exists between all other particles previously accepted. The algorithm is completed when the number of particles in the system is equivalent to that desired. Moreover, because the random packings are to be eventually implemented into an FEM, a clearance distance is also specified to ensure that poor elements are not formed between particles. For volume fractions up to 91% and 61% for disks and spheres, respectively, an event driven molecular dynamics (EDMD) algorithm is used. The EDMD routine is inspired by the algorithm proposed by Lubachevsky and Stillinger [67] and implemented for use in micromechanics by Ghossein [68]. The algorithm in this work is modified by exploiting the RSA algorithm to generate an initial packing fraction and distribution with an initial particle radius. Each particle is then given an initial velocity whose components are independently distributed at random between -1 and +1. The algorithm begins by computing the minimum time for either a binary collision between particles or, in the case of hard wall boundary conditions (non-periodic), a binary collision and particle collision with a cell face. Next, the radii of the spheres/disks are increased according to a user-defined growth rate, uniform for monodispersed and non-uniform for polydispersed systems. Lastly, the particle velocities are updated assuming purely elastic collisions with increasing energy due to the increasing radius. In the case of periodic boundary conditions mirrored images are created on opposing faces when a particle crosses a cell face. For hard wall boundary conditions, the particle's velocity is conserved with the perpendicular impact direction being reversed. The EDMD algorithm with hard wall boundary conditions has produced whole monosized sphere arrangements up to 63.3%, approaching the well-accepted value of 64% for random close packing [69]. Meanwhile, the algorithm with periodic boundary conditions (monosized periodic trimmed inclusions) has approached the theoretical maximum packing volume fraction of 74.05% [70] for spherical particles. However, it is worth noting that, at volume fractions above 60%, the packing arrangement tends to deviate from a random arrangement and take on regular arrangements such as cubic, face-

centered cubic and hexagonal close pack. To decrease the amount of computation time, the EDMD program is coded in parallel by discretizing the domain into grids according to the suggestion of Donev [71]. Here each processor is given a grid to compute binary collisions and wall impacts of the particles in its respective grid. A single processor then computes the collision times between particles close to grid boundaries. Parallelization of the code greatly reduces the amount of computational time needed to analyze higher packing fractions. All of the aforementioned algorithms were implemented by the author in the FORTRAN programming language. Once the packing configuration is completed, a Python script is used to interact with Abaqus [61], the commercial FEA code chosen for this work. Here, generation of the geometry and definition of material properties, boundary conditions, etc., are fully automated within the Abaqus Python scripting interface to streamline the modeling process.

CHAPTER 4

EFFECTIVE MATERIAL PROPERTIES OF GRADED COMPOSITES

Regardless of the intended application, the determination of the effective material response of FGMs is vital to their integration into mainstream usage. Thus, the purpose of this chapter is determine the effective properties of graded heterogeneous composites. This is achieved by first testing the hypothesis of using classical homogenization techniques developed for traditional composite materials on variable composition composites. This hypothesis is analyzed by comparing the effective properties of graded microstructures evaluated by analytical approximations and bounds to that obtained by numerical by FEA of RVEs.

4.1 Definition of RVE

An RVE for a composite system with a fixed volume fraction (macroscopically homogeneous) is typically well defined, while RVEs for variable-phase volume fraction composites (i.e., FGMs) are not as distinct or understood.

Nevertheless, a plethora of micromechanical models developed to describe the behavior of macroscopically homogeneous composites has been used to characterize the thermoelastic and thermal response of graded materials and structures. For instance, the straightforward ROM models [3, 4] have been used to describe the thermoelastic response of FGM-based thermal barriers and coatings by Lee and Erdogan [72] as well as Shaw [73] and Williamson et al. [74], to name a few. Higher-order micromechanical models such as the Mori-Tanaka and self-consistent scheme have been used to estimate the effective elastic response of graded materials [64, 75, 76]. Furthermore, various models to predict the effective CTE [11, 13, 14, 77], thermal conductivity [17, 19, 20, 78] and specific heat [14, 29] have been used in numerous works. Assessments encompassing various homogenization methods and applications applied to FGMs can be found in the reviews by Jha et al. [79], Birman and Byrd [80] and Markworth [81].

The motivation for the following sections is to determine a suitable choice of RVE for the determination of effective material properties of two-phase metal-ceramic FGMs. Particular attention will be paid to materials suitable for hypersonic structural applications, such as Titanium-based composites, due to their ability to retain high stiffness and strength at elevated temperatures.

4.2 Piecewise Layered RVE

In a fashion similar to that described in the literature [82], RVEs are generated by considering regions that have a uniform-to-slow variation in material composition (i.e., constant volume fraction), as shown in Fig. 4.1. This approach leads to statistically homogenous piece-wise RVEs of the graded microstructure that neglect interactions/influence from neighboring cells, creating a so-called Local Representative Volume Element (LRVE). Although this approach neglects neighboring interactions, it does have the added convenience that the effective material properties of the composite are assumed to be independent from the grading of the material. Thus, the effective material properties need only be evaluated once for each volume fraction.

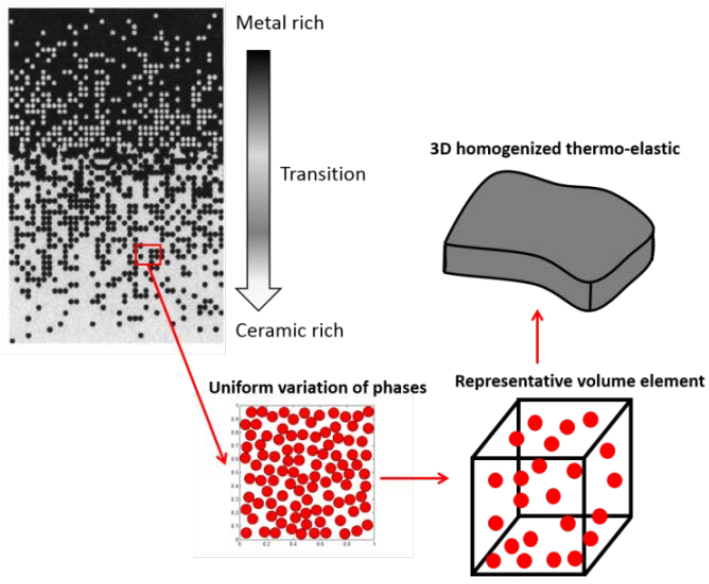

Figure 4.1. Layered RVE model.

4.2.1 Piecewise Layered RVE: Model Generation

The layered FGM model is constructed by first defining the material variation using the desired grading parameters along with either Eq. (3.1) or (3.2) and defining a specific number of volume fractions to model. Next, a volume fraction threshold is defined, which here is referred to as a transition zone, to switch the material phases (matrix becomes reinforcement and vice versa) when the reinforcement volume fraction exceeds this value. Swapping of the constituent phase materials is done to accommodate volume fractions that exceed the maximum permissible packing fraction. Finally, RVEs (either periodic or non-periodic) are created and the effective or overall composite properties determined using numerical homogenization techniques mentioned in Section 2.6. To account for variations in geometry, the effective material properties are averaged over no less than five random models. As mentioned previously, this procedure leads to homogenous piecewise RVEs that neglect the influence of neighboring cells and the profile in the material variation. A simplified graphical representation of the layered model approach is provided below in Fig. 4.2.

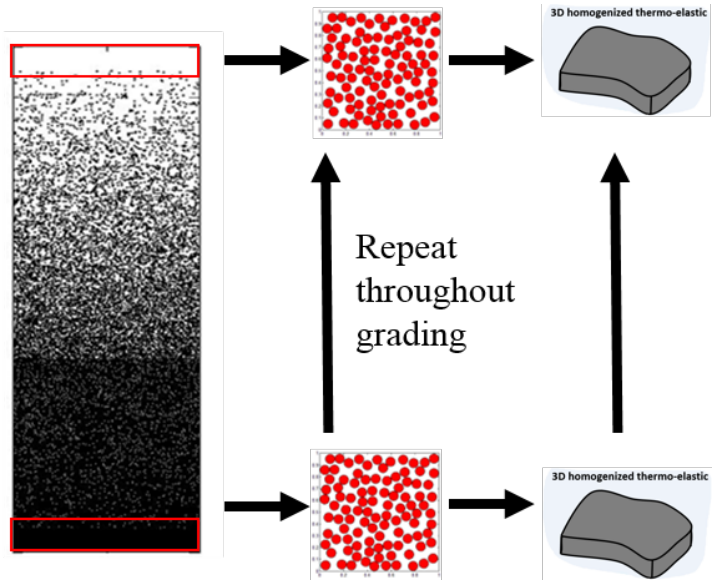

Figure 4.2. Graphical representation of the layered approach.

4.3 Continuous FGM RVE

In the context of FGMs, when applying the above methods (analytical and numerical), it is assumed that in regions where variation in phase volume fraction is constant or slowly varying an RVE exists. Thus, this RVE represents a material averaged response limited only to the region of interest. This approach is undoubtedly popular due to the fact that the response of the graded material can be obtained from layers of homogenous models, with material properties estimated in terms of local volume fractions while neglecting interactions of neighboring layers and material gradients. However, such methods raise concerns when the interactions between multiple layers cannot be neglected, particularly when there is a steep variation in material composition along the grading direction, as suggested by Anthoine [83]. Here, modeling of the complete variation in microstructure may influence the surrounding layers due to the particle interactions at the micro level taking place due to the varying material composition. Moreover, such an approach becomes even more troublesome when evaluating regions in the material when differentiation between the matrix and reinforcement phases is not well defined. To evaluate the effect these claims, artificial FGM microstructures are created and evaluated using FEA.

A similar modeling approach was taken by Reiter and Dvorak [84]. In their work, a carbon/silicone-carbide (C/SiC) linearly graded microstructure using a hexagonal-shaped reinforcement phase was homogenized using FEA with the resulting elastic response compared to the analytical Mori-Tanaka bounds [85] and self-consistent approximation [7, 8] to determine the legitimacy of using traditional micromechanical models on graded microstructures. Their models were later extended to evaluate the thermal and thermomechanical response and to assess the rationale of using classical analytical approximations to determine the effective response of the graded structure [86]. The findings of this work for the elastic, thermoelastic and thermal response indicate that the micromechanical models, originally developed for statistically

homogenous composites, may be applied to graded composites subjected to uniform and non-uniform loads with a reasonable degree of confidence. Furthermore, these conclusions also imply that the linearly graded C/SiC microstructure has little influence on the homogenization of the effective material response. Additionally, Grujicic and Zhang [87] performed similar work using the Voronoi cell method implemented into commercial FEA code on Ni/MgO and Ni_3Al/TiC systems with non-linear material variation. The resulting material properties were found to be in good agreement with experimental values and compared reasonably well with the self-consistent approximation [7, 8], further reinforcing the notion of using classical micromechanical models for graded composites.

The contribution of this work is the creation of high-resolution models utilizing simplified geometries to evaluate the influence of the graded microstructure on the effective homogenized material properties. This is accomplished by investigating varying degrees of material variation, such as fast, slow and uniform changes. Furthermore, in addition to the elastic and thermo-elastic properties, the effective properties will also include effective thermal conductivity and specific heat.

4.3.1 Continuous FGM RVE: Model Generation

The continuous FGM model is created in a fashion similar to the layered model outlined in Section 4.2.1. However, the influence of material variation and response and interaction of neighboring cells is taken into account by modeling the complete material variation. This is accomplished by defining a material distribution function and discretizing the geometry along the grading direction/s section into *i* layers in the case of 1D grading or *i* and *j* sections (vertical and transverse sections) for 2D grading. This same principle can also be extended to the case of 3D material grading. Each of these layers and sections is packed to the volume fraction according to Eq. (3.1) or (3.2). For cases when a continuous material variation is desired, a random distribution is given along the

boundaries of each section to attempt to mimic the theoretical continuous distribution function. Using sophisticated in-house-developed packing algorithms described in Section 3.3, complex microstructures with high-packing fractions can be produced to permit the study of transition zone locations and high-percolation composites. After model generation, FEA with appropriate boundary conditions is employed to homogenize the field response of interest for each section and layer. A low-resolution example of the entire process for a 1D graded plate is illustrated in Fig. 4.3. Comparable to the layered model case, effective material properties are averaged over no less than five random models.

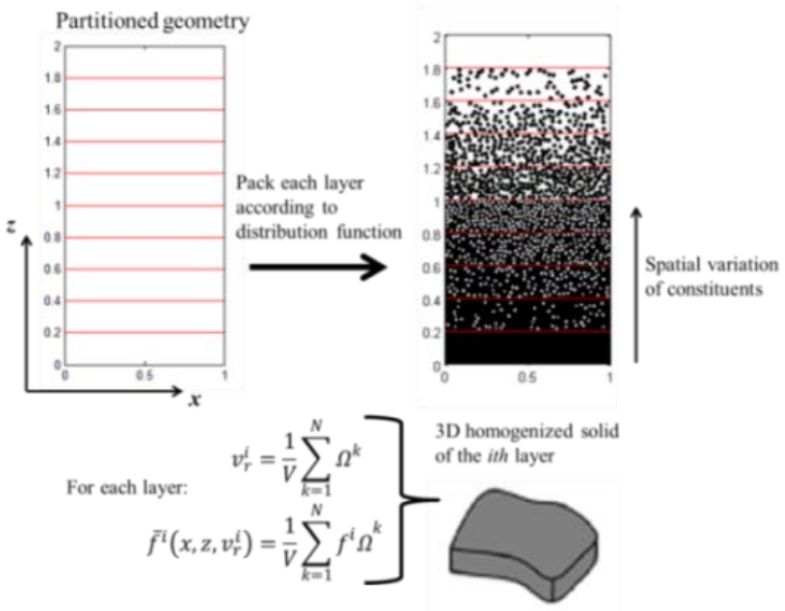

Figure 4.3. Graphical representation of the layered approach.

4.4 Effective Properties: Layered vs. Continuous Models

4.4.1 One-Dimensional Material Variation, 2D Geometry

This section provides a detailed comparison of the apparent properties of FGMs derived using homogenization techniques originally developed for traditional fixed-

volume fraction composites to the numerical values obtained by the Layered FGM RVE and Continuous FGM RVE modeling approaches described above. The results of this study will be used as guidance for determining suitable and efficient methods for acquiring the effective properties of graded composites and structures.

The influence of material variation and interaction with neighboring cell response is evaluated for a titanium and titanium Diboride (Ti/TiB_2) graded metal-ceramic system (through thickness only). This Ti/TiB_2 system can be assumed to be a composite with particulate reinforcement based on SEM images of a fabricated graded material system courtesy of Ma et al. [88]. These samples were constructed using powder metallurgy of Ti and TiB_2 powders as shown in Fig. 4.4.

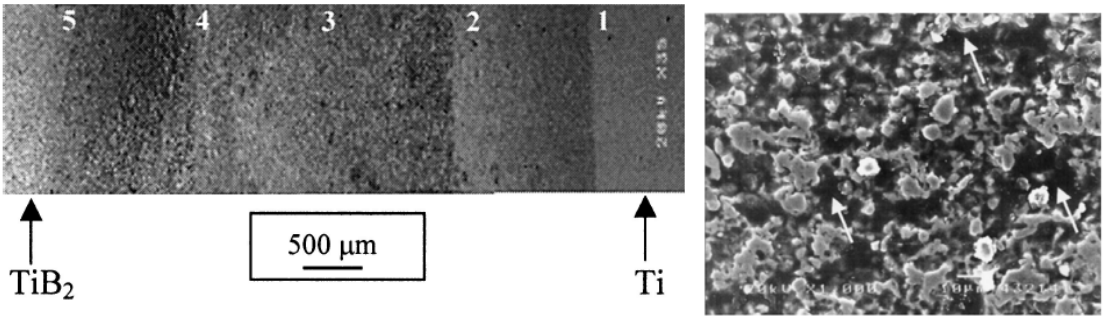

Figure 4.4. (a) Five-layer metal-ceramic Ti-TiB2 FGM (b) Ti-TiB2 microstructure: SEM image between layers 4 and 5 [88].

In the scope of this work, the reinforcement phase is modeled as simplified geometry (e.g., disks and spheres for 2D and 3D analysis). Utilizing Eq. (3.1), three material variations have been studied to determine the influence of the microstructure grading on the effective material properties. Setting the maximum ceramic volume fraction content to 1 ($\gamma = 1$), linear ($n = 1$), quadratic ($n = 2$) and square root ($n = 0.5$) functions, representing a gradual, slow and rapid variation in ceramic volume fraction, respectively, have been considered as shown in Fig. 4.5. The artificial microstructure is generated by discretizing a 5 mm section into 21 distinct layers, resulting in a volume

fraction resolution of 0.05/layer. Each layer is then packed to the desired volume fraction using the previously mentioned packing methods (RSA and EDMD) using disks with a radius of 0.005 mm (5 μm), providing an RVE characteristic length to inclusion radius of 1000. Upon the completion of all segments, a final distribution is given to the FGM along the boundaries of each division to produce as close to a continuous material variation as possible. For both the Layered and Continuous RVE models, constituent material phases are swapped when the reinforcement-phase volume content exceeds 60% (transition zone). A sample of the artificially generated geometries used for the numerical computations is provided in Fig. 4.6. For quick reference, the constituent material properties at 20 and 500 °C are provided in Table 4-1, while the complete temperature-dependent variations are provided in Figs. 4.7-4.9.

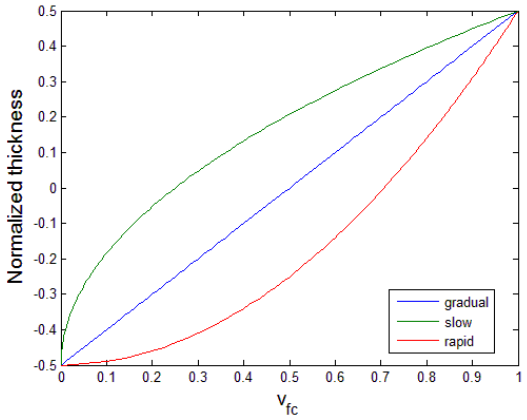

Figure 4.5. Ceramic volume fraction distribution.

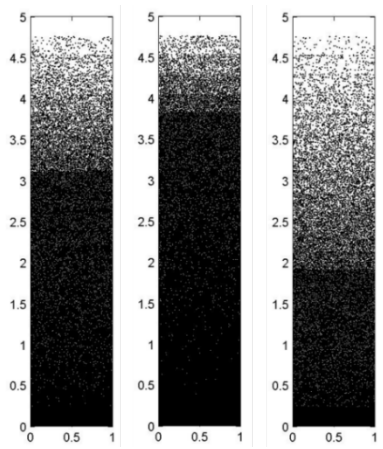

(a) (b) (c)

Figure 4.6. Artificially generated continuous FGM RVE microstructures, (a) *n=1*, (b) *n=2*, and (c) *n=0.5*.

Table 4-1. Material properties of Ti-6Al-4V [89] and TiB_2 [90, 91] at 20/500 C.

	E (GPa)	ν	α (μm/μm-K)	k (W/m-K)	C_p (J/kg-K)
Ti-6Al-4V	106.2/79.0	0.298/0.314	8.8/10.1	6.1/14.3	535.3/651.5
TiB_2	495.4/477.2	0.100/0.102	7.4/8.0	95.8/81.4	622.7/1051.8

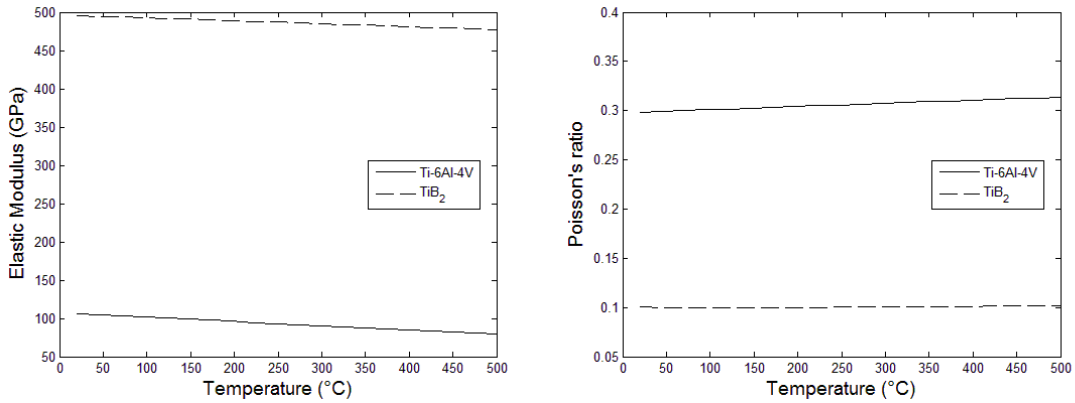

Figure 4.7. Temperature-dependent elastic modulus and Poisson's ratio of Ti-6Al-4V [89] and TiB_2 [90, 91].

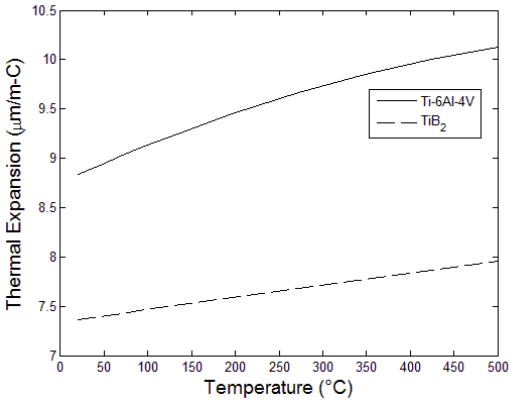

Figure 4.8. Temperature-dependent coefficient of thermal expansion Ti-6Al-4V [89] and TiB_2 [90, 91].

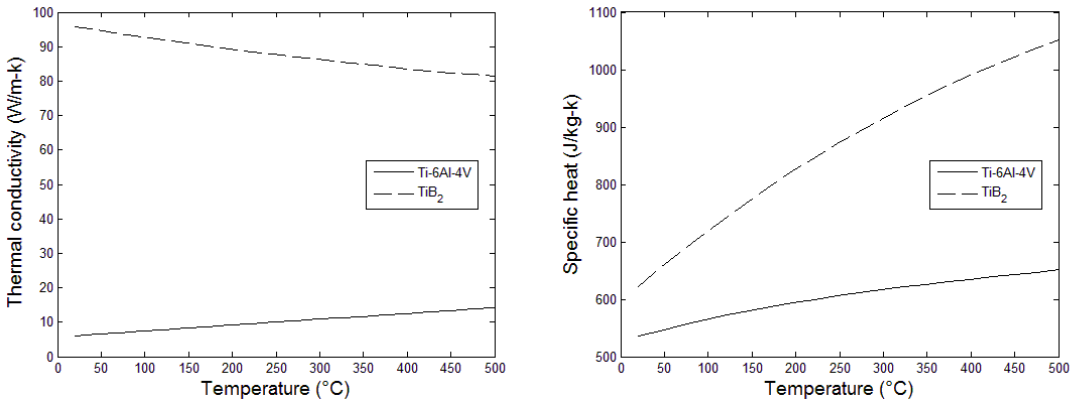

Figure 4.9. Temperature-dependent thermal conductivity and specific heat of Ti-6Al-4V [89] and TiB_2 [90, 91].

Randomly generated geometry is then imported into the commercial FEA code Abaqus [61], leveraging the Abaqus/Python scripting interface. The model-generation process has been automated to reduce user interaction. For the LRVE approach, PBCs are implemented on all sides of the LRVE. In the Continuous FGM RVE approach, mixed boundary conditions are used. Here, periodicity is enforced on the sides of the RVE transverse to the grading direction, while KUBCs are prescribed in the through-thickness direction (graded direction). For both cases, appropriate loads are applied to the RVE depending on the type of homogenized property of interest. In 2D elastic and thermo-

elastic models, triangular and quadrilateral quadratic generalized plane strain elements are used, while quadratic 3D stress elements are used in 3D cases. For steady-state and transient heat transfer, triangular and quadrilateral quadratic heat transfer elements are employed. A mesh refinement study was performed in the elastic analysis to determine an adequate mesh to properly discretize the geometry and obtain a converged solution. It is worth noting that in the case of the continuous modeling approach, a comprehensive mesh refinement study is difficult to achieve due to the large number of inclusions and tight packing fractions. For the most part, a large number of elements is needed, regardless, to generate a mesh with as few as possible distorted elements. The final element count for each simulation (approximately 800k for 2D continuous graded RVEs, 200k for 2D LRVEs and 550k for 3D LRVEs) was assumed to be the same for the elastic, thermo-elastic and thermal analysis.

4.4.1.1 Elastic Response

The elastic modulus of the artificial model is estimated by applying a tensile load to the RVE and volume averaging the elastic response (stress and strain) throughout the RVE. Thus, the effective elastic moduli tensor $\boldsymbol{C}^*$ is determined as

$$\bar{\sigma} = \boldsymbol{C}^* \bar{\epsilon} \tag{4.1}$$

where average stress, $\bar{\sigma}$, and average strain, $\bar{\epsilon}$, are computed using Eqs. (2.50) and (2.51) and V is the volume of the RVE. The tensile load is applied via prescribed displacement on a reference node and appropriate boundary conditions. In the case of LRVE models, this volume averaging is repeated for each volume fraction of interest. Meanwhile, in the case of the Continuous RVE, homogenization is repeated at each segment within the domain. The numerical homogenization results of both RVE approaches are compared to the well-known analytical and semi-analytical approximations and bounds of Voigt [3],

Reuss [4], SCM [7], and Hashin-Shtrikman [6] (Eq. (2.2), (2.3), (2.16), (2.17), (2.12), and (2.13), respectively). Here, the H-S bounds are denoted as H-S$^+$ and H-S$^-$ for the upper and lower bounds, respectively. The results and comparisons at 20 and 500 °C are provided in Fig. 4.10. Figures 4.11-4.12 provide detailed results of each modeling technique (Layered and Continuous) compared to the rigorous bounds of Hashin and Shtrikman. It should also be noted for clarification that in this work the terms *elastic modulus* and *Young's modulus* are used interchangeably.

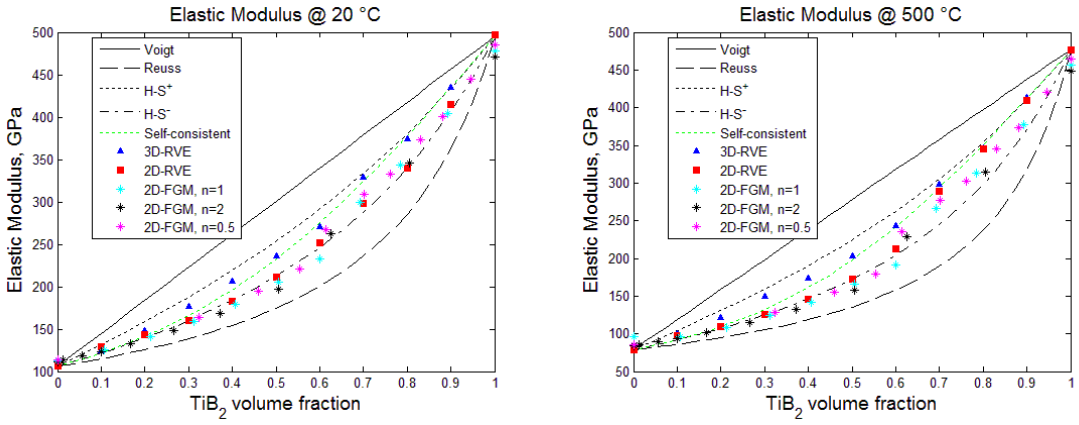

(a) (b)

Figure 4.10. Effective elastic modulus (a) 20 °C and (b) 500 °C, all models.

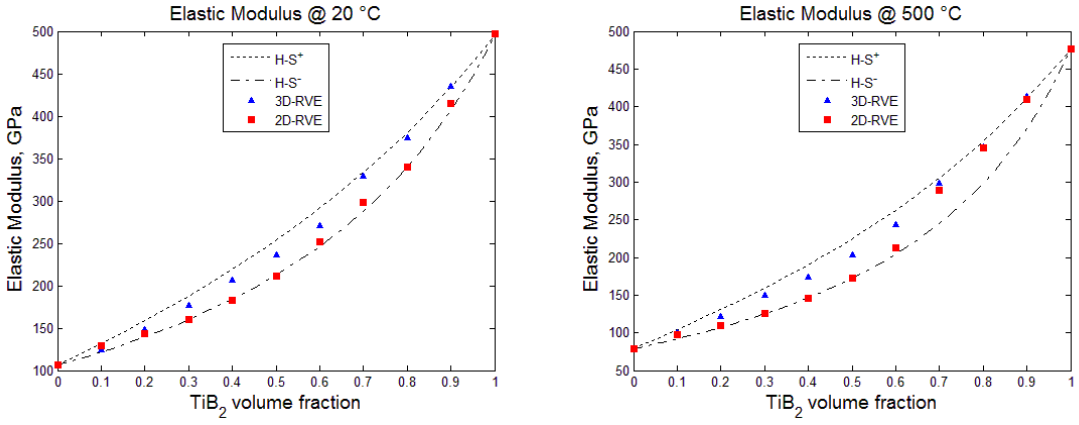

(a) (b)

Figure 4.11. Effective elastic modulus (a) 20 °C and (b) 500 °C, layered models.

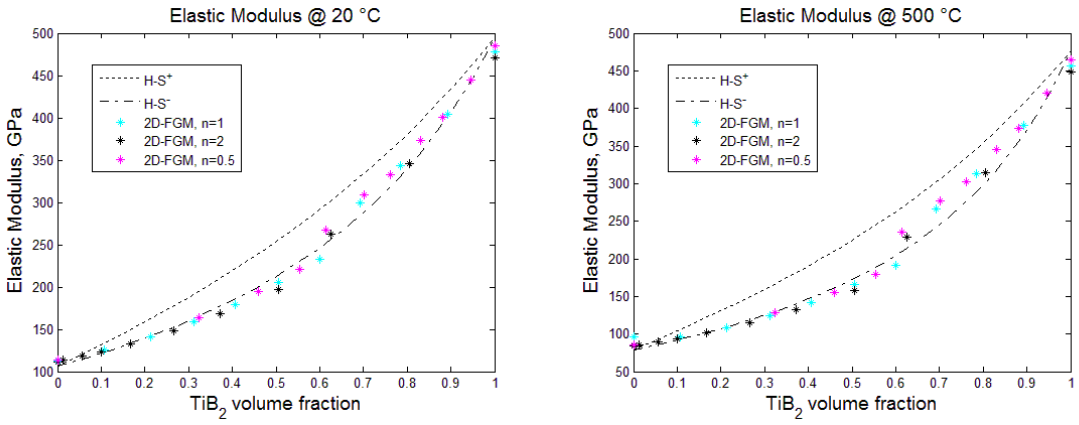

(a) (b)

Figure 4.12. Effective elastic modulus (a) 20 °C and (b) 500 °C, continuous models.

Examining Fig. 4.10, it can be seen that the effective elastic modulus estimation for the Layered and Continuous RVE approaches are similar to one another and fall within or close to the rigorous bounds. Furthermore, upon reviewing Figs. 4.11-4.12, it can be concluded that the 2D models predict slightly lower values for the effective elastic modulus, particularly at volume fractions below the transition zone (in this case, below 0.6). These differences can be attributed to the assumption of generalized plane strain made for the 2D models. Moreover, upon examination of Fig. 4.12, modeling of the material grading appears to have little effect on the estimation of the effective elastic property determination, indicating that the LRVE approach is adequate to accurately estimate the effective composite property for the material parameters. Additionally, the effective elastic response has a similar trend to that of the 3D RVE, but not the exact results. Once again, differences here can be attributed to the plane strain assumption made.

4.4.1.2 Thermoelastic Response

The CTE of the RVE is estimated by increasing the temperature of the RVE over the entire domain from a reference zero strain state and volume averaging the stress and strain throughout the RVE. Due to a mismatch in the CTE of each phase material, a resulting mechanical strain is produced within the body. Therefore, the total strain ϵ, is given as

$$\epsilon = \epsilon_m + \epsilon_{th} \tag{4.2}$$

where ϵ_m and ϵ_{th} are the mechanical and thermal strains, respectively. For convenience, the thermal strain can also be written as

$$\epsilon_{th} = \alpha^*(T - T_0). \tag{4.3}$$

Here, α^* is the effective CTE, and T_0 and T are the initial and final temperature, respectively. Thus, assuming a linear CTE and zero strain at T_0, the effective CTE α^* is determined as

$$\alpha^* = \frac{\bar{\epsilon} - \bar{\epsilon}_m}{(T - T_0)} \tag{4.4}$$

where $\bar{\epsilon}$ and $\bar{\epsilon}_m$ are the average total and mechanical strains, respectively, which are computed in a fashion similar to that used in Eq. (2.51). The computational thermal expansion results for 2D and 3D layered RVEs as well as 2D continuous RVE can be seen compared to the rigorous bounds of Schapery [13] and the approximations of Turner [10] and ROMs [3, 4], Eqs. (2.27), (2.28), (2.24), (2.22) and (2.23), respectively, in Fig. 4.13. In the following figures, the Schapery bounds are denoted as Schapery$^+$ and Schapery$^-$ for the upper and lower bounds, respectively. Figures 4.14-4.15 provide

detailed results of each modeling technique (Layered and Continuous) compared to the rigorous bounds of Schapery.

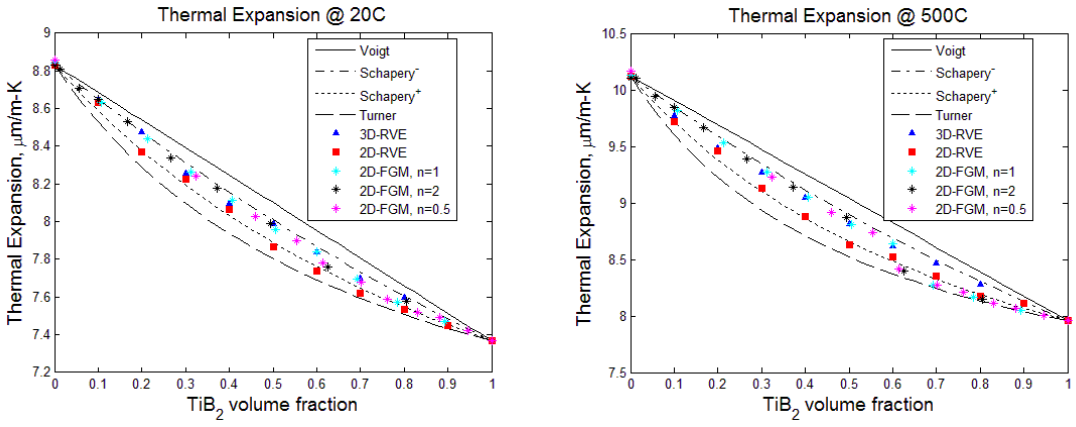

(a) (b)

Figure 4.13. Effective coefficient of thermal expansion (a) 20 °C and (b) 500 °C, all models.

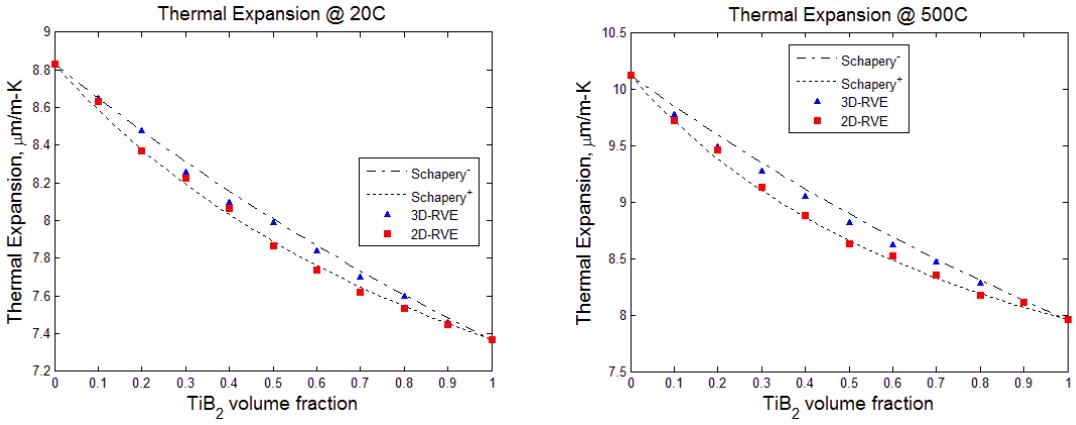

(a) (b)

Figure 4.14. Effective coefficient of thermal expansion (a) 20 °C and (b) 500 °C, layered models.

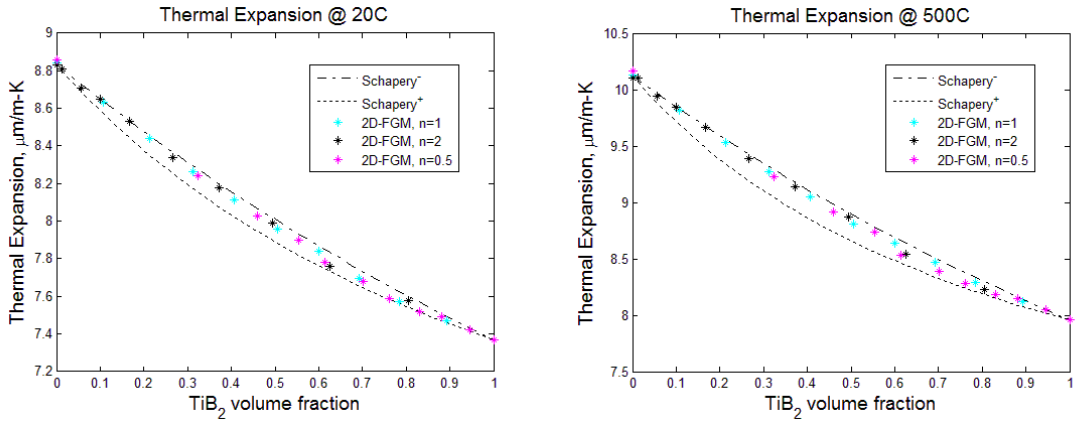

(a) (b)

Figure 4.15. Effective coefficient of thermal expansion (a) 20 °C and (b) 500 °C, continuous models.

As seen in the above figures, the effective CTE falls within or on the rigorous bounds of Schapery. In addition, the choice of RVE appears to have little effect on the estimation of the effective property. Similar to the stress-strain response, the differences in the 2D RVE models (layered and continuous) from the 3D RVE could be attributed to the plane strain assumption used.

4.4.1.3 Steady-State Thermal Response

The effective RVE thermal conductivity is assessed by applying a specified temperature gradient across two faces of the RVE while insulating the remaining faces and assuming a steady-state condition. The temperature gradients and heat fluxes are then volume averaged to determine the effective thermal conductivity k^* as determined by

$$k^* \nabla \bar{T} = -\bar{q} \tag{4.5}$$

where the average temperature gradient, $\nabla \bar{T}$, and average heat flux, $\bar{q}$, are calculated in a fashion similar to Eq. (2.51). For layered RVEs, a temperature gradient is enforced using

PBCs to create a difference across two of the RVE faces/edges, while maintaining equivalent temperature change across the remaining faces of the RVE. In continuous models, a temperature gradient is applied along the grading direction. The thermal conductivity analysis results can be seen at 20 and 500 °C in Fig. 4.16, compared to the bounds of Hashin and Shtrikman [20], Wiener [16] and the approximation of Bruggeman [17] (Eqs. (2.39), (2.40), (2.34), (2.33) and (2.35), respectively). Figures 4.17-4.18 provide detailed results of each modeling technique (Layered and Continuous) compared to the rigorous bounds of Hashin and Shtrikman.

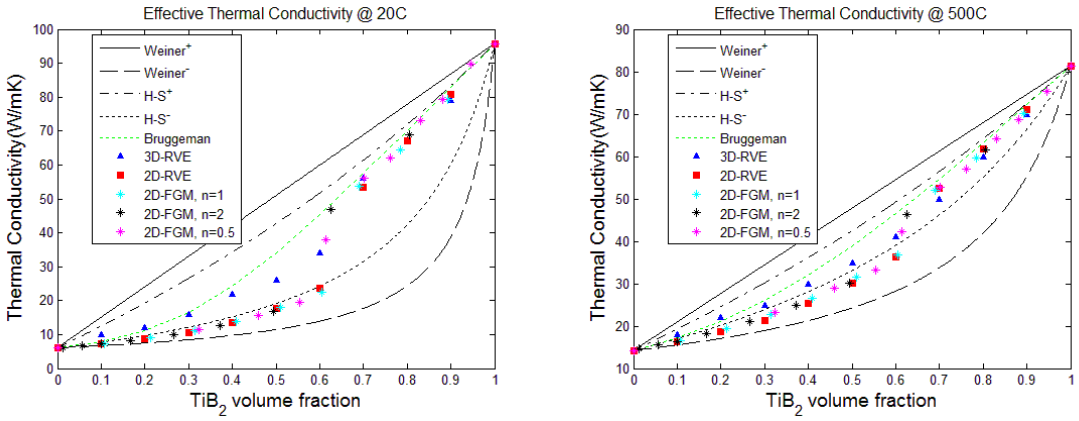

(a) (b)

Figure 4.16. Effective thermal conductivity (a) 20 °C and (b) 500 °C, all models.

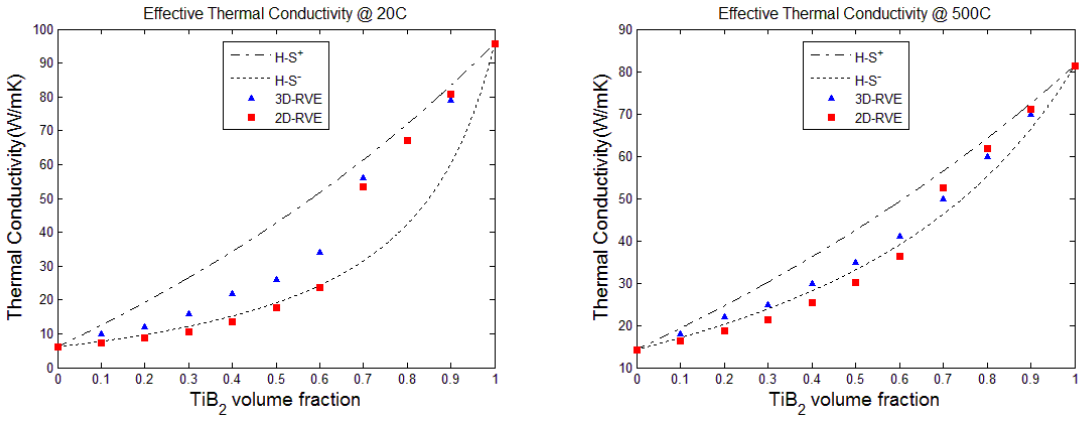

(a) (b)

Figure 4.17. Effective thermal conductivity (a) 20 °C and (b) 500 °C, layered models.

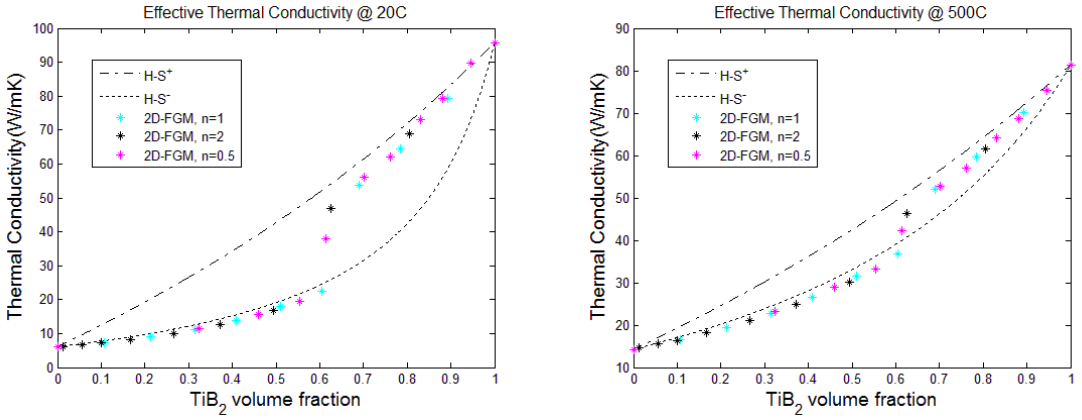

(a) (b)

Figure 4.18. Effective thermal conductivity (a) 20 °C and (b) 500 °C, continuous models.

Referring to the above figures, it is seen that the effective thermal conductivity results for each model are in fair agreement with one another. Similar to the other effective properties, the 2D RVE and 2D FGM RVE predict slightly lower results than the 3D RVE model, up to around 60% volume ceramic content, after which the models all predict similar effective thermal conductivity. Furthermore, all models exhibit similar behavior when the constituent phase materials are switched, as is the case when ceramic

volume fractions exceed 0.6. This observation emphasizes the importance of the transition zone on the determination of the effective properties through numerical and analytical approaches. In these cases, a distinct jump in the effective thermal conductivity is observed, particularly for lower temperatures (i.e., 20 °C), where there exists a larger contrast in constituent thermal conductivity. This behavior appears to be consistent with intuition, as the thermal transport increases as one would expect when a higher thermal conductivity material encompasses a lower conductivity material. Numerical simulations of the effect of the transition zone on the apparent composite material parameters will be presented in Section 0.

4.4.1.4 Transient Thermal Response

The effective RVE specific heat is determined by applying a uniform heat source to the body RVE and assuming a transient condition to allow the temperature to steadily increase with time. The temperature gradients and heat fluxes are then volume averaged to determine the effective specific heat c_p^* as determined by

$$\bar{Q} = C_p^* \, \bar{\rho} \frac{d\bar{T}}{dt} \tag{4.6}$$

where the average heat body flux, $\bar{Q}$, and average temperature change with respect to time, $d\bar{T}/dt$, can also be determined using Eq. (2.51) with proper variables and with a fixed time step of 0.01. The uniform heat source $\bar{Q}$ is applied to the entire model as a heat body flux, with the average density $\bar{\rho}$ calculated using the ROM of Eq. (2.45). Figure 4.19 presents the transient thermal response for the three models compared to the bounds of Rosen and Hashin [14] and the mixture rule of Koop's Law [29], Eqs. (2.46), (2.47) and (2.44), respectively.

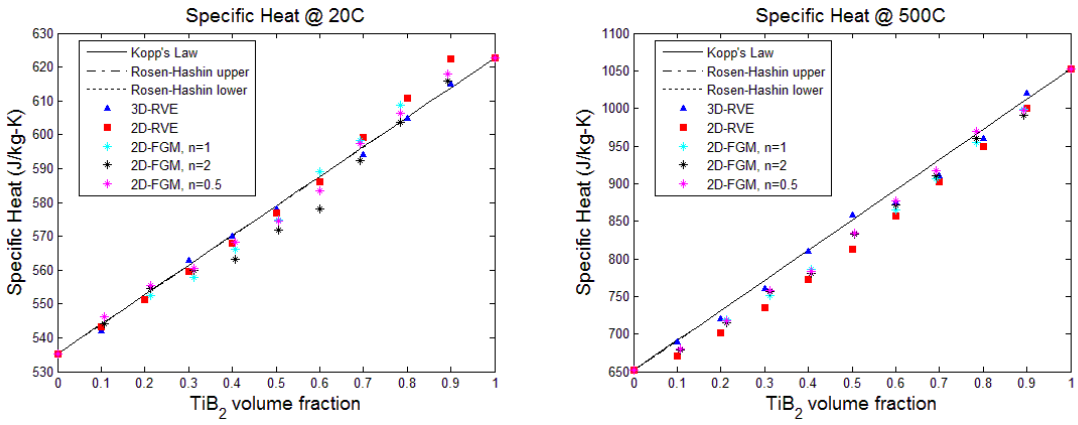

(a) (b)

Figure 4.19. Effective specific heat (a) 20 °C and (b) 500 °C, all models.

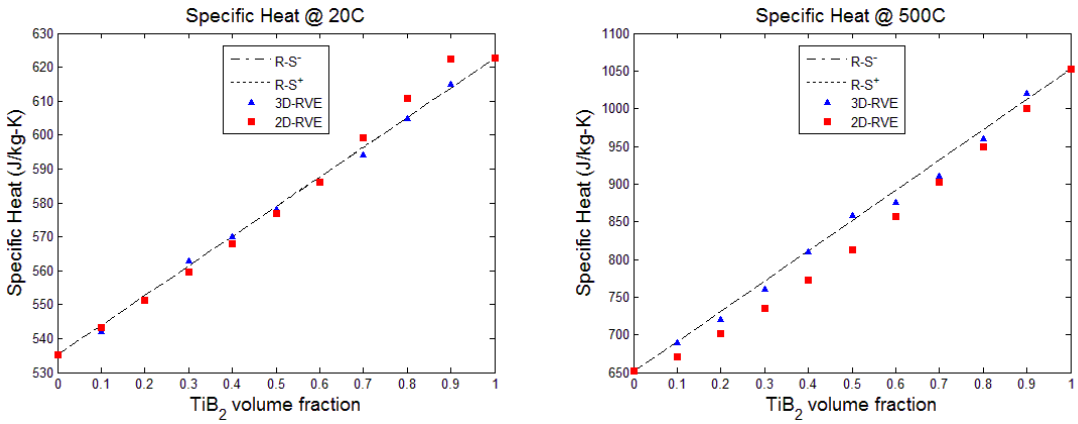

(a) (b)

Figure 4.20. Effective specific heat (a) 20 °C and (b) 500 °C, layered models.

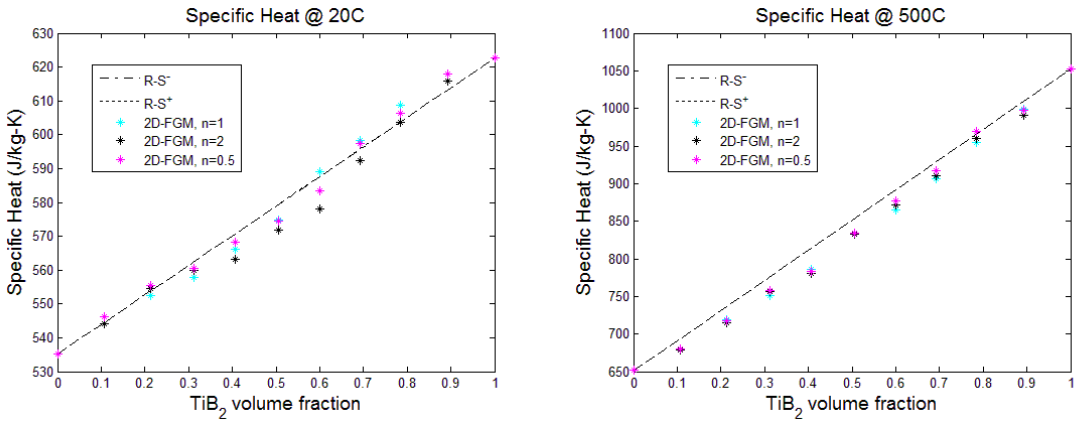

(a) (b)

Figure 4.21. Effective specific heat (a) 20 °C and (b) 500 °C, continuous models.

Examining the above figures, we can see that the analytical model approximations are, for the most part, coincident. This similarity in approximation is due to a combination of the lack of contrast in key material properties, such as density, specific heat and thermal expansion, all of which contribute to the estimation of the effective specific heat models. The 3D RVE effective specific heat prediction is well approximated by the analytical models, while the 2D RVE and 2D FGM models predict effective values close to or less than those of the analytical models. Furthermore, as with the other effective properties, the influence of the grading appears to be negligible on the estimation of the effective specific heat between the 2D-FGM models.

4.4.2 One-Dimensional Material Variation, 3D Geometry

In the previous analysis we considered the effective properties of a Ti/TiB_2 FGM with grading in the through-thickness direction using simplified disks to model the inclusion phase. In the following study, we seek to obtain the same effective material properties by modeling the FGM as a three dimensional body using spherical inclusions using the same linear, quadratic and square root material distribution functions as

described in Fig. 4.5. The same discretization schedule used in the 2D geometry case is also adopted here in the 3D, although a 2 *mm* section is used with 21 layers, and a more computationally forgiving particle radius of 0.015 is used. Figure 4.22 provides samples of each of the volume fraction distribution models with spherical inclusion geometry. Following the same homogenization procedure outlined and used previously, the resulting elastic and thermoelastic response at 20 °C averaged over five artificially generated microstructures for each distribution compared to the H-S and Schapery bounds, respectively, is provided in Fig. 4.23.

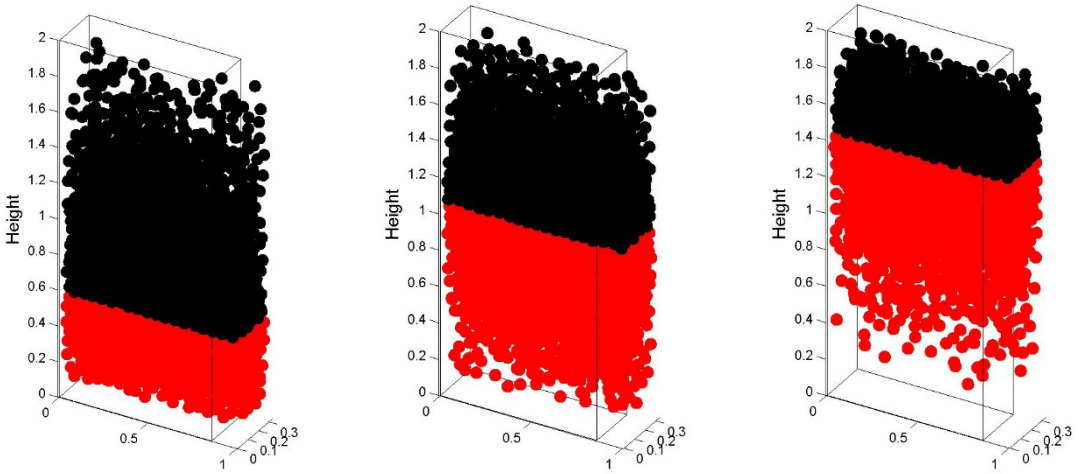

(a) (b) (c)

Figure 4.22. Artificially generated continuous FGM RVE microstructures with spherical inclusions, (a) *n=0.5*, (b) *n=1*, and (c) *n=2*.

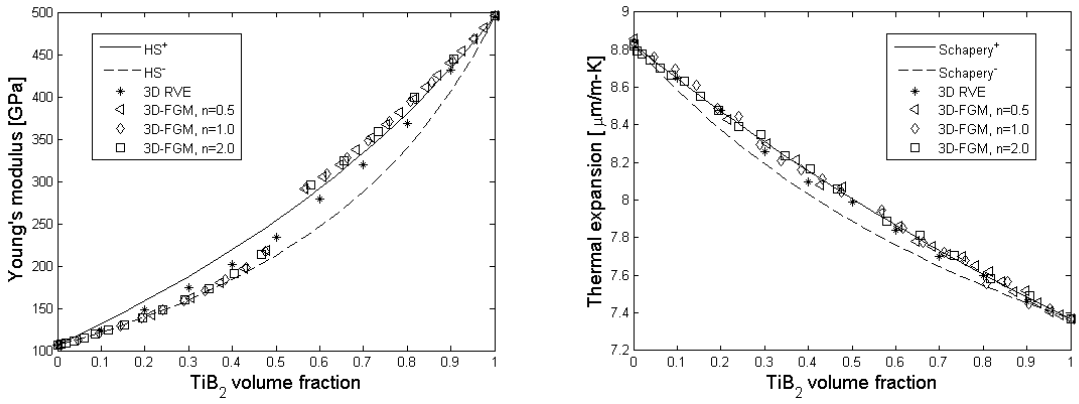

(a) (b)

Figure 4.23. Effective (a) elastic modulus and (b) CTE at 20 °C, 1D grading with 3D geometry.

Examining the above figures, we can see that the through-thickness FGM with 3D geometry is closely approximated by the 3D LRVE with the 3D continuous elastic model being slightly outside of the H-S upper bound for reinforcement volume fractions above the swapping fraction of 0.5. Moreover, each of the grading profiles predict similar values regardless of the material variation for both the elastic and thermoelastic response. Furthermore, when comparing Figs. 4.23, 4.10 and 4.11, the 3D models (3D-FGM and 3D-RVE) tend to predict stiffer effective Young's modulus values when compared to their 2D counterparts. All of this could be accounted for by the fact that the 2D models assume a plane strain condition, which in some cases may not be a valid assumption. The steady-state and transient thermal responses have also been studied to compare the predicted values obtained by 3D models to those by 2D. Figure 4.24 provides a comparison of such properties for each modeling approach.

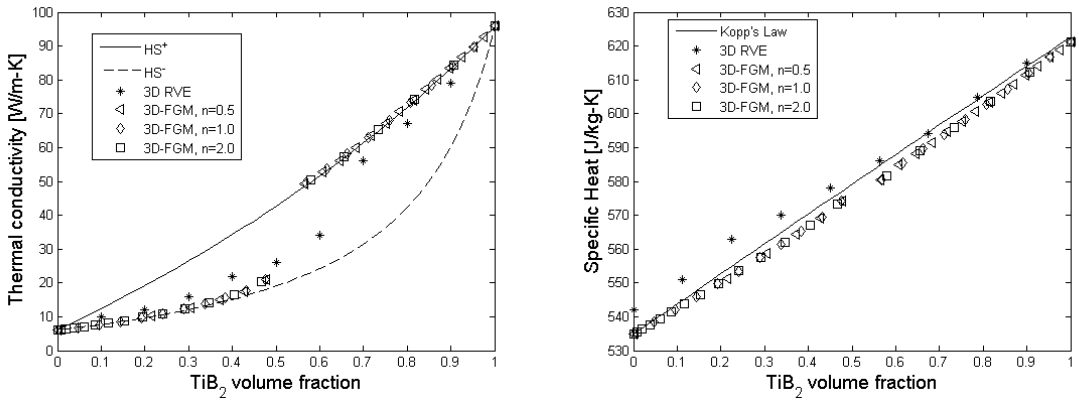

(a) (b)

Figure 4.24. Effective (a) thermal conductivity and (b) specific heat at 20 °C, 1D grading with 3D geometry.

Referring to the above figure, it can be seen that the predicted effective thermal conductivity values from the 3D-FGM model are similar to those obtained by the 3D RVE model, particularly at volume fractions about 0.6. An interesting observation is the estimated value of each model at approximately 60% TiB2 content. Here, large differences are observed between the two modeling approaches. This, however, can be explained by the differences in phase swapping used between the two models. In the case of the 3D RVE, phase swapping occurs at volume fractions above 0.6, while 3D FGM models swap the inclusion phases at 0.5. These differences are a direct result of the user-defined swapping volume fraction, which will be addressed in great detail in Section 4.5 to follow.

4.4.3 Two-Dimensional Material Variation, 3D Geometry

As previously mentioned, the predominant characteristic of FGMs is the ability to tailor material properties to best suit the anticipated loading conditions and desired response. As highlighted in CHAPTER 4, our proposed model is capable of modeling materials with variation of constituent materials in more than one principal direction.

Hence, the objective of this section is to highlight the effective properties of FGMs exhibiting material variation in two directions using the present modeling approach. Using the same Ti/TiB_2 material properties described in the previous sections, the 2D material variation is modeled using 3D geometry and the 2D power law equation Eq. (3.2) along with the material variation parameters provided in Table 4-2. Figure 4.25 provides visual illustration of the resulting 2D material variation. Examples of the resulting 2D material variation geometry are provided in Fig. 4.26.

Table 4-2. Grading parameters for 2D Ti/TiB_2 FGMs.

Model	Mdl-1	Mdl-2	Mdl-3
Layers	21	21	21
Sections	10	10	10
n_z	0.5	1	2
n_x	0.5	1	2
η_z	1	1	1
η_x	1	1	1
η_{max}	1	1	1

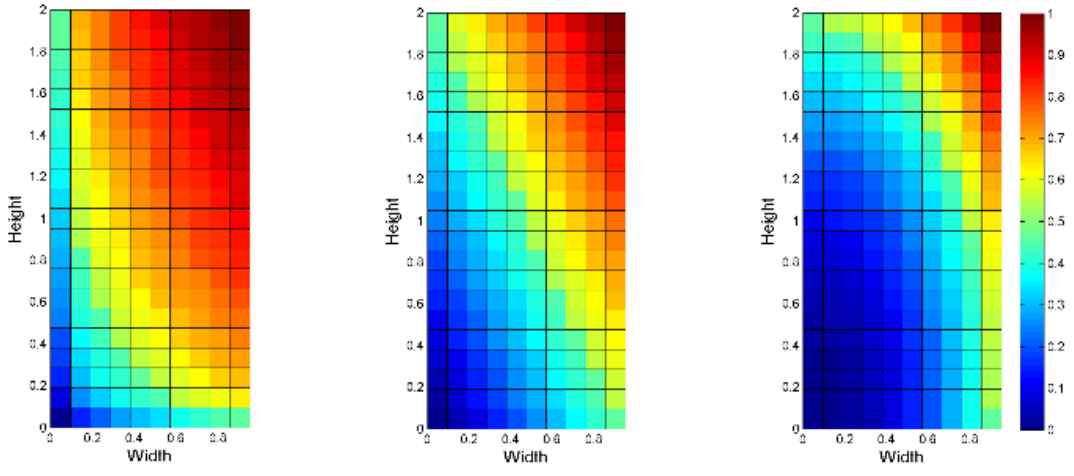

(a) (b) (c)

Figure 4.25. Artificially generated continuous 2D FGM RVE volume fraction distribution, (a) $n_z = n_x = 0.5$, (b) $n_z = n_x = 1$, and (c) $n_z = n_x = 2$.

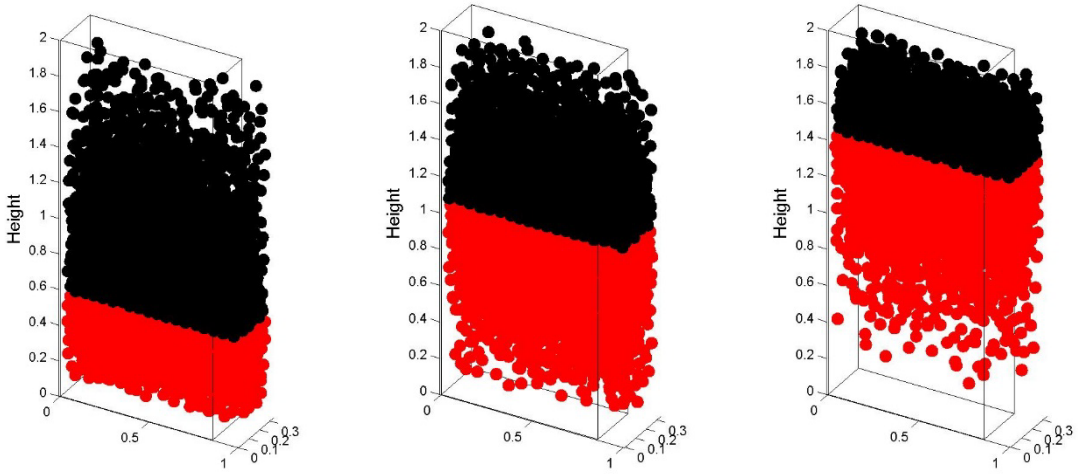

(a) (b) (c)

Figure 4.26. Artificially generated continuous 2D FGM RVE microstructures with spherical inclusions, (a) $n_z = n_x = 0.5$, (b) $n_z = n_x = 1$, and (c) $n_z = n_x = 2$.

Conducting numerical homogenization on each layer (through-thickness) and section (in-plane), the predicted elastic responses at 20 °C averaged over three artificially generated microstructures for each distribution are compared to the H-S bounds and plotted as color maps as a function of spatial orientation as shown in Fig. 4.27.

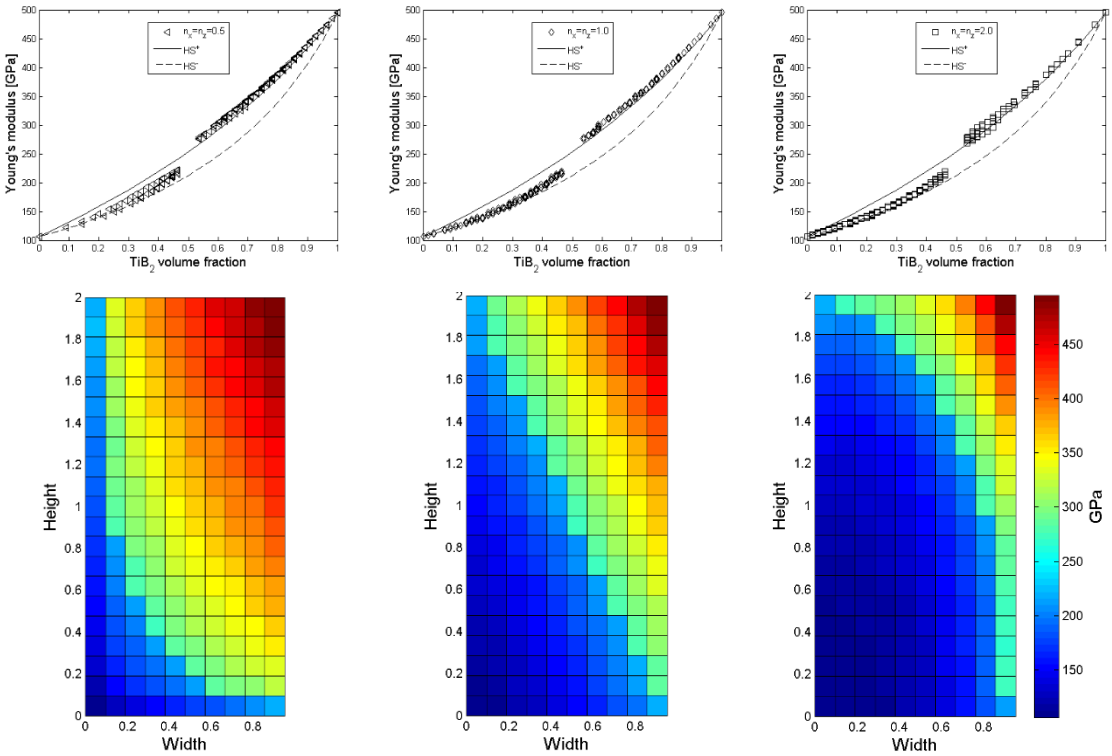

(a) (b) (c)

Figure 4.27. Effective Young's modulus at 20 °C for (a) Mdl-1 (b) Mdl-2 and (C) Mdl-3, for 2D grading with 3D geometry.

As can be inferred from the above figure, the predicted values are similar to those obtained for 1D graded materials with 3D geometry. Moreover, the resulting effective property for each volume fraction depends on its location with Mdl-1 and Mdl-3 exhibiting larger variations in the apparent effective property. This suggests that the surrounding volume fractions in each of the directions influence the effective elastic response. This spatial dependence can also be seen when investigating the effective thermoelastic response as shown in Fig. 4.28. Here, it can be seen that similar to the effective elastic response, while seemingly small, the location with respect to neighboring volume fractions appears to play a role in the effective thermoelastic response.

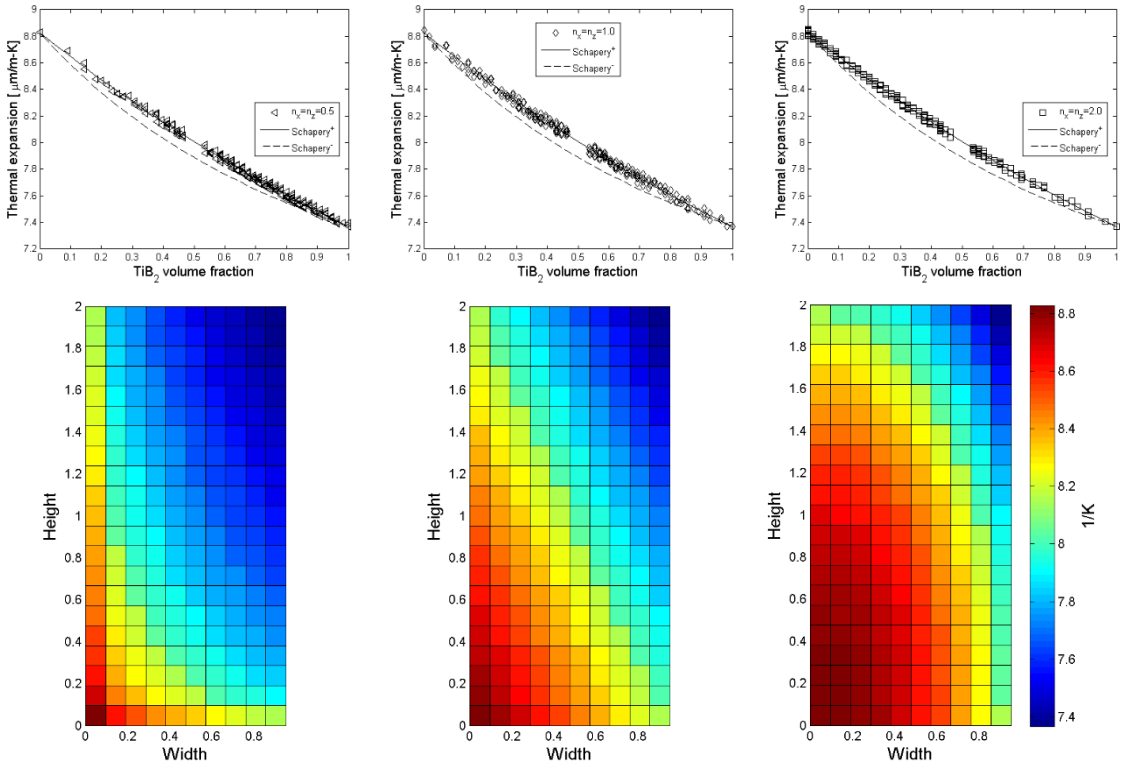

(a) (b) (c)

Figure 4.28. Effective CTE at 20 °C for (a) Mdl-1 (b) Mdl-2 and (C) Mdl-3, for 2D grading with 3D geometry.

Additionally, the steady-state and transient thermal responses have also been investigated to determine the effect of 2D material variation on the effective thermal response. Figure 4.29 provides the resulting effective thermal conductivity, while Fig. 4.30 displays the apparent specific heat.

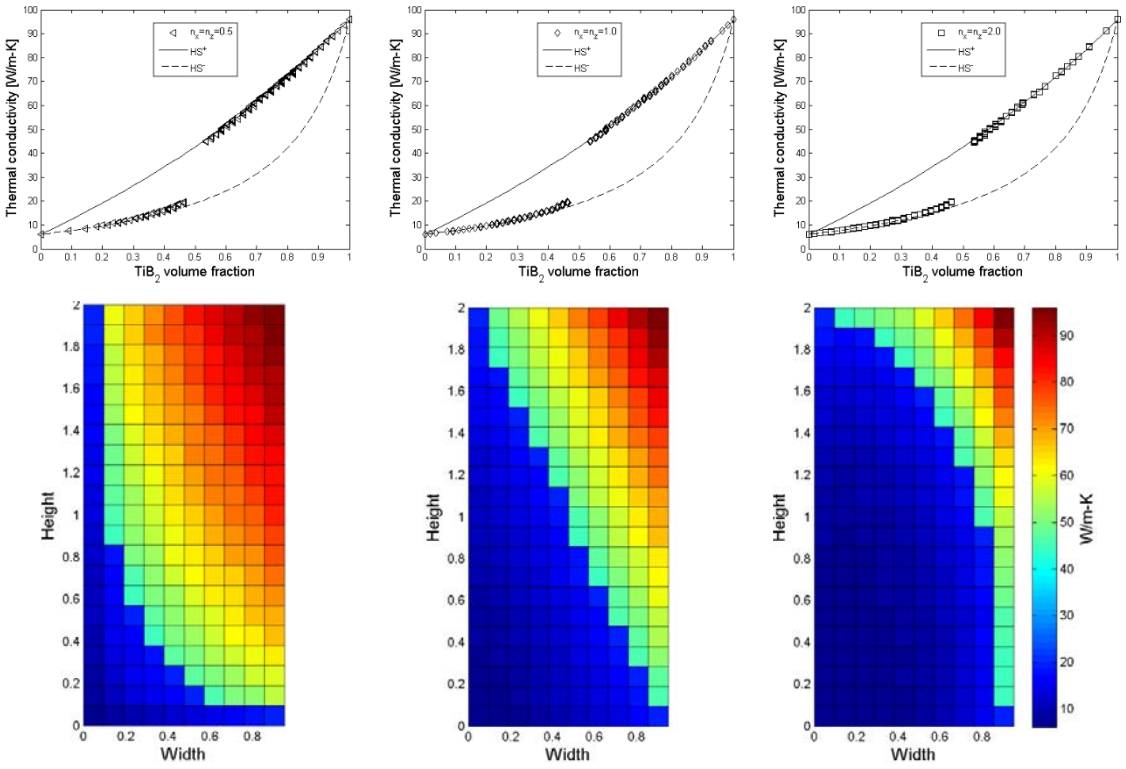

(a) (b) (c)

Figure 4.29. Effective thermal conductivity at 20 °C for (a) Mdl-1 (b) Mdl-2 and (C) Mdl-3, for 2D grading with 3D geometry.

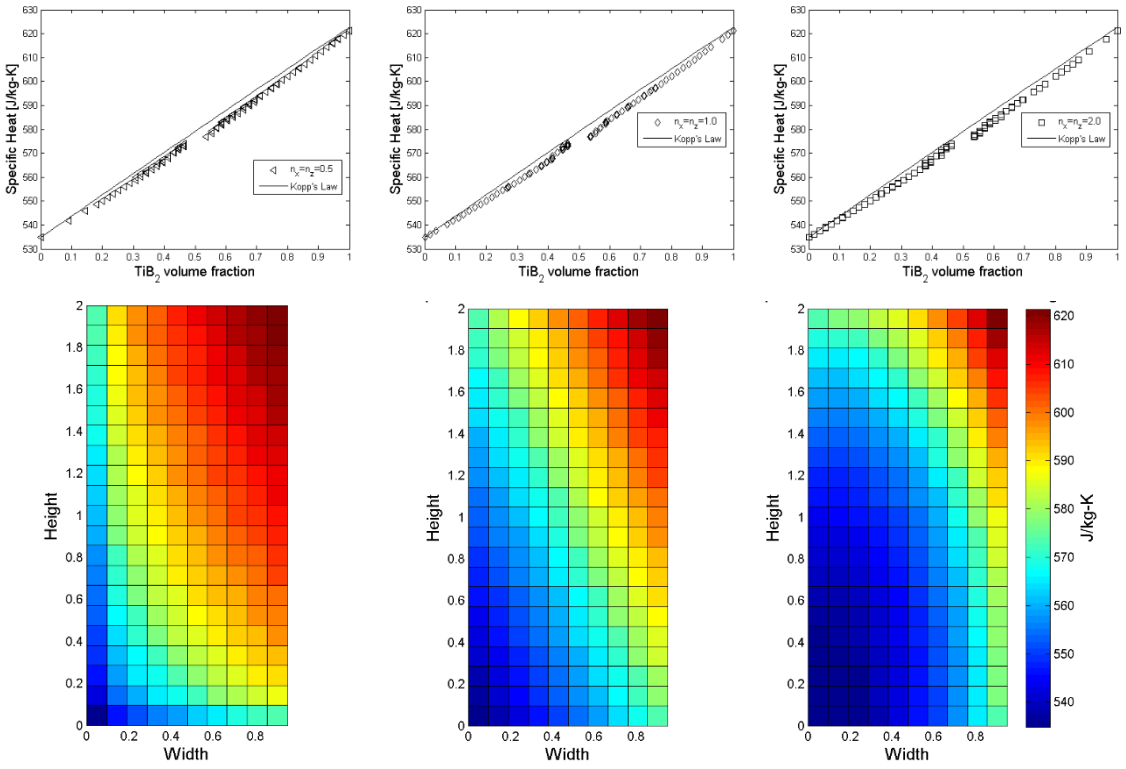

(a) (b) (c)

Figure 4.30. Effective specific heat at 20 °C for (a) Mdl-1 (b) Mdl-2 and (C) Mdl-3, for 2D grading with 3D geometry.

Referring to Figure 4.29, the effective thermal conductivity displays a similar response when compared to other modeling approaches and geometric considerations (LRVE vs. FGM and 2D vs. 3D). This suggests that there is less of a spatial dependence on the effective steady-state thermal response when compared to the elastic; as can be seen, there is less variation in the effective thermal conductivity for each region of similar TiB_2 volume fraction. Most notable is the distinct jump in the predicted effective value after the phase swapping fraction, which will be addressed in the following section. Similarly, the effective specific heat (Fig. 4.30) displays little dependence on the spatial location or surrounding volume distribution as its property is well estimated by Koop's Law.

4.5 Effects of Transition Zone

In this work, the transition zone is defined as the volume fraction at which the constituent material phases are reversed. The motivation for this definition stems from considering the material composition of a graded composite. In such composites, the material variation evolves from a dominant phase-1 to phase-2 material. Throughout this evolution, there will exist regions where it will be difficult to distinguish the matrix from the reinforcement phase. This transition zone will greatly depend on the manufacturing process controlling the morphology of the constituents and the interactions of the materials at the micro level.

As can be seen in the examples from Section 4.4 (particularly the thermal conductivity), selection of the volume fraction at which to switch the constituent phase materials plays a significant role in the estimation of the local effective property (see Fig. 4.31). As can be deduced from this observation, determination of the effective local property will become even more clouded when contrast in the material properties increases. To investigate this transition or jump further, an example problem consisting of a 1-unit thickness 2D linearly graded (n=1, η=1) Ti/TiB_2 system is evaluated using transition zones (swapped phases) of 0.40, 0.50 and 0.60 volume fractions. For clarification, at volume fractions at or below the transition zone, TiB_2 acts as the reinforcement phase, while Ti performs the role of matrix. Above this transition zone, the phase materials are switched. Applying the same modeling principles used in Section 4.4, the effective elastic modulus, coefficient of thermal expansion, thermal conductivity and specific heat averaged over three randomly generated models are computed. Figures 4.32 and 4.33 provide the effective property results with respect to volume fraction (thickness coordinate) and the assumed volume fraction of the transition zone. In these plots, trans-04, trans-05 and trans-06 designate the 40%, 50% and 60% transition zones.

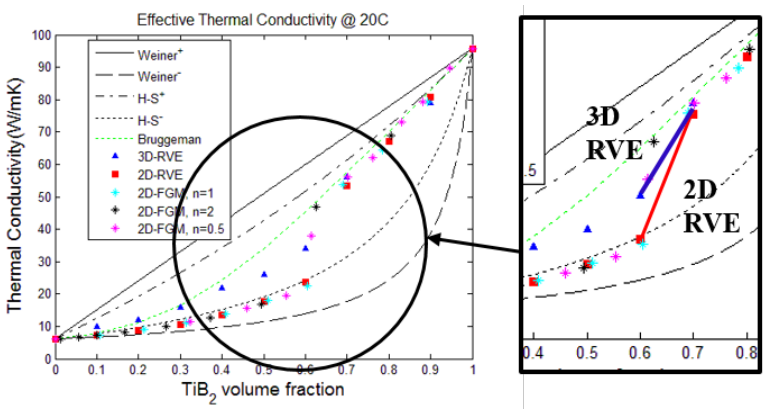

Figure 4.31. Effective thermal conductivity jump after transition zone.

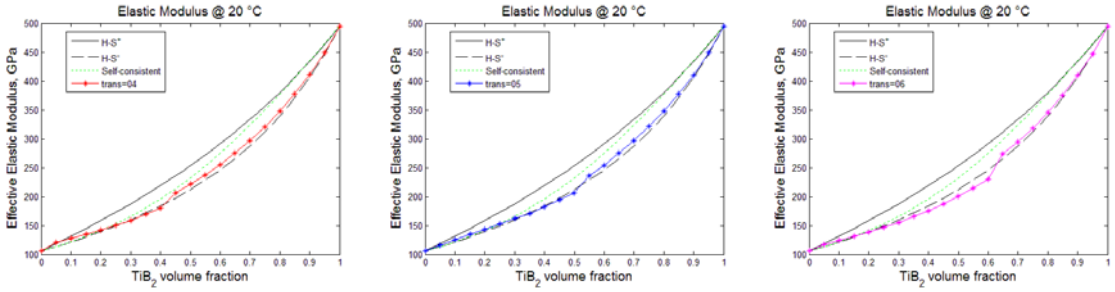

(a) (b) (C)

Figure 4.32. Effective elastic modulus at 20 °C and transition zone volume fractions of (a) 0.4 (b) 0.5 and (c) 0.6.

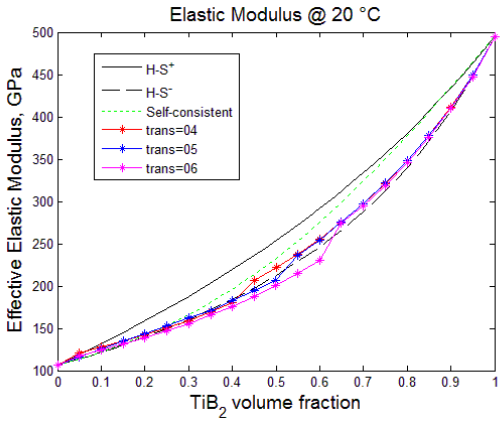

Figure 4.33. Effective elastic modulus at 20 °C with varying transition zones.

As shown in the above figures, the effective elastic modulus tends to be well estimated by the H-S lower bound. When the reinforcement volume fractions exceeds that of the transition zone volume fraction there is a distinct jump in the apparent elastic modulus. This jump in apparent property is further emphasized when considering the steady-state thermal response as provided in Figs. 4.34 and 4.35 below.

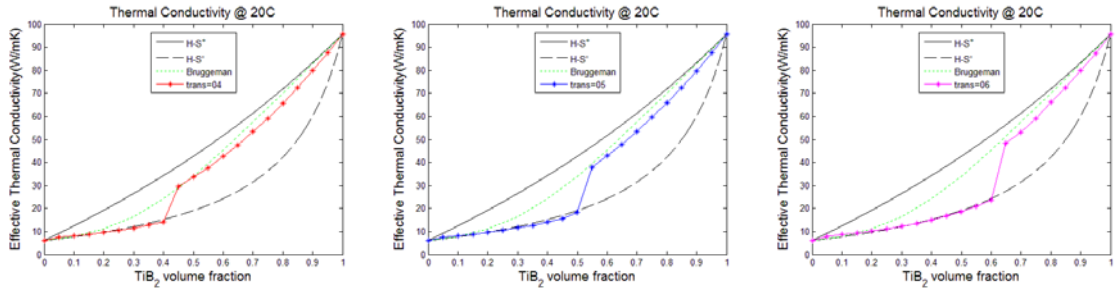

(a) (b) (C)

Figure 4.34. Effective thermal conductivity at 20 °C and transition zone volume fractions of (a) 0.4 (b) 0.5 and (c) 0.6.

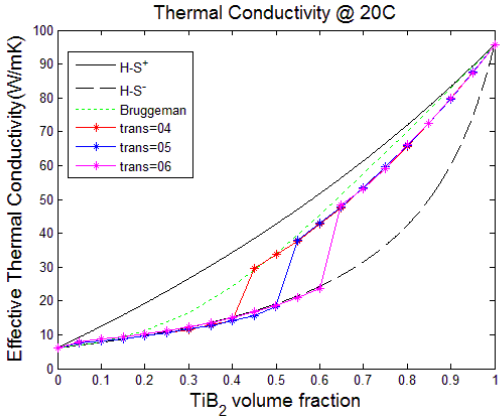

Figure 4.35. Effective thermal conductivity at 20 °C with varying transition zones.

As can be seen in Figs. 4.34 and 4.35, the effective thermal conductivity estimation further highlights the significance of determining the location of the material transition zone. The effective property tends to be well estimated by the H-S lower bound for reinforcement volume fractions less than or equal to the transition zone. In the case when

the reinforcement volume fraction exceeds the transition zone, there exists a distinct jump in the calculated effective property to approximately the Bruggeman or self-consistent approximation. To complete the transition zone study, a thermoelastic and transient thermal response were also investigated for the Ti/TiB_2 graded system. Figures 4.36-4.39 provide the results of this work.

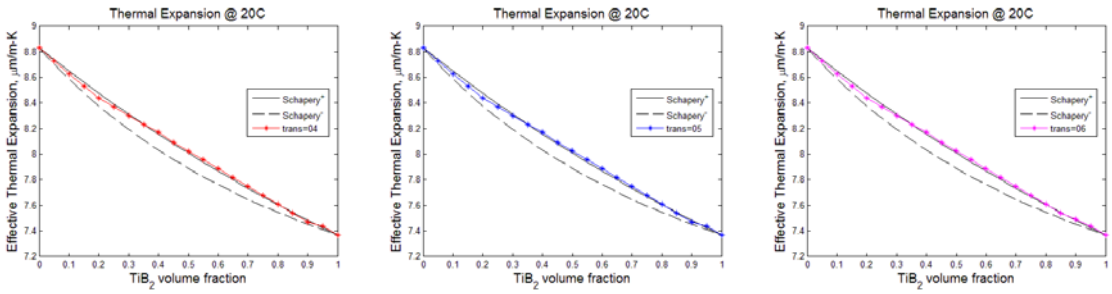

(a) (b) (C)

Figure 4.36. Effective coefficient of thermal expansion at 20 °C and transition zone volume fractions of (a) 0.4 (b) 0.5 and (c) 0.6.

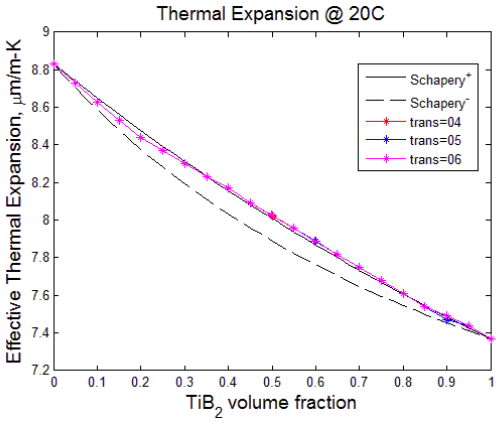

Figure 4.37. Effective coefficient of thermal expansion at 20 °C with varying transition zones.

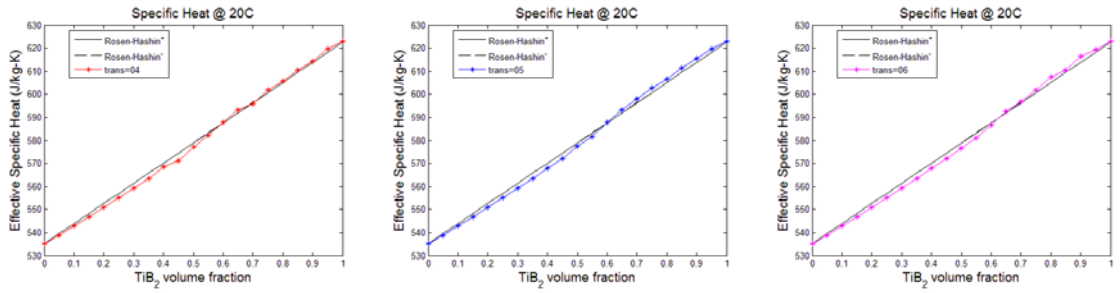

(a) (b) (C)

Figure 4.38. Effective specific heat at 20 °C and transition zone volume fractions of (a) 0.4 (b) 0.5 and (c) 0.6.

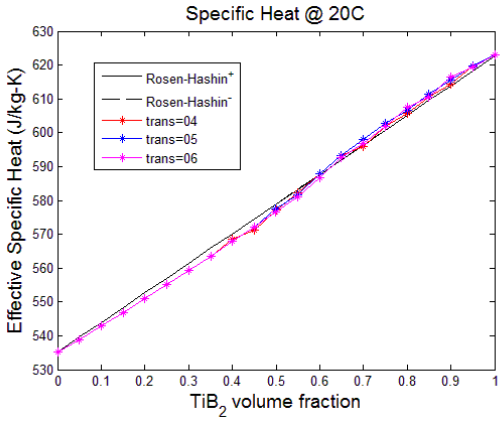

Figure 4.39. Effective specific heat at 20 °C with varying transition zones.

Reviewing Figs. 4.36-4.39, it can be seen that the distinct jump in the estimation of the overall property is not as apparent as in the case of the elastic modulus and thermal conductivity. This response could be explained by the derivation of Schapery's [13] effective CTE. Upon further investigation, it can be seen that the composite CTE is dependent on the bulk modulus of the constituents and the effective composite bulk modulus as well as the CTE of the constituents. In the case of the Ti/TiB_2 system, the CTE of each phase are relatively similar to one another. In addition, while the elastic moduli may have high contrast, the H-S (Eq. (2.12)) effective composite bulk modulus bounds are fairly tight. Here, the maximum difference between the upper and lower bounds for the elastic and bulk modulus are approximately 46.1 and 10.1 GPa, as seen in

Fig. 4.40. This combination of similar CTE properties and tight bounds leads to little deviation in the homogenized values. The same rationale can be applied to the effective specific heat when regarding the Rosen-Hashin [14] formulation.

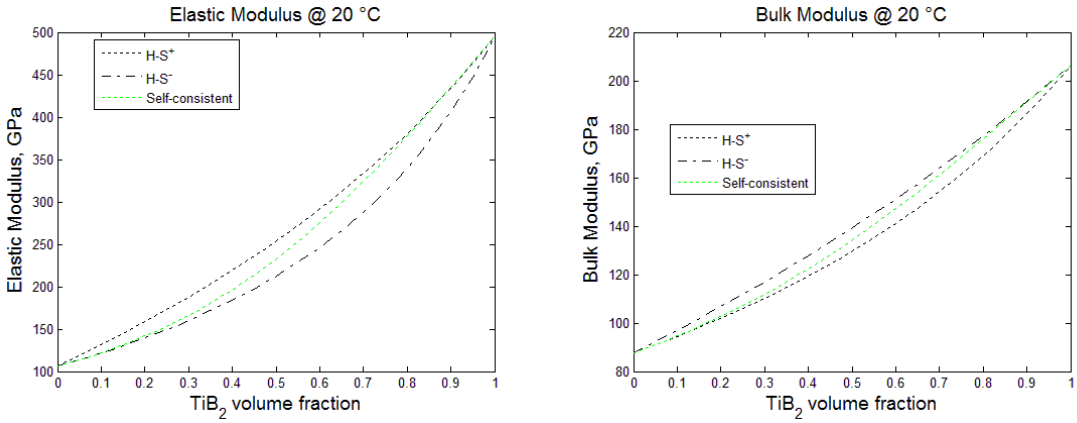

(a) (b)

Figure 4.40. Effective (a) elastic and (b) bulk modulus at 20 °C.

The outcome of this study clearly indicates that the evolution of the material variation is key to an accurate prediction of the local overall effective properties. Particularly for material parameters with high contrast, the local effective property can differ drastically from neighboring properties with little change in the reinforcement volume fraction. In such cases image-based modeling may be beneficial and/or investigation of the material manufacturing process control may be necessary to properly facilitate the modeling of graded microstructures.

4.6 Material Model Validation

In the previous section, the proposed model was verified by comparing the numerically obtained effective material properties to those obtained using the analytical methods. Results of these simulations indicate that the proposed model falls within or very close to rigorous analytical bounds for each respective material property. The aim of this section is to validate the proposed model by comparing the estimated effective

properties to FGM experimentally obtained values available in literature. Because manufactured materials typically contain defects such as voids or porosity, a few of the models in the following validation incorporate a third material phase to address these defects using the same procedure outlined in Sections 4.2.1 and 4.3.1.

4.6.1 Elastic Model Validation

Elastic simulations have been carried out to validate the proposed FEM model using available experimental data found in literature. One such set of experimental data is that of Parameswaran and Shukla [92]. In their study, FGMs were fabricated using cenosphere inclusions and polyester or polyester-plasticizer matrix materials to estimate the effective Young's modulus. The experimental FGM sheet measuring 250x250x12 *mm* was modeled as a 2D plate normalized to a 1x1 plate discretized into 50 layers using a characteristic radius of 0.003. The material distribution varies continuously from 0 to 45% for cenospheres in polyester matrix and cenospheres in polyester-plasticizer with the volume fraction ϕ distributions shown in Fig. 4.41. The Young's Modulus E and Poisson's ratio ν used in the analysis are taken from the work of Yin et al. [77] and are provided in Table 4-3. The resulting Young's modulus predictions of this case study can be seen below in Fig. 4.42.

Table 4-3. Material properties of Cenospheres, polyester and polyester-plasticizer.

Material	E (GPa)	ν
Cenospheres, C	6.0	0.35
Polyester, P	3.6	0.41
Polyester-Plasticizer, P-P	2.5	0.33

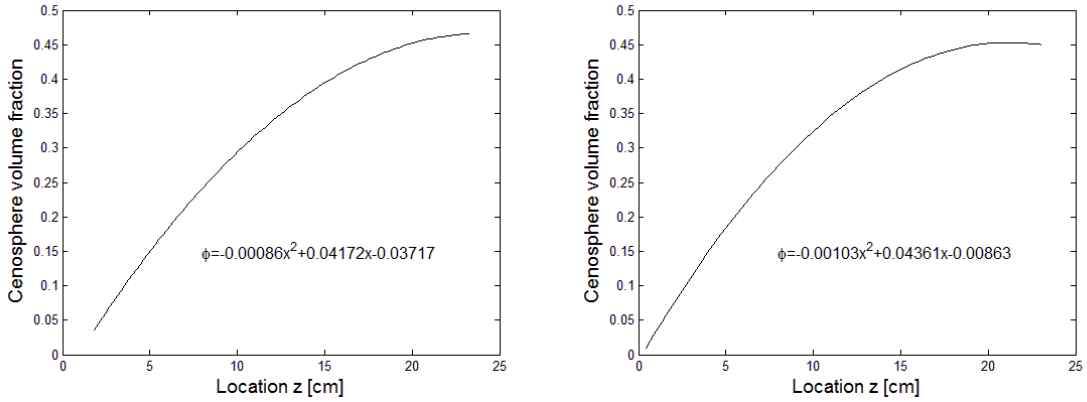

(a) (b)

Figure 4.41. Volume fraction $\boldsymbol{\phi}$ distribution for cenospheres in (a) polyester matrix (b) polyester-plasticizer matrix, reproduced from [92].

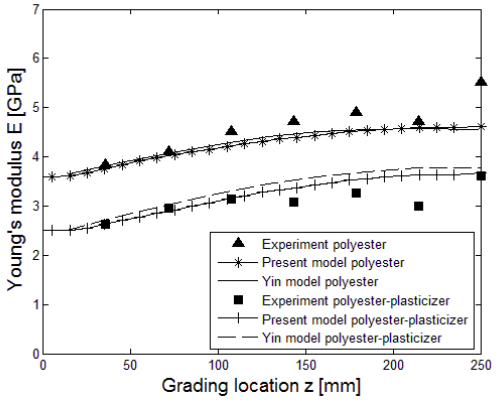

Figure 4.42. Comparisons of effective Cenosphere FGM Young's moduli between the present model simulations, Yin model [77] and experimental data [92] for (a) polyester matrix and (b) polyester-plasticizer matrix.

As can be seen in the above Figure, the proposed FEM compares reasonably well with the experimental data and with the particle interaction analytical model of Yin et al. [77].

To illustrate the flexibility of the proposed model, elastic simulations are also carried out on materials that contain significant amounts of porosity or voids. One such comparison is the effective elastic properties of Ni/MgO and Ni_3Al/TiC graded materials experimental obtained by Zhai et al. [93]. To account for the porosity present in the

manufactured FGMs, a third phase was introduced to our model as voids with null elastic properties, using the nominal values of the experimental measured porosity provided in Fig. 4.43. The voids are modeled as disks and assumed to have a radius half that of the inclusion radius. The elastic properties of the fully dense Ni and MgO are taken to be in line with Voronoi cell finite element model (VCFEM) of Grujicic and Zhang [94] as: $E_{Ni} = 180$ GPa, $\nu_{Ni} = 0.33$, $E_{MgO} = 230$ GPa and $\nu_{MgO} = 0.25$, while the Ni_3Al and TiC are taken as: $E_{Ni_3Al} = 217$ GPa, $\nu_{Ni_3Al} = 0.3$, $E_{TiC} = 440$ GPa and $\nu_{TiC} = 0.19$. Once again, the planar geometry was modeled as a 1x1 plate with a linearly varying TiC and MgO content. The geometry was discretized into 50 layers using a particle radius of 0.005 units and with phase swapping when the inclusion volume fraction exceeded 0.5. The effective Poissons's ratio is determined by dividing the negative of the average transverse strain by the average tensile strain in each layer. Comparisons of the experimental data, VCFEM and the particle interaction model of Yin with the proposed FEM averaged over five models are shown in Figs. 4.44 and 4.45 for Ni/MgO and Ni_3Al/TiC, respectively.

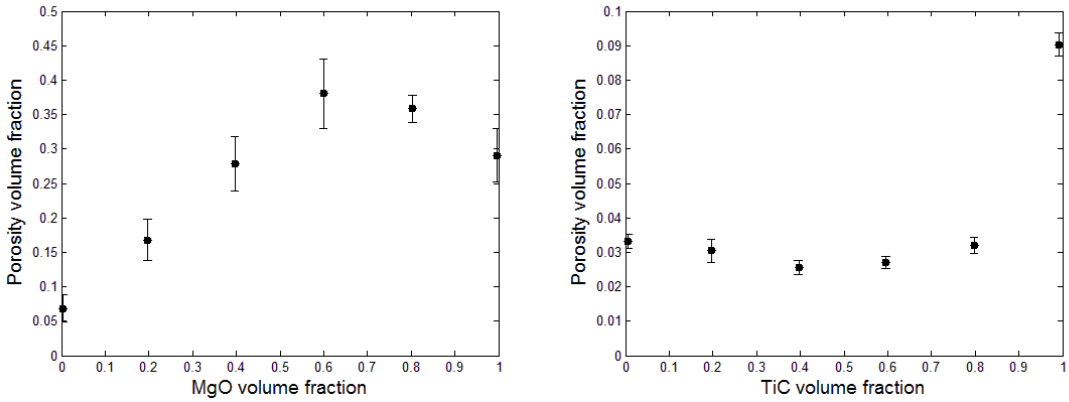

Figure 4.43. Experimentally measured FGM porosity in Ni/MgO and Ni_3Al/TiC FGMs (reproduced from [94]).

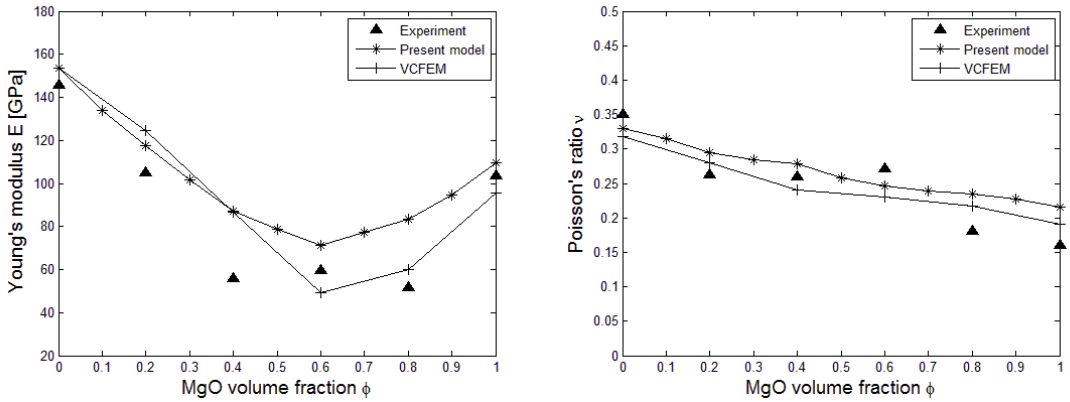

Figure 4.44. Comparisons of Ni/MgO FGM effective Young's modulus and Poisson's ratio between the present model simulations, VCFEM [94], Yin model [77] and experimental data [93].

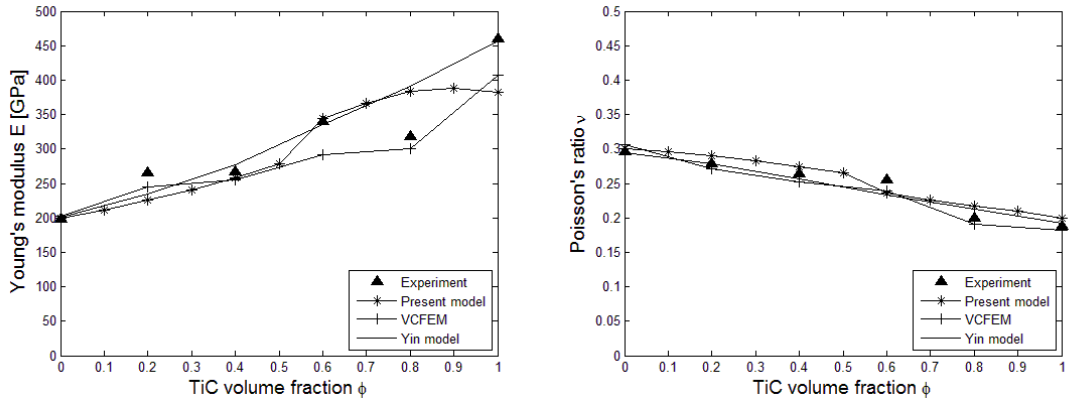

Figure 4.45. Comparisons of Ni_3Al/TiC FGM effective Young's modulus and Poisson's ratio between the present model simulations, VCFEM [94], Yin model [77] and experimental data [93].

As can be seen in Figs. 4.44 and 4.45, the proposed model predicts the effective Young's modulus and Poisson's ratio reasonably well when compared to the experimental data and reference solutions with the best agreement found in the Ni_3A/TiC material system. This could be explained by the fact that the reported porosity in this system is significantly lower than that of the Ni/MgO FGM. At higher volume fractions of porosity, the effects of size, shape and distribution of voids may play a larger role in the effective elastic response as suggested by Shen and Brinson [95]. Thus, it requires a more thorough investigation into the modeling of porosity, which is not within the scope of this

work. Moreover, it should be noted that while the proposed model is in fair agreement with the analytical model of Yin, the current model under predicts the Young's modulus at full TiC concentration (TiC and porosity only). Meanwhile, the model of Yin predicts the exact experimental value. This was not expected by the author as the reported fully dense TiC Young's modulus is less than the experimentally obtained value.

In addition to evaluating the effective elastic response of FGMs, the current model has also been used to analyze the effective response of uniform composites. By reducing the number of layers and sections to one, the FGM model is converted into a classical RVE for fixed volume fraction composites. The user can then define the type of analysis and boundary conditions (periodic, kinematic and homogenous) to impose on the RVE. The process is illustrated by considering the experimental data of Wong and Bollampally [96], who measured the Young's modulus for epoxy matrix composites containing three different types of inclusion materials: silica, alumina and silica-coated aluminum nitride (SCAN). Where silica was spherical, alumina was close to spherical and SCAN was irregular in shape. The material properties of the matrix and inclusion materials are provided in Table 4-4. The RVE used for each material is assumed to be a 1x1 square with disk-shaped inclusions with a radius of 0.02. Tensile loads are applied to the RVE via PBCs, and the effective response is calculated in the same manner as outlined above. Comparisons of the effective Young's modulus for silica, alumina and SCAN inclusion materials are shown in Fig. 4.46. The proposed model is found to be in good agreement with the experimental data which is also well estimated by the H-S lower bound.

Table 4-4. Elastic material properties of Expoy, Silica, SCAN and Alumina.

Material	E (GPa)	ν
Epoxy	2.25	0.19
Silica	73.0	0.19
SCAN	330.0	0.25
Alumina	385	0.24

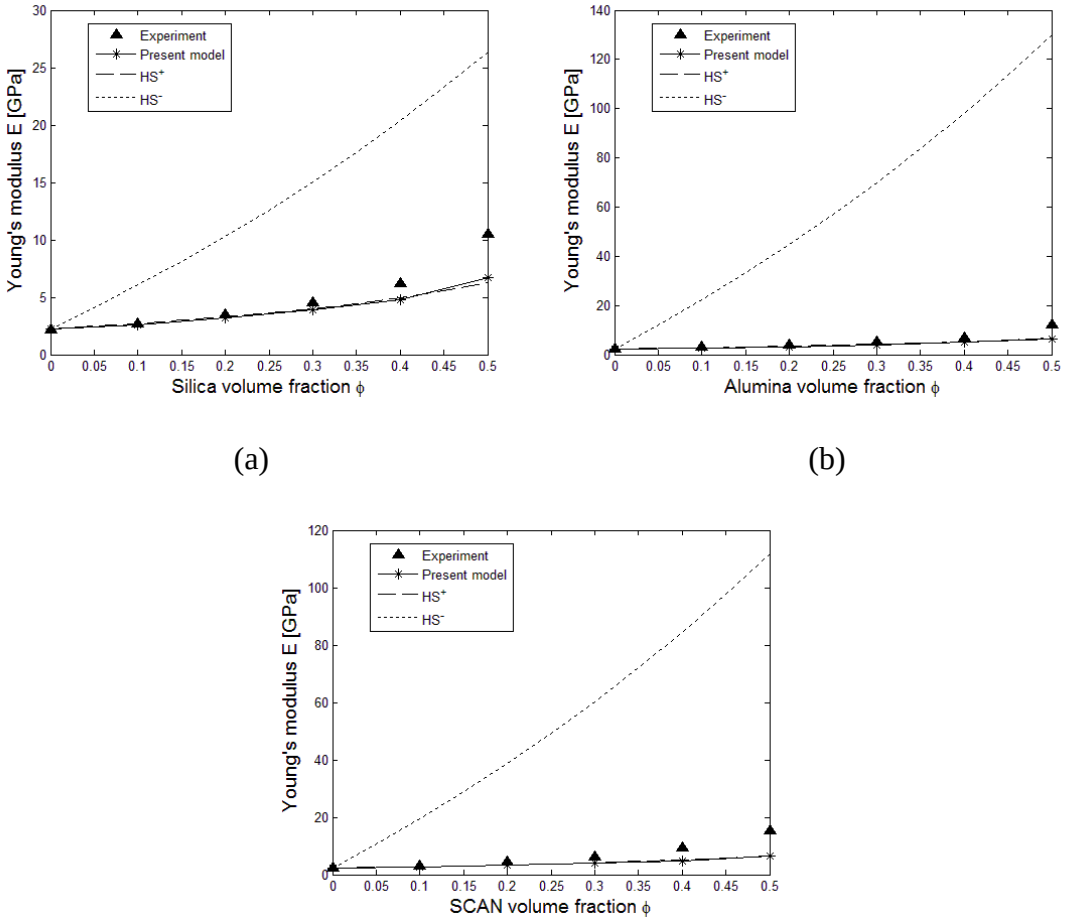

(a) (b)

(c)

Figure 4.46. Comparisons of effective Young's modulus for epoxy matrix composites between present model simulations, Hashin-Shtrikman (HS) bounds [97] and experimental data [96] for (a) silica (b) alumina and (c) SCAN reinforcement materials.

4.6.2 Thermoelastic Model Validation

In addition to the elastic model validation, Thermoelastic simulations have also been completed to validate the accuracy of the FEM in predicting the effective spatial-dependent coefficient of thermal expansion. One such validation simulation uses the experimental data of a Molybdenum-Silicon Dioxide (Mo-$SiO_{2)}$ FGM obtained by Ishibashi et al. [98]. The cylindrical material samples with a diameter of 1.5 cm and height of 2.5 cm were assumed to be a normalized 1.7x1 2D plate discretized into 50 layers with a characteristic particle radius of 0.003. The material properties of Mo and SiO_2 are provided in Table 4-5. The material distribution varies continuously following the distribution approximated by the function shown in Fig. 4.47.

Table 4-5. Mo and SiO_2 material properties.

Material	E (GPa)	ν	α (10^{-6}/K)
Mo	324.0	0.31	5.1
SiO_2	80.4	0.18	0.54

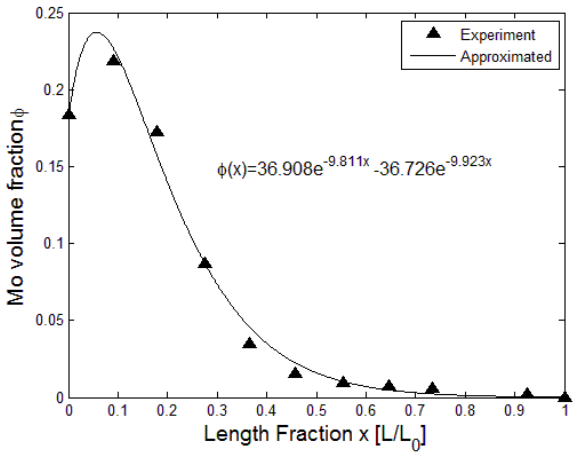

Figure 4.47. Approximate Mo volume fraction $\boldsymbol{\phi}$ distribution and experimentally measured [98].

Referring to Fig. 4.47, the Mo content varies from 0 to approximately 25%; thus, only one particle zone exists in this FGM and does not require transition considerations.

Figure 4.48 shows the comparisons of the predicted spatially variant CTE along the grading direction with the experimental data. As shown, the proposed model provides reasonable agreement with the experimentally obtained data and good agreement with the analytical model offered by Yin et al. [99]. These subtle differences, particularly at higher Mo content, could be explained by the fact that our model assumes monodispersed disks with a random distribution. This excludes any effects due to particle shape or distribution on the effective properties. Moreover, information regarding discovery or notation of porosity is not divulged by the authors, leading to the assumption that zero porosity is present in the manufactured material. Additionally, due to the non-monotonic Mo distribution shown in Fig. 4.47, the effective CTE does not vary monotonically in the grading direction but instead follows a distribution similar to that of the volume fraction.

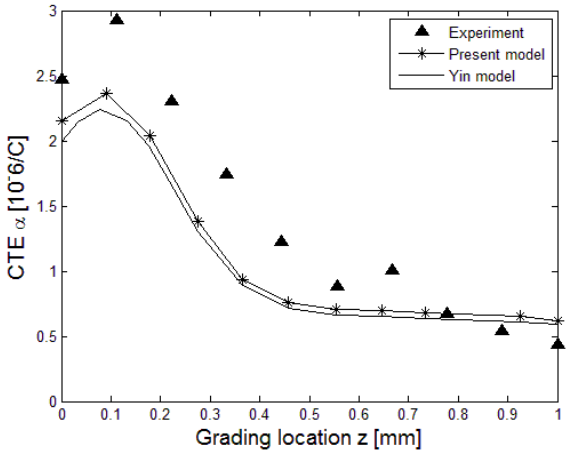

Figure 4.48. Comparisons of Mo/SiO_2 FGM effective CTE distribution between present model simulations, Yin model [99] and experimental data [98].

Further model validation of the offered model is illustrated by considering the effective CTE distribution measured by Neubrand et al. [100] for an Al/Al_2O_3 FGM with linear grading of Al whisker-shaped particles. The material properties used for the analysis are shown in Table 4-6. For the analysis, the experimental 35x33x3 mm plates with a 17.5 mm grading length were modeled as a 2x1 normalized plate with the same

characteristic disk radius and discretization schedule used in the previous example. The effective CTE predicted by the current model are found to be in good agreement with the experimental values and the analytical model of Yin et al. [99], as indicated by Fig. 4.48.

Table 4-6. Al and Al_2O_3 material properties.

Material	E (GPa)	ν	α (10^{-6}/K)
Al	69.0	0.33	23.1
Al_2O_3	390.0	0.20	7.7

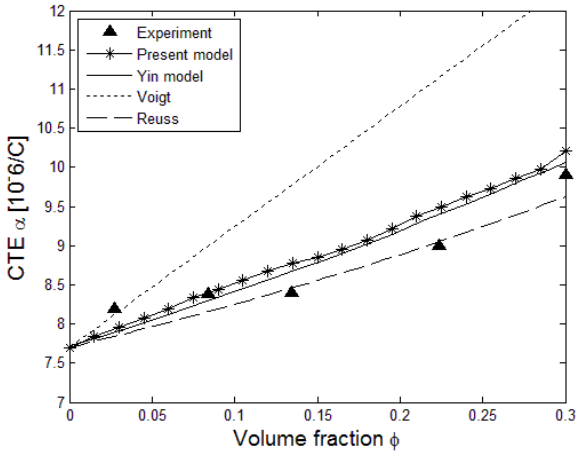

Figure 4.49. Comparisons of the Al/Al_2O_3 FGM effective CTE distribution between present model simulations, Yin model [99], Voigt and Reuss rule-of-mixtures and experimental data [100].

The predicted CTE values for uniform volume fraction composites have been validated by comparing to the experimental CTE data of the same the epoxy matrix composites discussed earlier in Section 4.6.1 and measured by Wong and Bollampally [96]. Once again the number of layers in the model is set to one, thus reducing the graded material model to a uniform composite. In this analysis, the model is assumed to be a 1x1 plate with periodic boundary conditions. Material properties used in the simulation are provided in Table 4-7. As Fig. 4.50 shows, the predicted values of the present model are

in good agreement with the experimental data and FGM model of Yin et al. [99] (only Silica-Epoxy composite data are available).

Table 4-7. Thermoelastic material properties of Expoy, Silica, SCAN and Alumina.

Material	E (GPa)	ν	α (10^{-6}/K)
Epoxy	2.25	0.19	88
Silica	73.0	0.19	0.5
SCAN	330.0	0.25	4.4
Alumina	385	0.24	6.6

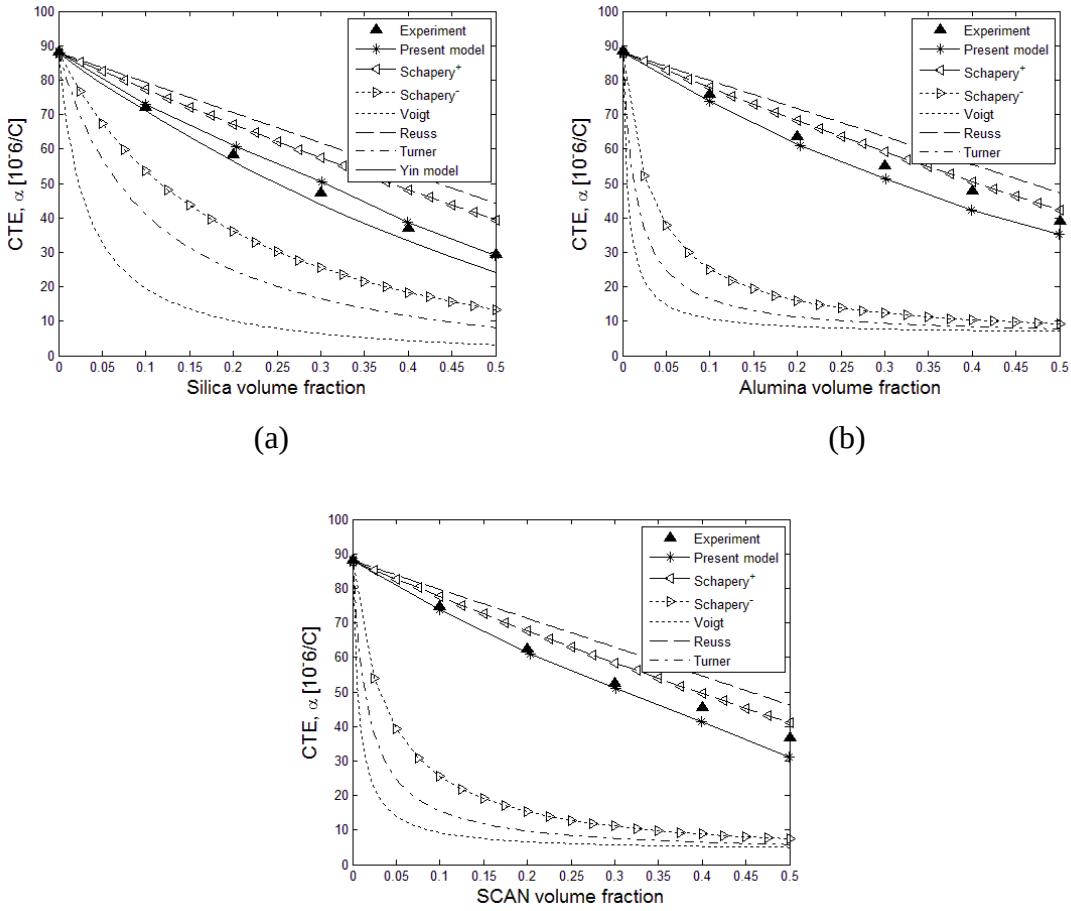

Figure 4.50. Comparisons of effective coefficient of thermal expansion (CTE) for epoxy matrix composites between present model simulations, bounds of Schapery [13], Voigt and Reuss rule-of-mixtures, Turner [10] model and experimental data [96] for (a) silica with Yin model [99] (b) alumina (c) SCAN reinforcement materials.

4.6.3 Thermal Conductivity Model Validation

The accuracy of the FGM model in predicting the effective spatially dependent thermal conductivity of graded composites is first evaluated by considering the experimental data of Khor and Gu [101]. In this study, the authors investigated the effective thermal conductivity of an FGM TBC comprised of yttria-stabilized zirconia (YSZ) and NiCoCrAlY comprised of five layers, as shown in Fig. 4.51.

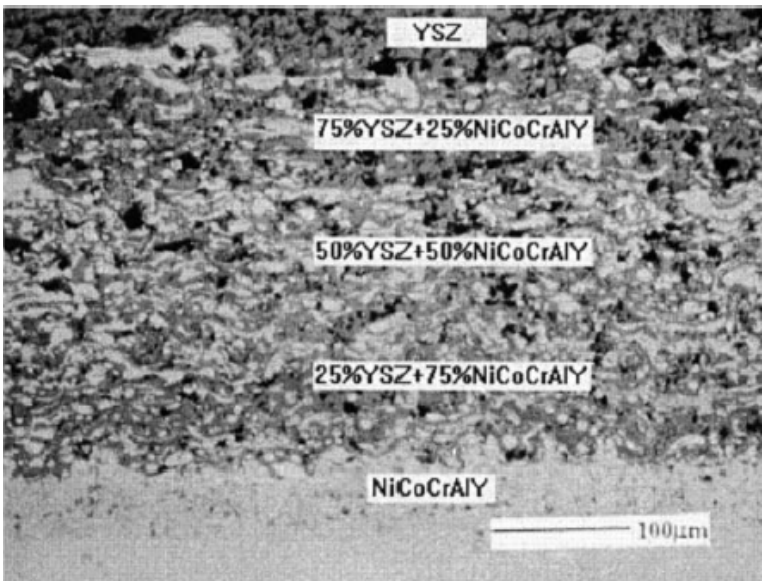

Figure 4.51. Microstructure of the five-layer YSZ/ NiCoCrAlY FGM coating [101].

The experimental 1.25 cm diameter and 1.5 mm thick samples are modeled as a 2 x 0.25 normalized plate with 21 layers and a disk radius of 0.003. Additionally, due to the recorded material porosity indicated by the authors, a third phase is introduced and modeled as air. Using the material properties provided in Table 4-8 and swapping the constituent phase materials at 80% YSZ content, as suggested by the high-percolation manufacturing, the results of the simulation are shown in Fig. 4.52.

Table 4-8. Thermal material properties of YSZ, NiCoCrAlY and Air.

Material	k (W/m-K)	C_p (kJ/kg-K)	ρ (kg/m^3)
YSZ	0.524	498.5	6050
NiCoCrAlY	4.303	545.0	8400
Air (20 °C)	0.026	1.01	1.225

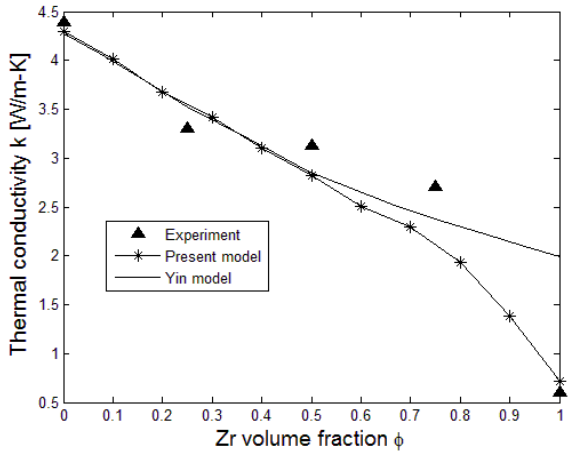

Figure 4.52. Comparisons of YSZ/ NiCoCrAlY FGM coating effective thermal conductivity predictions between present model simulations, Yin model [102] and experimental data [101].

As can be inferred from the above figure, the values predicted by the present model are in good agreement with the experimental results. Moreover, when compared to the analytical model of Yin et al. [102], the results could be interpreted as improved. This is due to the fact that the present model takes into account the effect of porosity on the effective thermal response. Meanwhile, the Yin model matches well for ZrO2 volume fractions less than 0.8 due to the assumption that the conductivity of ZrO2 is 2.0 W/m-K as opposed to the experimental value of 0.524 Wm-K, leading to an over prediction at higher ZrO_2 contents.

Additional conductivity validation is presented by considering the effective electrical transport process of an alumina/zirconia (Al_2O_3/ZrO_2) FGM as measured experimentally by Sanchez-Herencia et al. [103]. The electrical conductivity, which of course is mathematically analogous to the thermal conductivity further expands the model validation by including additional material properties of interest for spatially variant composites. In these eight layer slip cast composites, yttria-stabilized tetragonal zirconia serves as the base layer while increasing the Al_2O_3 content in subsequent layers to a fully saturated outer layer. The FEM used to simulate the eight-ply FGM was carried out assuming a 2x1 flat plate with a 0.005 particle radius. The manufactured materials are

noted as having a high percolation limit of approximately 80% Al_2O_3 content. To address this, a varying number of layers (greater than eight) is used to alter the volume fraction at which the phase materials are switched to study the effect of phase substitution. The electrical conductivity γ of the constituent phase materials used in the analysis is provided in Table 4-9. The effective electrical conductivity for various swapping fractions predicted by the present model is compared to the experimental data and analytical model of Yin et al. in Fig. 4.53, with varying swap fractions indicated as "Present model, v_s=XX", where XX is the swap percent used. As shown, the predicted values are in fair agreement with the experimental data. This is particularly true when the constituent phases are swapped at higher volume fractions (e.g., $v_s > 50\%$). At these swap fractions, the proposed FEM attempts to mimic the high percolation limit of the experimentally manufactured FGM with a Zr dominant matrix phase.

Table 4-9. Electrical conductivity of Zr and Al_2O_3.

Material	γ (S/cm)
Zr	1.35E-1
Al_2O_3	1.11E-8

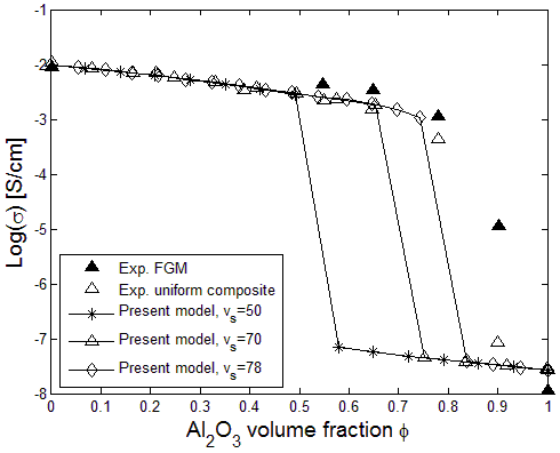

Figure 4.53. Comparison of effective electrical conductivity for an Zr/Al_2O_3 FGM between experimental data [103] and present model with varying swap volume fractions.

As a final conductivity model validation, we once again highlight the flexibility of the proposed model by considering the effective thermal conductivity of fixed volume fraction composites. The epoxy composite materials in this case are in the same experimental setup discussed previously by Wong and Bollampally [96]. The epoxy and filler material properties for the 1x1 RVEs with periodic boundary conditions are provided in Table 4-10.

Table 4-10. Thermal conductivity of Expoy, Silica, SCAN and Alumina.

Material	k (W/m-K)
Epoxy	0.20
Silica	1.5
SCAN	220.0
Alumina	36

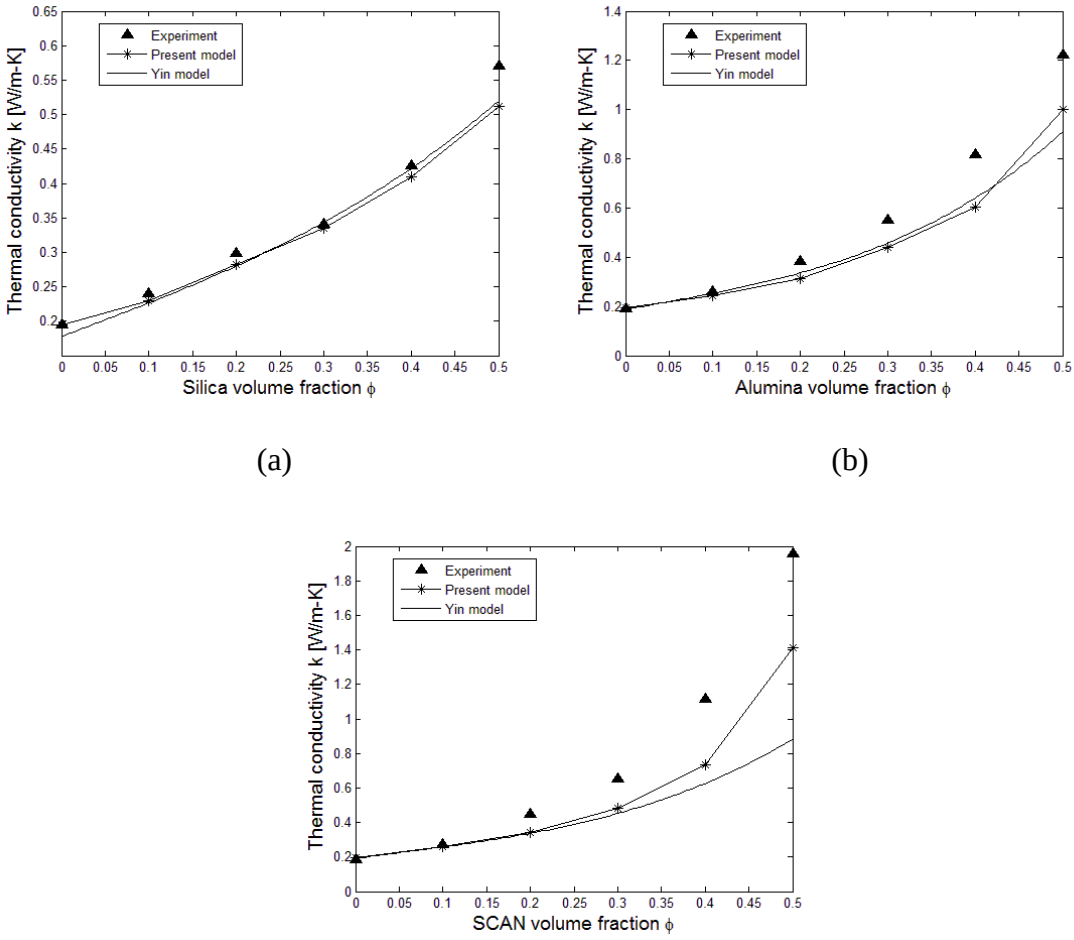

Figure 4.54. Comparisons of effective thermal conductivity for epoxy matrix composites between present model simulations, Yin model [102] and experimental data [96] for (a) silica (b) alumina (c) SCAN reinforcement materials.

Figure 4.54 displays the predicted effective thermal conductivity of the epoxy composites with Silica, SCAN and Alumina reinforcement materials. As shown, the predicted values are in good agreement with the experimental data and the analytical model of Yin et al. [102], further emphasizing the accuracy of the proposed model.

4.6.4 Specific Heat Model Validation

The final model validation involves comparing the predicted effective specific heat values with experimentally available data. While multiple experimental data sets have been used to validate the previous material properties, experimentally obtained data for the effective specific heat of FGMs is not as bountiful. The presented validation uses the previously mentioned experimental data for a YSZ/NiCoCrAlY FGM TBC provided by Khor and Gu [101]. Using model parameters identical to those of the thermal conductivity model with the material properties provided previously in Table 4-8, the model is found to compare well with the experimental data, as shown in Fig. 4.55.

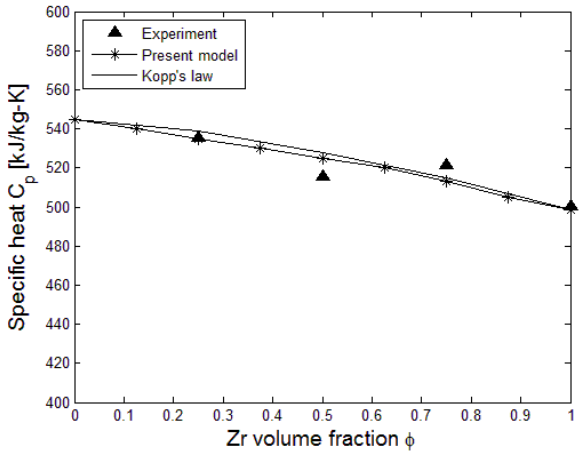

Figure 4.55. Comparison of effective specific heat for an YSZ/ NiCoCrAlY FGM coating between present model, Kopp's law [29] and experimental data [101].

4.7 Effect of Porosity Distribution in Graded Materials

While the primary focus of the previous work has been on determining the effective properties of FGMs, we now turn to study the effects of flaws and porosity on the resulting properties. Depending on the field of study, porosity can be seen as a nuisance that should be avoided at all costs or a well-received intentionally introduced feature. In the case of multifunctional structural/thermal management systems, the effects of porosity can be viewed as both beneficial and detrimental. For instance, consider

thermal protection materials such as silicon-based syntactic foams or the ceramic thermal tiles found on the NASA space shuttle. These tiles leverage the effects of porosity to control and enhance the materials' thermal properties [104]. On the other hand, the introduction of voids, defects or porosity can have drastic implications on the effective mechanical properties of structural materials [95, 105]. Thus, our interest for this section lies in understanding how defects introduced deliberately or unintentionally influence the estimation of the effective temperature-dependent thermoelastic and thermal properties of graded composite materials.

4.7.1 Modeling of Porous Graded Materials

To investigate the effects of porosity on the material response, we will consider a three-phase FGM with material variation in the through-thickness direction only. Each FGM is composed of Titanium (Ti), Zirconia (Zr) and varying degrees and distribution of porosity, modeled as voids with physical properties of air. It is worth noting that our analysis requires values for the Young's modulus and Poisson's ratio of the void material to avoid numerical singularities. Thus a small value is used for the elastic stiffness to avoid these numerical issues. The material properties at 500 °C used in the forthcoming analysis are provided in Table 4-11.

Table 4-11. Material properties of Ti [106], Zr [107] and air [108].

Material	E (GPa)	ν	α (10^{-6}/K)	k (W/m-K)	C_p (kJ/kg-K)	ρ (kg/m^3)
Ti	79	0.314	10.12	14.24	0.651	4357
Zr	89	0.333	6.29	1.94	0.598	3625
Voids	0.001	0	0	0.052	1.07	0.524

Similar to the 2D material variation functions, the distribution and magnitude of the porosity third-phase $\boldsymbol{v_v(z)}$ is controlled using the following power law

$$v_V(z) = \eta_z^v \frac{z^{n_z^v}}{h} \tag{4.7}$$

where η_z^v and n_z^v are parameters controlling the porosity phase maximum content and the distribution profile in the through-thickness direction z. The actual reinforcement and matrix volume fractions v_r^{act} and v_m^{act} , respectively, are calculated by

$$\begin{aligned} v_r^{act} &= v_r - v_v \\ v_m^{act} &= 1 - v_r - v_v \,. \end{aligned} \tag{4.8}$$

In the current analysis, four different porosity profiles, denoted as "Profile-1 … Profile-4", are investigated using a 1D linear ($n_z = 1,\ \eta_z = 1$) variation of Zr. For this study, the first two profiles exhibit a linear porosity variation ($n_v = 1$) with maximum content $\eta_v = 0.1$ and $\eta_v = 0.7$. The remaining two profiles use a constant porosity content of $\eta_v = 0.4$ and distribution profile parameters of $n_v = 2$ and $n_v = 6$. The resulting porosity distributions are plotted against the relative reinforcement volume fraction, as shown in Fig. 4.56.

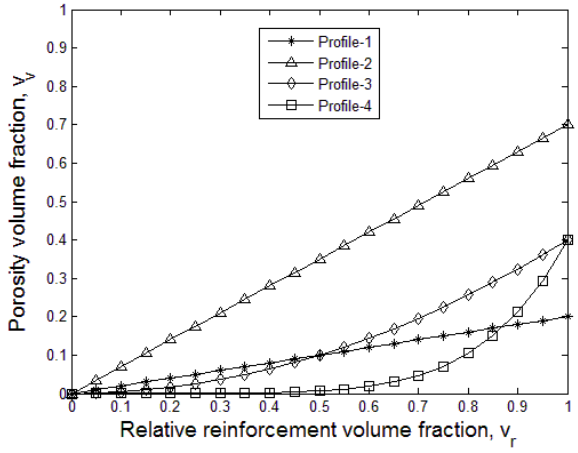

Figure 4.56. Porosity distribution profiles vs. relative reinforcement volume fraction.

4.7.2 Effective Properties of Porous Graded Materials

Utilizing the modeling technique described in Section 4.3.1, the effective elastic, thermoelastic and steady-state and transient thermal responses are determined by dividing a 2x1 mm plate into 21 layers. A characteristic particle radius of 0.005 mm (5 μm) is used to pack the geometry, with phase swapping occurring at 0.68 (particle + void fraction). The resulting predicted effective Young's modulus for each porosity profile compared to the variational three-phase bounds of Hashin and Shtrikman [6] denoted by the upper (HS^+) and lower (HS^-) and the self-consistent scheme (SCM) approximation [8] are provided in Fig. 4.57. Figure 4.58 compares the resulting effective Young's moduli for each of the porosity profiles.

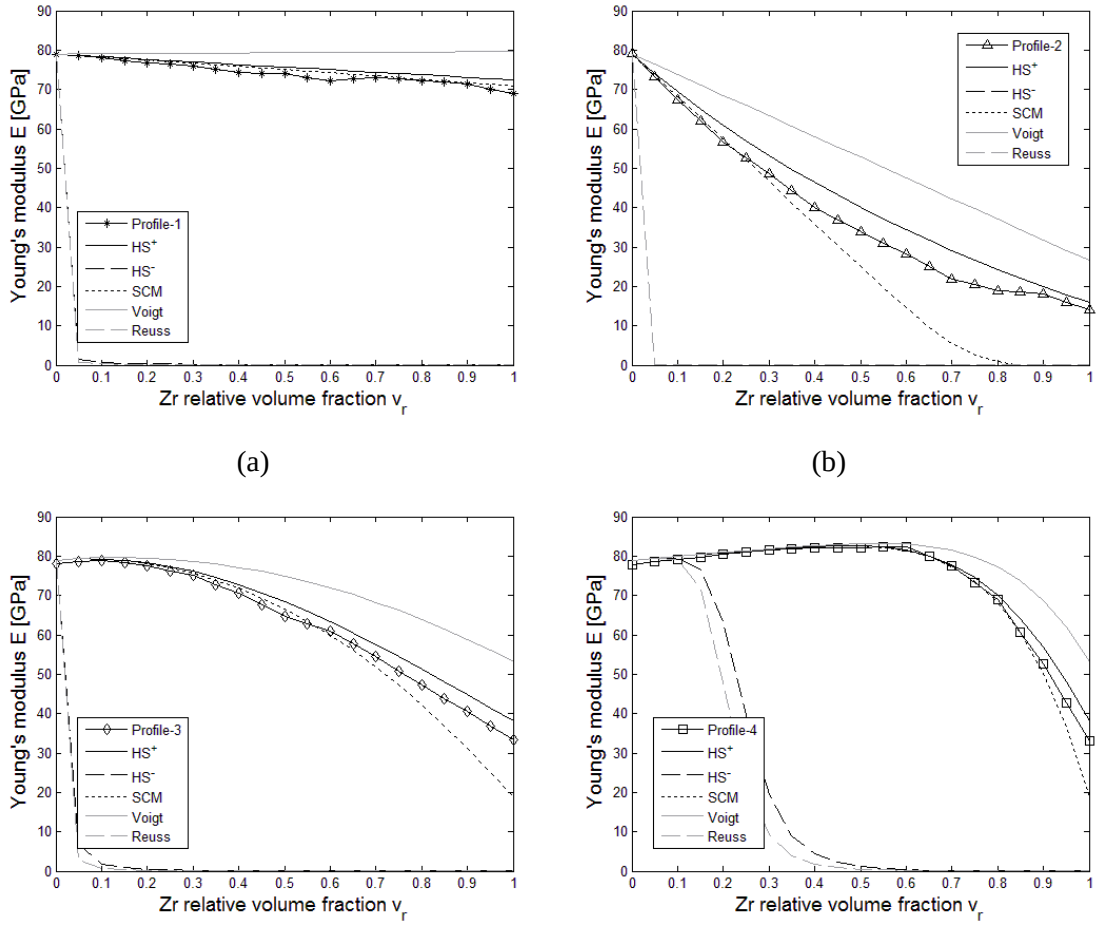

Figure 4.57. Effective FGM Young's modulus for porosity distribution (a) Profile-1, (b) Profile-2, (c) Profile-3 and (d) Profile-4.

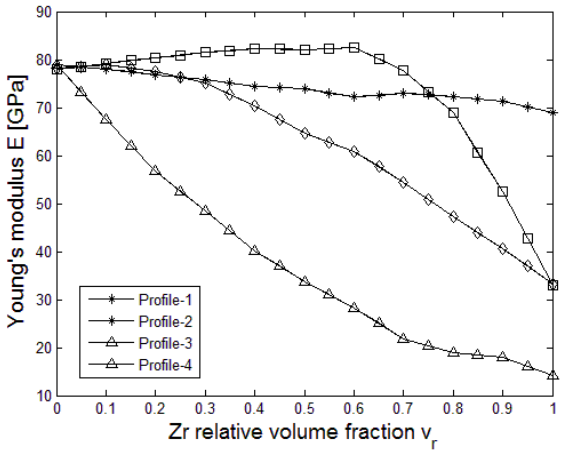

Figure 4.58. Effective FGM Young's modulus for all porosity distribution profiles.

Referring to Figs. 4.57 and 4.58, it can be seen that the effective Young's modulus exhibits a strong dependence on the spatial distribution of porosity within the material. Moreover, drastic or aggressive magnitudes of porosity coupled with moderate changes in distribution result in a fast reduction of the effective elastic property (Profile-2). Meanwhile, profiles with lower magnitudes (Profile-1) and slower variations in the porosity volume fraction (Profile-3 and 4) are able to sustain higher elastic properties throughout the grading direction. The steady-state thermal response has been calculated for each porosity profile to understand the effect of voids on the effective material response. This is done by applying a known temperature gradient across the top and bottom boundaries in the grading direction and volume averaging the heat flux and temperature gradient of each section as described in detail in Section 2.6.6. The resulting effective thermal conductivity distributions are provided in Fig. 4.59 plotted against the rigorous H-S three-phase bounds (HS^+ and HS^-) [20], the SCM approximation [19] and the Wiener ROM bounds [16]. Figure 4.60 compares the effective thermal conductivity for each porosity variation with respect to the relative Zr volume fraction. Examining each of these figures, similar conclusions can be drawn as those made for the effective

elastic response. Moreover, as one would expect, greater reductions in the effective thermal conductivity are found for distributions where porosity is prevalent.

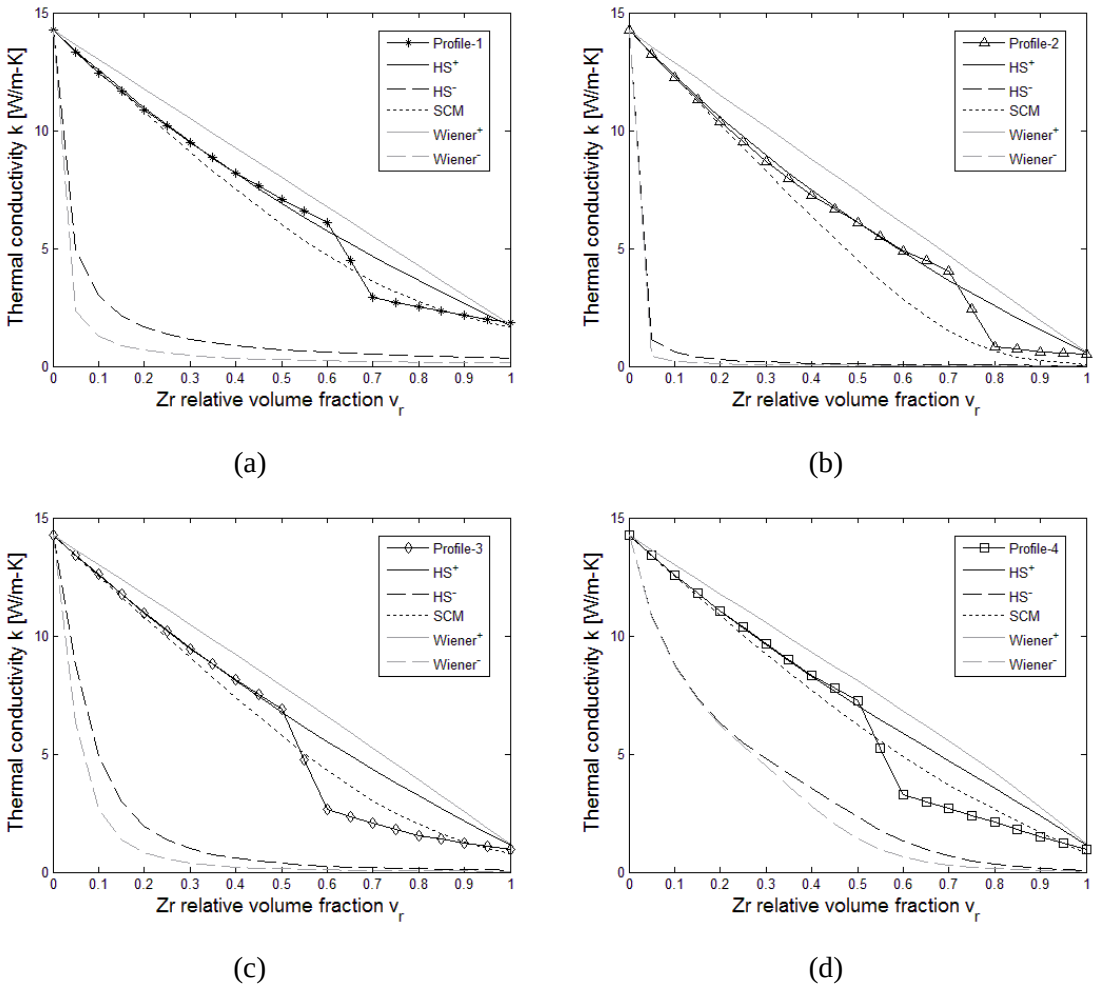

Figure 4.59. Effective FGM thermal conductivity for porosity distribution (a) Profile-1, (b) Profile-2, (c) Profile-3 and (d) Profile-4.

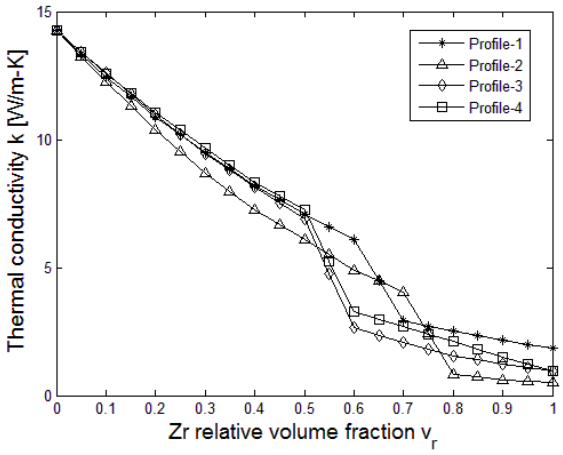

Figure 4.60. Effective FGM thermal conductivity for all porosity distribution profiles.

We also consider the effects of porosity on the FGM thermoelastic response by estimating the CTE with respect to location. The effective CTE α^* is estimated by applying a uniform temperature and volume averaging the thermal and mechanical strain. While structural loads are not applied to the body, mechanical strains are generated as a result of the mismatch in the CTE for each of the material phases. Homogenizing the thermoelastic response according to Section 2.6.7, the expansion results are compared to the bounds of Schapery [13] in Fig. 4.61, while Fig. 4.62 provides comparisons of each material distribution.

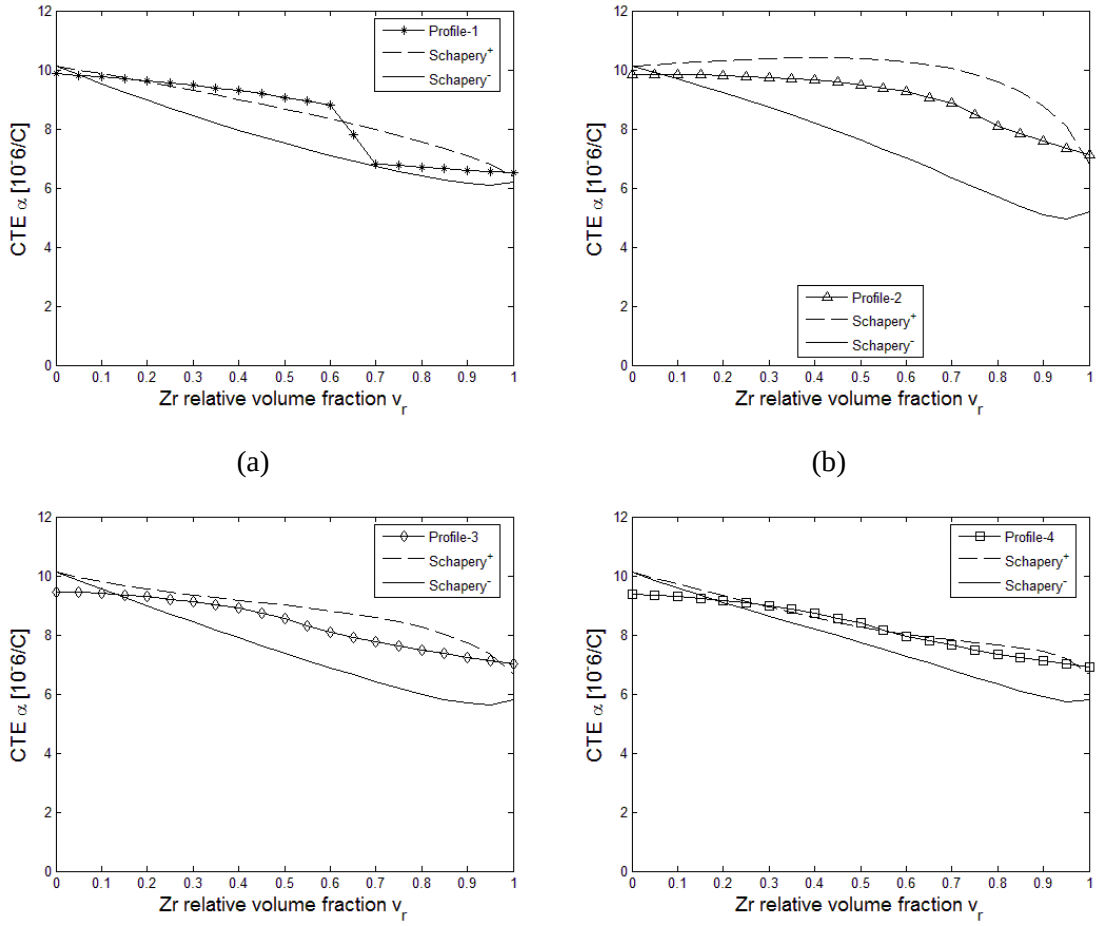

Figure 4.61. Effective FGM coefficient of thermal expansion for porosity distribution (a) Profile-1, (b) Profile-2, (c) Profile-3 and (d) Profile-4.

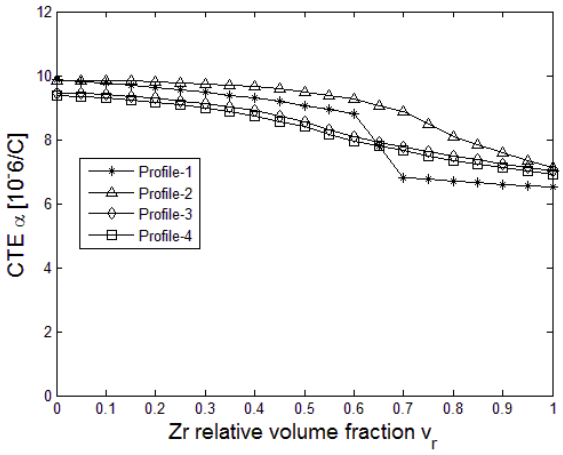

Figure 4.62. Effective FGM coefficient of thermal expansion for all porosity distribution profiles.

As can be seen in the above figures, the effective thermal expansion exhibits a slight dependence on the spatial distribution of porosity within the material. Furthermore, moderate variations in porosity distribution (Profile-3 and Profile-4) results in a faster reduction of the effective thermoelastic property. Meanwhile, profiles with lower levels of porosity (Profile-1) result in little change in reported CTE values when compared to those of a two-phase Ti/Zr system.

Lastly, we investigate the effects of porosity on the FGM transient thermal response using the proposed model to estimate the spatial dependence of the effective specific heat. The effective specific heat C_p^* is evaluated by subjecting the material to a uniform heat source to the body $\bar{Q}$ and assuming a transient condition outlined in Section 2.6.8. The effective specific heat was found to exhibit strong dependence on the porosity profile and the amplitude of the void content present in the grading direction. Figure 4.63 depicts this dependence and was found to be in good agreement with the Koop's mixture law. Moreover, as expected, low-volume fraction porosity profiles (Profile-1) deviate little from a virgin two-phase material. Meanwhile, profiles with higher void content (Profile-2, Profile-3 and Profile-5) approach C_p values to that of air, with Profile-2 being the closest. Figure 4.64 provides a comparison of the effective specific heat for each

porosity profile, further demonstrating the dependence on the quantity and distribution of porosity in the system.

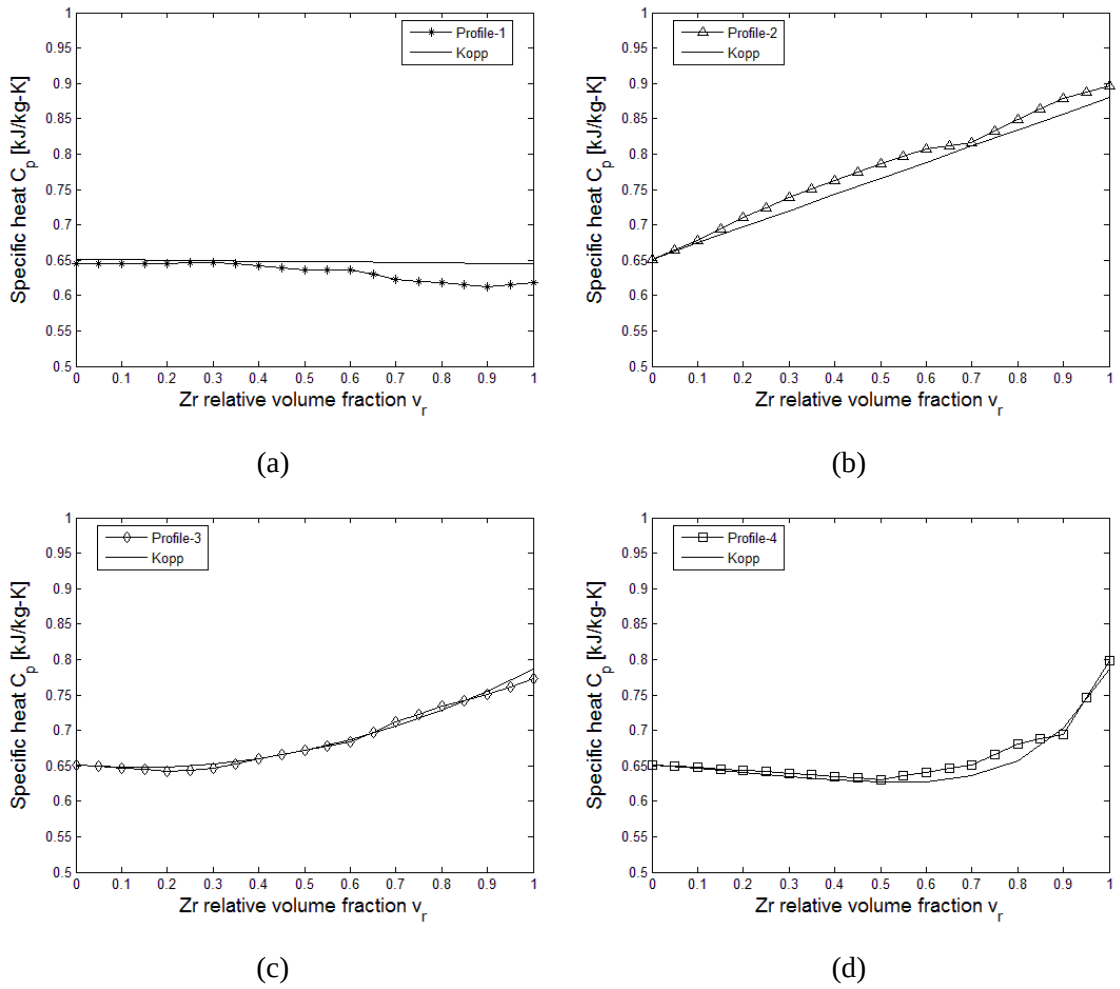

Figure 4.63. Effective FGM specific heat for porosity distribution (a) Profile-1, (b) Profile-2, (c) Profile-3 and (d) Profile-4.

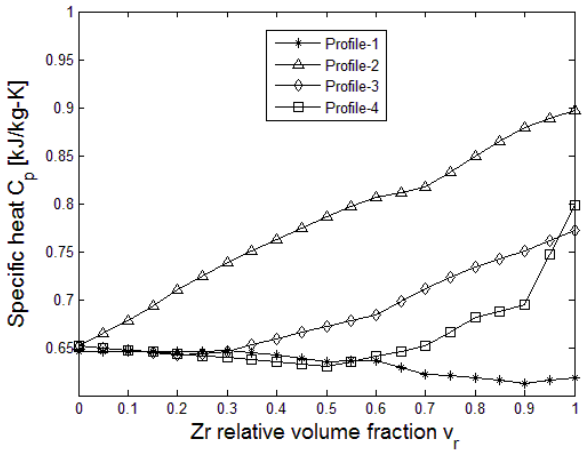

Figure 4.64. Effective FGM specific heat for all porosity distribution profiles.

4.7.3 Application of Porous Graded Materials

Utilizing the effective material properties obtained in the previous exercise, the thermostructural effects of the porosity model are studied. In this analysis we consider the transient thermal and thermoelastic response of a two-dimensional flat plate subjected to a surface heat flux q on the upper boundary as depicted in Fig. 4.65. Here, the upper surface (gray) represents a TPS or TBC material of thickness $t_1 = 0.25\ mm$ which is intended to remove or mitigate the effects of temperature on the underlying structural material (black surface).

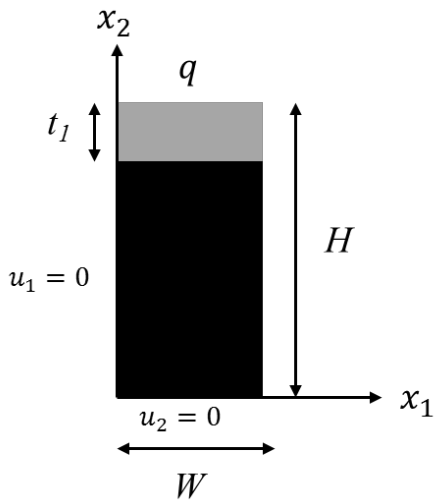

Figure 4.65. Effective FGM specific heat for all porosity distribution profiles.

As a benchmark, we consider a plate comprised of a Titanium alloy Ti-6Al-4V and Acusil® II syntactic foam, which serve as structural and TPS materials, respectively. The material properties of the Ti-6Al-4V and Acusil® II at 500 °C, referred to as Ti and TPS hence forth, used in the study are provided in Table 4-12. The baseline thermostructural response is compared to the same porous Ti/Zr FGMs with varying magnitudes and distributions of porosity as described in the previous section, with material variation for all FGMs acting in the through-thickness direction (top-bottom). For these computations, we assume temperature-independent material properties, a strain-free state at an initial temperature of 500 K and a plate with width w and height h of 0.5 and 1 mm, respectively. Applying a heat flux of 200 W/m^2, the resulting temperature distribution for each case after 180 seconds is provided in Fig. 4.66 below.

Table 4-12. Properties of Ti-6Al-4V [24], Zr [25] and Acusil® II [32] at 500 °C.

Material	E (GPa)	ν	α (10^{-6}/K)	k (W/m-K)	C_p (kJ/kg-K)	ρ (kg/m^3)
Ti	79	0.314	10.12	14.24	0.651	4357
TPS	0.28	0.32	20.9	0.19	962	0.524

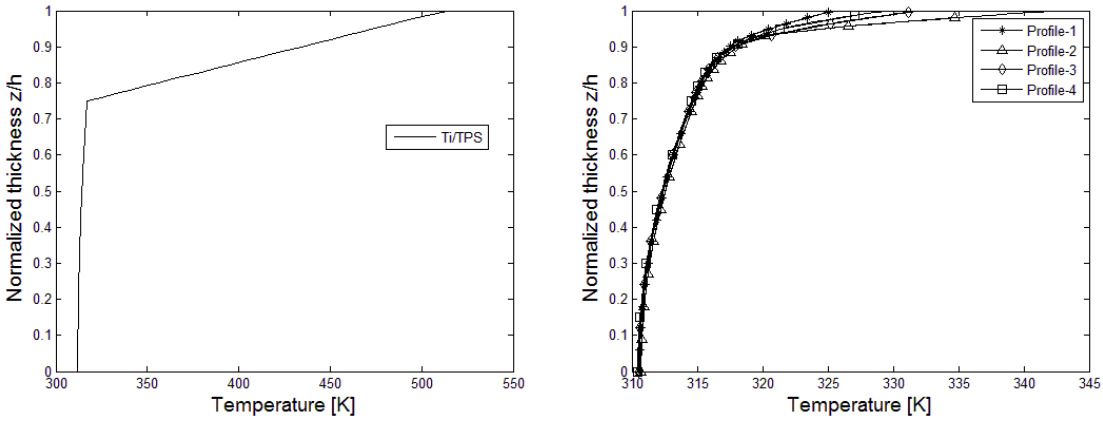

(a) (b)

Figure 4.66. Resulting temperature vs. normalized thickness after 180 seconds (a) Ti/TPS material system, (b) Porous FGM profiles.

Referring to Fig. 4.66, the normalized thickness spans the x_2 direction of the plate with 1 representing the top surface. It can be seen that the Ti/TPS system creates an abrupt change in temperature corresponding to the union of the underlying Ti and TPS material interface. Meanwhile, implementation of the porous FGM results in a drastic reduction of the through-thickness temperature gradient with minimal increase in temperature of the underlying material. The resulting thermostructural responses of each of these temperature distributions are provided in Fig. 4.67.

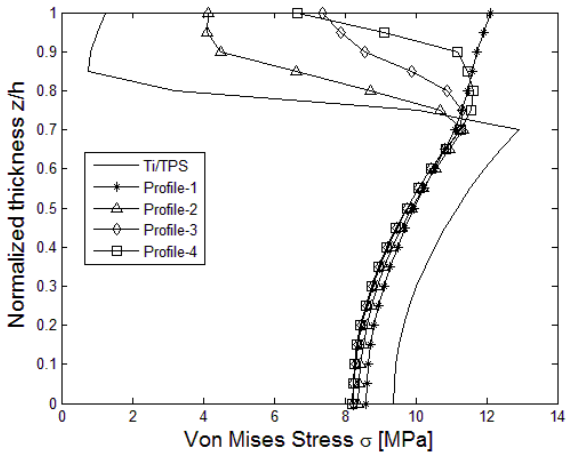

Figure 4.67. Effective thermoelastic response vs. normalized thickness after 180 seconds for Ti/TPS and porous FGM distribution profiles.

As can be inferred from the figure above, introducing the graded microstructure results in reduced stress concentrations when compared to the interface of the Ti/TPS system ($z/h = 0.7$). This is a direct result of two key coupled features of graded structures. First, a reduction of the through-thickness temperature gradient creates a uniform temperature field, thus creating a uniform thermal expansion throughout the body and therefore reducing stress concentrations. This is a direct result of reducing the differences in thermal conductivity and specific heat seen between base and typical TPS materials. Second, introduction of smoothly varying material properties reduce the elastic, thermoelastic and thermal mismatch, which is very pronounced in the Ti/TPS system.

Moreover, from Figs. 4.66 and 4.67, we can see that Profile-1 of the porosity distributions creates the most uniform stress distribution when compared to the remaining distributions at a minimal cost of increase in underlying material temperature. Thus the ideal material distribution would be a function of the maximum allowable top and bottom surface temperatures, stress, deflection, etc.

CHAPTER 5

THERMOSTRUCTURAL ANALYSIS OF FUNCTIONALLY GRADED HYPERSONIC PANELS

In this chapter, application of the titanium/ titanium diboride metal-ceramic FGMs for hypersonic STATS is studied. It has been suggested that STATS may offer the advantage of reducing or eliminating many of the downfalls of conventional structural and thermal airframe materials, such as stress concentrations and temperature gradients, by incorporating spatial material grading into the structures [2, 109, 110]. Additionally, incorporating graded materials as multifunctional thermostructures can eliminate design constraints such as maximum bond line temperature (the interface between the TPS and skin) and thermally induce oxide growth of the skin material, both of which can be limiting factors in hypersonic airframe design using conventional approaches.

5.1 Representative Hypersonic Airframe

In this work, a representative hypersonic monocoque airframe is considered using the geometry and coordinate system convention shown in Fig. 5.1. In this convention, the x-axis spans the longitudinal axis, while the clocking angle Φ defines the geometry in the circumferential direction. A characteristic flight trajectory for the airframe is provided in Fig. 5.2.

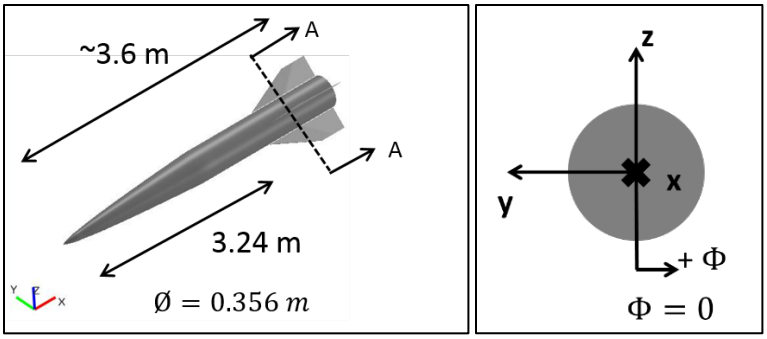

(a) (b)

Figure 5.1. (a) Representative geometry and (b) coordinate system convention.

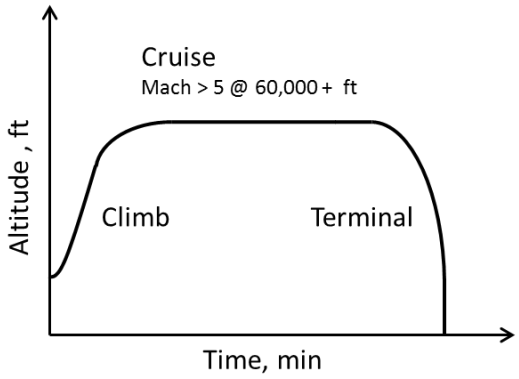

Figure 5.2. Example flight trajectory.

In the initial phase (climb), the missile is released from an elevated altitude from a sub to transonic speed (Mach 0.8-1.2) and accelerated to Mach 3 while performing a steep climb to above 60,000 ft. The second phase (cruise) is a hypersonic (Mach $\geq$ 5) cruise up to 10 minutes in duration. The final phase of the trajectory (terminal) is a steep non-powered dive to the final destination. During the terminal phase, the vehicle may undergo erratic changes in trajectory, resulting in acceleration loads above 10 *g*'s.

As discussed previously in great detail, the consequences of highly maneuverable airframes operating at high velocity are high structural loads due to maneuvering at high dynamic pressures and extreme temperatures as a result of aerodynamic heating. A design envelope for the expected skin temperatures is estimated to be in the range of 530-

1100 °C (1000-2000 °F) using the anticipated cruise speed (Mach 8) and altitude along with Fig. 5.3 (a). Similarly, the expected dynamic pressure acting on the vehicle, assuming a range of 200 to 300 nautical miles, is expected to be between 100-150 kPa (see Fig. 5.3 (b)).

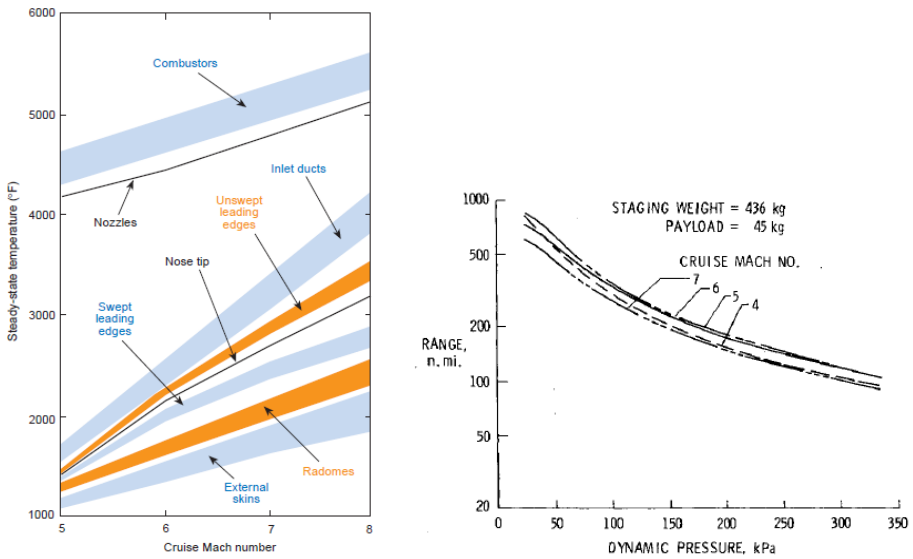

(a) (b)

Figure 5.3. (a) Steady-state temperature vs. Mach number at 80,000-ft [111] (b) Cruise range variation with dynamic pressure [112].

The size of this titanium (Ti-6Al-4V) skin and Exelis Acusil® II TPS airframe has been determined to be suitable by the Air Force Research Laboratory (AFRL) Munitions Directorate using the in-house flight simulation analysis tool, Aerothermal Analysis Targets Program (ATAP). This analysis was also used to provide the time- and spatial-dependent thermal and structural loads acting on the airframe. To focus the extent of this study, Section A-A of the airframe shown in Fig. 5.1 (a) will be used for benchmarking and future investigation. This 200 mm long section (disregarding the fins) is chosen because the titanium skin and Acusil® II TPS thickness are constant at 1.3 and 2.05 mm, respectively. The total effective mass of the section is 1.40 kg. Moreover, the variation in

the thermal load and dynamic pressure along the longitudinal axis is negligible, resulting in loads as a function of time and clocking angle, Φ. The time- and spatial-dependent recovery temperatures, skin coefficients, pressure, bending moments and force components acting on this section at various clocking angles are provided in Figs. 5.4-5.6. As mentioned previously, time- and spatial-dependent thermal and mechanical loads on the section are a result of aerodynamic heating, high G maneuvers and dynamic pressure. In the data provided, moments about the remaining axis are assumed to be negligible (four orders of magnitude lower). Therefore, in Fig. 5.5 (b), only moments about the y-axis are presented and used in the upcoming analysis. Temperature-dependent material properties for the skin and TPS materials are provided in Table 5-1, while complete variation of the Ti alloy skin have been provided previously in Figs. 4.7-4.9.

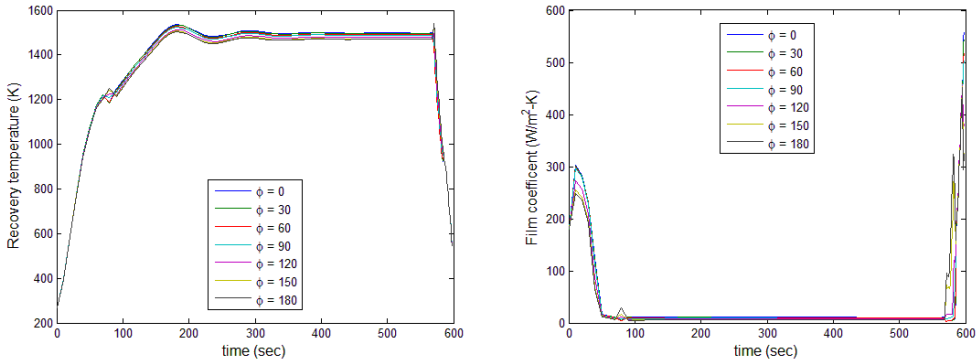

(a) (b)

Figure 5.4. Time- and spatial-dependent (a) recovery temperature (b) skin coefficient.

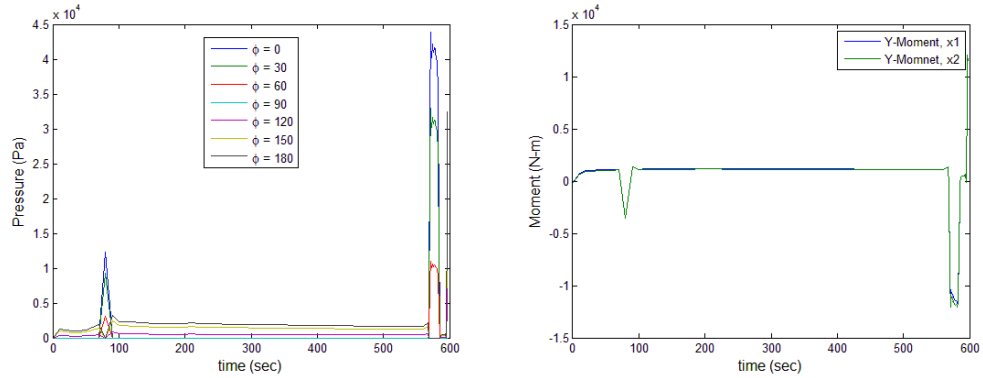

(a) (b)

Figure 5.5. Time- and spatial-dependent (a) pressure and (b) bending moments at front x_1 and rear x_2 of section.

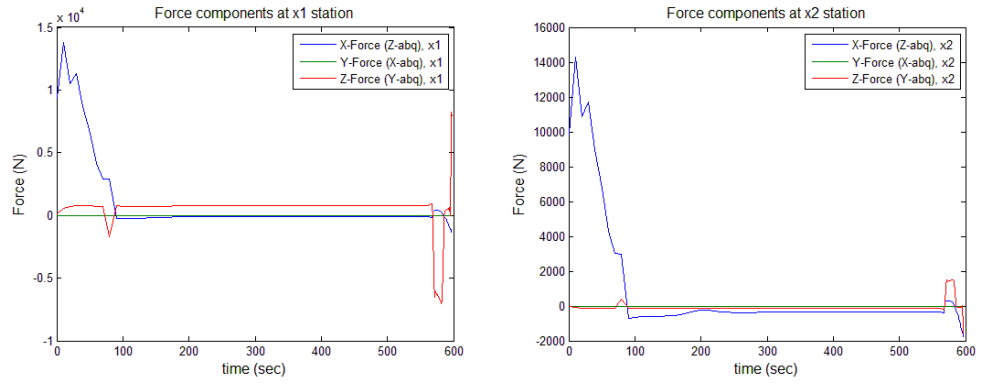

(a) (b)

Figure 5.6. Time- and spatial-dependent force components (a) front x_1 and (b) rear x_2 of section.

Table 5-1. Material property variation of Ti-6l-4V [89] and Acusil® II [113] at 20/600 °C.

Material	E (GPa)	ν	α (10^{-6}/K)	k (W/m-K)	C_p (kJ/kg-K)
Ti-6Al-4V	106/73	0.298/0.317	8.8/10.2	6.1/16	535.3/670
Acusil ® ii	0.28	0.320	20.9	0.05/0.19	962

Modeling of the time- and spatial-dependent loading was accomplished using a two-step sequential temperature-dependent FEM in Abaqus/CAE. The time-dependent thermal solution was first established, and the results were used as prescribed conditions for the time-dependent mechanical analysis. A sequential analysis was preferred as the coupled thermal-stress analysis option in Abaqus does not permit the use of inertia relief to be enforced (details later). Utilizing symmetry about the longitudinal axis (geometric and loading), the geometry was meshed using 2D composite layup shell elements with three integration points through the thickness of each layer. The recovery temperatures, T_r, and skin coefficients, h, provided by ATAP were used to calculate the applied heat flux, Q, to the vehicle surface using the following relation:

$$Q = h(T_r - T_w) + \epsilon\sigma(T_\infty^4 - T_w^4), \tag{5.1}$$

where T_w and T_∞ are the outside wall and ambient temperature, respectively; ϵ is the emissivity; and σ is the Stephan-Boltzmann constant. In Eq. (5.1), the ambient air temperature is assumed to be constant and is determined using the U.S. Standard Atmosphere, 1976 [114] table at 60,000 ft, resulting in an ambient temperature of 216.65 K. The inside wall of the structure is assumed to be adiabatic, hence heat transfer to the inside of the missile atmosphere is not permitted.

Temporal- and spatial-dependent loads are applied to the structural panels using the Abaqus user-defined FORTRAN subroutines DFLUX and DLOAD [115] for heat flux and pressure applications, respectively. Because automatic time stepping is utilized,

Abaqus determines the appropriate time increment based on the convergence of the previous iteration. In this case, the current time step may not coincide with the time resolution of the provided data. Moreover, the finite element discretization may not coincide with the spatial resolution of the provided data. To overcome these obstacles, an additional FORTRAN function was written within DFLUX and DLOAD to linearly interpolate the time and space variables (*y* and *z* positions) to determine the appropriate load. Section force components (axial and shearing) and bending moments are applied to reference points at the front and rear of the section and coupled to the section edges using coupling constraints and time interpolated using the same method as discussed above in a similar interpolative manner. Symmetric boundary conditions are used along the longitudinal axis of the section and on the leading edge, while the trailing edge was left unconstrained. As a result of the structure being in motion at each time step, the applied loads do not necessarily imply that the structure is in equilibrium. Such an analysis results in unconstrained DOFs typically requiring the use of a time-consuming dynamic analysis. However, in aero-structural analysis, the inertia relief solution technique is commonly used for such flight dynamics. Here, the acceleration forces from the dynamic system are applied as body forces to the model's center of mass to constrain the model's rigid body motion. This technique offers the benefit of reducing the computation time by allowing the system to be solved by inversion of the stiffness matrix in the typical fashion. Resulting thermomechanical response is then post-processed using the Abaqus/Python scripting interface to automate the tedious task of determining the stress, strain and temperature fields. Because coupling constraints are used to apply the aeroelastic loads to the section, post-processing the thermomechanical response is only considered in areas far away from the shell edges. This is done to eliminate spurious stress and strain values as it is well known that coupling constraints inherently tend to stiffen the nodes and elements in and near the vicinity of the constraint.

5.2 Thermostructural Analysis: Longitudinal Uniform Heat Flux

This section provides a detailed analysis of the thermostructural response of a skin/TPS (Ti-6Al-4V/Acusil® II) material system and Ti/TiB_2 1D FGM subjected to a heat flux that is uniform along the longitudinal axis. However, due to changes in the angle of attack during the flight, variation in surface heat flux can be found along the circumferential direction of the airframe direction (clocking angle). As can be observed in Table 5-1, Acusil® II has very low thermal conductivity, as would be expected from a TPS material. However, based on its relatively low stiffness, it does not provide structural value to the airframe. The motivation for this work is to establish an effective structural response to the thermal and structural loads imposed on the section.

To determine the effectiveness of replacing a conventional Ti/TPS with an FGM-based system, a computational study was carried out to complement the benchmarking of the Ti/TPS structural panel by replacing the skin and TPS with an FGM structural/thermal panel graded in the thickness direction only. The FGM in this study is comprised of a two-phase, titanium (Ti-6Al-4V) and titanium di-boride (TiB_2) composite. Titanium was chosen due to its high strength and temperature tolerance, and titanium di-boride for its increased stiffness and temperature stability of mechanical and thermal properties. Temperature-dependent material properties of the constituents were provided previously in Section 4.4 via Table 4-1 and Figs. 4.7-4.9. As can be seen in the Tables, TiB_2 may not appear to be an intuitive choice of material for thermal protection due to its relativity high thermal properties in relation to Ti-6l-4V. However, it has been shown that the high stiffness, low thermal expansion and temperature stability of TiB_2 make it a promising choice for an FGM TPS. Ceramic grading was determined based on the power law distribution of Eq. (3.1). For this initial investigation, one configuration was chosen using a maximum ceramic content of 85% (η=0.85) and quadratic grading profile (n=2) with the distribution provided in Fig. 5.7. A total thickness of 1.25 *mm* was chosen, resulting in a FGM section with a mass of 1.24 *kg*.

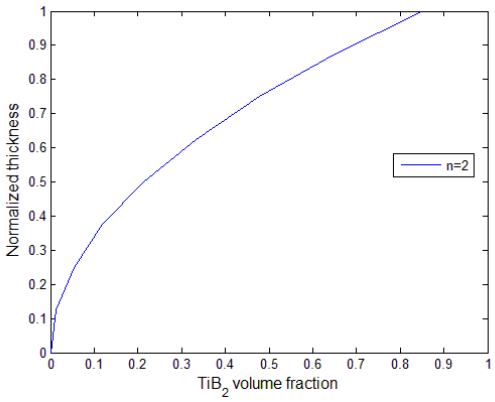

Figure 5.7. Ceramic volume fraction distribution, Ti/TiB_2.

5.2.1 Thermal response

Using the thermal loading data and modeling approach presented in Section 5.1, the thermal response of the Ti/TPS and Ti/TiB_2 1D FGM material systems are evaluated. As previously mentioned, the thermal load is a function of time and clocking angle of the section. A snap-shot of the spatially varying heat flux applied to the section of interest can be seen at a time step during the climb phase of the trajectory in Fig. 5.8.

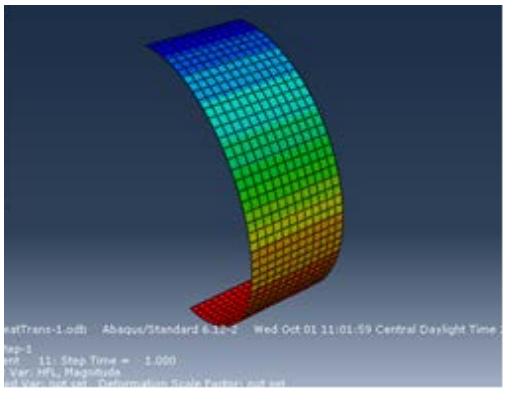

Figure 5.8. Spatially varying heat flux.

As can be seen in in Fig. 5.8, during the climb phase of the trajectory, the heat flux on the bottom surface is higher than that of the top surface due to the aerodynamic drag. The

time history of the outside and inside wall temperatures, in Kelvin, can be seen in Figs. 5.9 and 5.10.

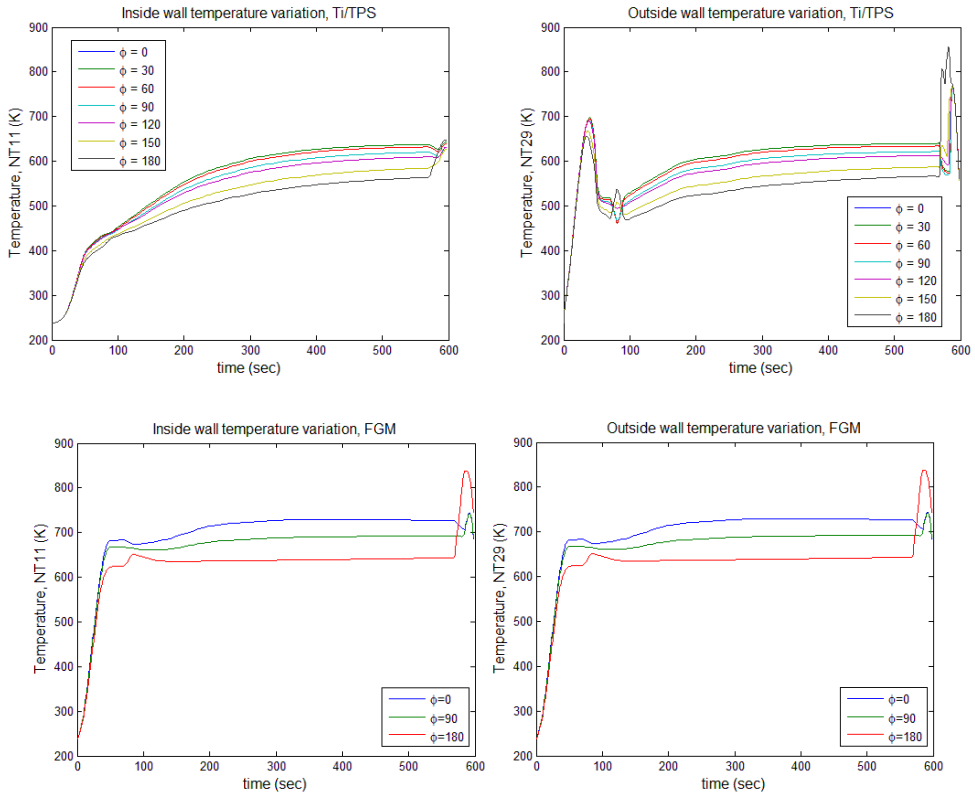

Figure 5.9. Inside (left) and outside (right) wall temperatures for Ti/TPS (top) and Ti/TiB_2 1D FGM (bottom).

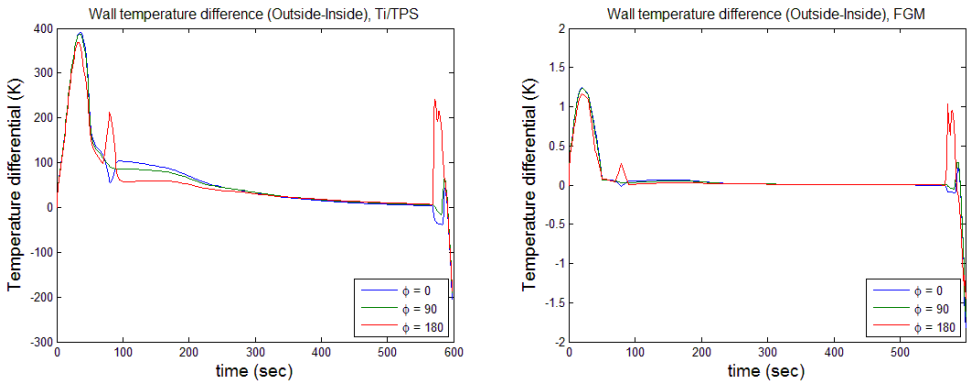

(a) (b)

Figure 5.10. Outside and inside wall temperature difference (a) Ti/TPS (b) Ti/TiB_2 1D FGM.

As can be deduced from the above inside and outside wall temperatures, a thermal gradient of as much as 400 K exists in the Ti/TPS structure, coinciding with major adjustments during the trajectory (climb and terminal phases), while the Ti/TiB_2 gradient is negligible. The temperature gradient at select times during the trajectory on the bottom of the Ti/TPS section (Φ=0) is provided in Fig. 5.11.

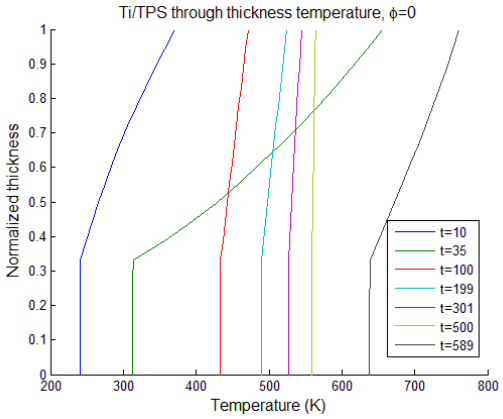

Figure 5.11. Ti/TPS through-thickness temperature gradients at clocking angle **Φ**=0 degrees.

Referring to Fig. 5.11, the through-thickness temperature gradient is predominant during major adjustments in the vehicle trajectory. At the beginning phase (*t*=10 and *t*=35 seconds), the airframe is performing an aggressive climb, resulting in increased surface heat flux as a result of aerodynamic heating. Here, the TPS does not allow the heat to flow through to the underlying Ti-6Al-4V skin, resulting in large temperature gradients. In the cruise portion of the flight (*t*=100 to *t*=500 seconds), the airframe becomes heat soaked as a result of sustained high-velocity flight. Finally, during the terminal phase (*t*=589 seconds), the surface temperature once again begins to increase and resist flow to the inner surface. As a result of incorporating the Ti/TiB_2 1D FGM, the temperature gradients throughout the section have been almost entirely eliminated, as can be seen when comparing the inside and outside wall temperatures in Fig. 5.9, or more clearly the outside to inside wall temperature difference in Fig. 5.10.

5.2.2 Thermostructural Response

Using the structural loading data and modeling approach presented in Section 5.1, the thermal response of the Ti/TPS material system is evaluated. In this procedure, the time-dependent section temperature is imposed as prescribed temperature conditions to determine the current value of the temperature-dependent material parameters during the analysis. As a result of the temperature gradients present in the section and the mismatch of the thermal expansion and stiffness of the materials, stress gradients and stress concentrations are generated in the through-thickness and in-plane directions of the section. The stress gradients and concentrations at t=572 seconds of the analysis are shown in Fig. 5.12, where stress is plotted vs. the normalized thickness at 0, 90 and 180 degree clocking angles (bottom, middle and top), with unity representing the top layer of the layup (outside wall).

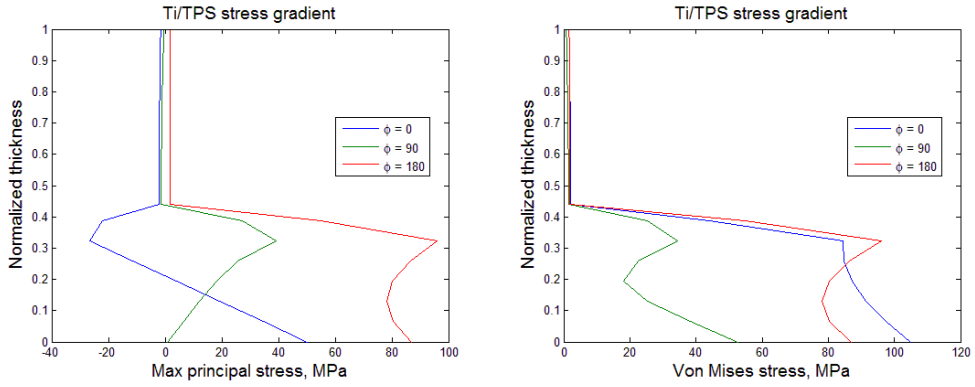

(a) (b)

Figure 5.12. Ti/TPS stress gradient (a) maximum principal (b) Von Mises.

As one can see, abrupt changes in stress occur at the interface of the Ti and TPS materials, as one would expect. Upon analyzing the entire time history, it was found that the time range 560-598 seconds appeared to generate the highest combined thermal and mechanical loads on the structure. Examining the results in this time range, the maximum outboard deflection was found to be approximately 9.4 mm in the middle of the section (Φ=90°).

The combined thermo-mechanical response of the Ti/TiB_2 1D FGM panel was found to be the most severe around the same time as the analysis of the Ti/TPS system. As a result of reducing the through-thickness temperature gradients and the amount of contrast in the stiffness and thermal expansion, a reduction in the through-thickness stress concentration in this time range was observed. As indicated by Fig. 5.13, the stress contours have reduced the concentrations along the thickness. This is particularly highlighted when examining the maximum principal stress of Fig. 5.13 (a). In addition to a uniform temperature and a reduction in stress gradients, the maximum outboard deflection and overall panel weight has been reduced as indicated by Table 5-2. It is worth noting that the results in the meantime must not be taken as absolute certainty. In the thermostructural analysis, it has been assumed that the maximum stress must not exceed that of either of the constituents' yield or ultimate strength. In this case, a maximum principal stress of approximately 350 MPa is observed on the outer surface corresponding to a 0.15 Ti-6Al-4V and 0.85 TiB_2 volume fraction distribution.

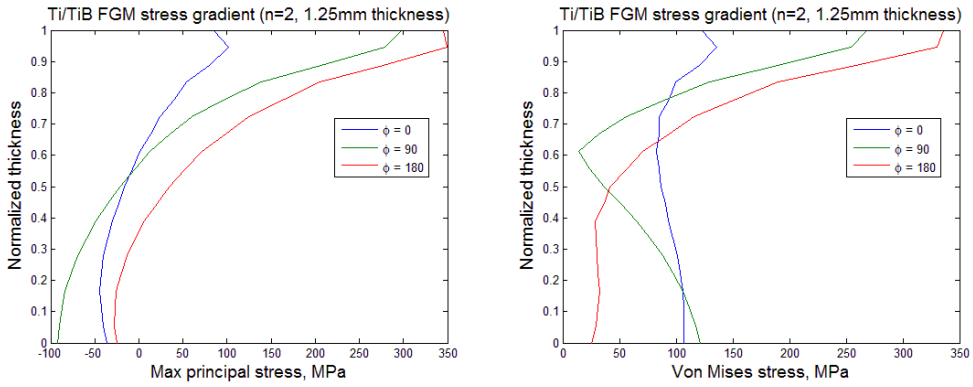

(a) (b)

Figure 5.13. Ti/TiB_2 1D FGM stress gradient (a) maximum principal (b) Von Mises.

Table 5-2. Comparison of outboard deflections:
Ti/TPS vs Ti/TiB2 1D FGM.

Configuration	Mass		Deflection	
	kg	% diff.	mm	% diff.
Ti/TPS	1.4	-	9.4	-
Ti/TiB_2 FGM	1.2	-11	6.8	-28

5.3 Thermal and Thermostructural Analysis: Non-uniform Heat Flux

One of the predominant characteristics of FGMs is the ability to tailor material properties or behavior with the end goal of optimizing and/or producing a desired system response. Thus, the anticipated loading seen by the structure strongly influences the types of materials used and the manner in which they are varied. This becomes even more beneficial due to the fact that one aspect of the thermal loading conditions in hypersonic airframes that is not well understood is the transition from laminar to turbulent flow. With many computational fluid dynamics (CFD) simulations of flight trajectory, the transitional boundary layer between laminar and turbulent flow must be approximated by empirical tools, experimental data or engineering judgment [116]. For this reason, structures are typically assumed to be turbulent over the entire geometry. Such an assumption leads to aerodynamic heating of approximately four to eight times that of laminar flow [117]. Modeling of the correct transitional boundary layers has been found to produce significantly higher thermal gradients, which can result in higher panel temperatures than that of purely turbulent flows [118]. Therefore, working with members of the AFRL Munitions Directorate, the location of the transitional boundary layer has been approximated, and models of the location have been created to determine the influence of non-uniform heating conditions on the thermal and thermostructural response.

For this study, the same representative time-dependent structural and thermal loads used in the uniform heat flux example are utilized and modified to model the

laminar to turbulent transitional heating effects. The temporal- and spatial-dependent laminar heat flux, Q_{lam} is calculated the same as described previously in Eq. (5.1). The transitional boundary layer heat flux Q_{trans} is modeled using the adopted technique of Riley et al. [118], where the laminar to turbulent heat flux transition is a continuous piecewise function as described by

$$Q(x,t) = \begin{cases} Q_{lam}(x,t), & x < x_{on} \\ Q_{trans}(x,t), & x_{on} \le x \le x_{end} \\ Q_{turb}(x,t), & x > x_{end} \end{cases}. \tag{5.2}$$

Here, the heat flux at any location x between the onset, x_{on}, and end location, x_{end} (transitional region), is computed using a Gaussian distribution function as described by Eq. (5.3). The location and amplitude of the heat flux is determined by the overshoot parameters, x_{os} and Q_{os}, respectively, which account for the possibility of heat fluxes exceeding that of turbulent flow, which has been observed in both physical and numerical experiments [119, 120]

$$Q_{trans} = (1 + Q_{os})Q_{turb}|_{x_{os}} e^{\left[-\frac{(x-x_{os})^2}{2\sigma^2}\right]} \tag{5.3}$$

with the standard deviation, σ, defined as

$$\sigma = \sqrt{-\frac{1}{2}(x_{on} - x_{os})^2 / log\left[\frac{Q_{lam}|_{x_{on}}}{(1 + Q_{os})Q_{turb}|_{x_{os}}}\right]} \tag{5.4}$$

For the extent of this work, onset and overshoot locations of $x_{on}/L = 0.3$ and $x_{os}/L = 0.7$ are used along with an overshoot value of $Q_{os} = 0.5$ to study the influence of transitional heating and overshoot effects on traditional layered TPS as well as 1D and 2D graded FGMs. Considering a general case, the laminar, turbulent and transitional heat fluxes are plotted together in Fig. 5.14.

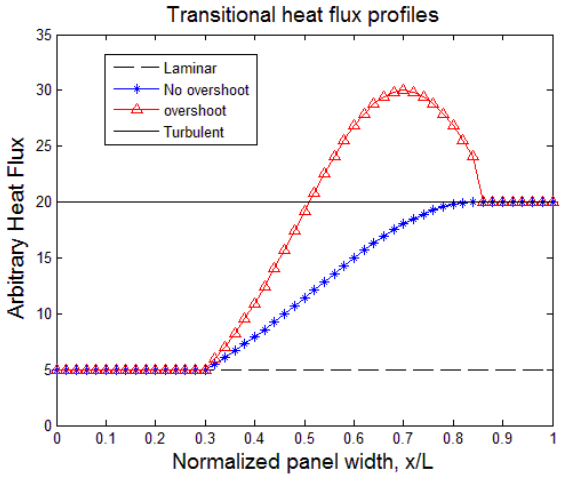

Figure 5.14. Transitional heat flux profiles.

A before, temporal- and spatial-dependent thermal loads are applied to the structural panels using an Abaqus user-defined subroutine DFLUX [115]. Examples of the two types of applied heat flux profiles are provided in Fig. 5.15.

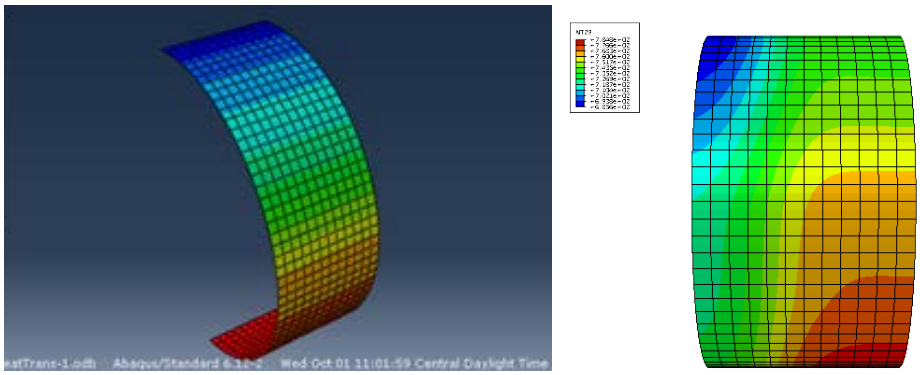

(a) (b)

Figure 5.15. Circumferential (a) and longitudinal and circumferential heat flux profiles (b).

In this example, FGMs are modeled using Eqs. (3.1) and (3.2) for material variation in one and two dimensions. Values chosen in this study for 1D and 2D graded structures were selected such that each created equivalent mass between the 1D and 2D graded systems (1.24 kg). The resulting parameters are summarized in Table 5-3 and shown

graphically in Fig. 5.16. In this work, the 1D and 2D Ti/TiB_2 FGM panels are denoted as Ti/TiB_2 1D FGM and Ti/TiB2 2D FGM, respectively.

Table 5-3. Grading parameters for 1D and 2D Ti/TiB_2 FGMs.

Grading	η_r	η_x	n_r	n_x
1D (through-thickness)	0.9	-	2	-
2D (through-thickness/in-plane)	0.9	1	2	2

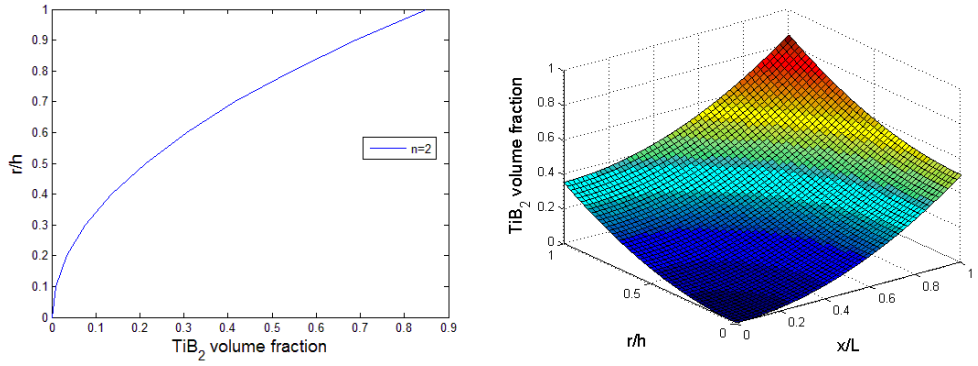

(a) (b)

Figure 5.16. Ti/TiB_2 FGM grading profiles (a) 1D and (b) 2D.

5.3.1 Thermal Response

Applying the transitional heating profiles seen in Fig. 5.14, and applying the same modeling approach as in Section 5.2, the thermal response of the Ti/TPS has been evaluated using overshoot parameters of Q_{os}=0.0 and Q_{os}=0.5. Figures 5.17 and 5.18 provide the thermal response of the Ti/TPS, Ti/TiB_2 1D FGM and Ti/TiB_2 2D FGM material systems subjected to a laminar to turbulent transitional surface heating with overshoot parameters of $Q_{os} = 0$ and $Q_{os} = 0.5$, respectively.

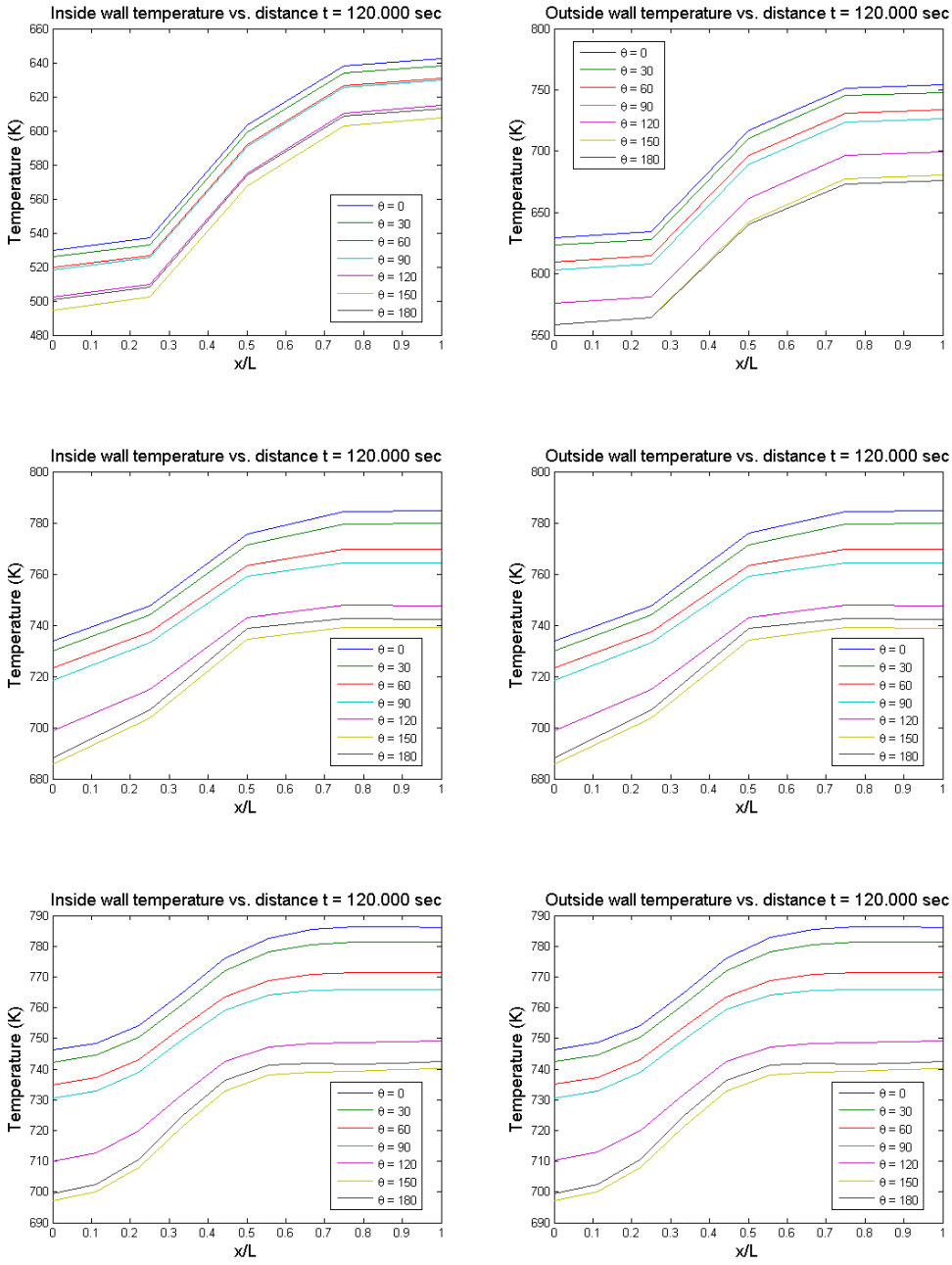

Figure 5.17. Wall temperature vs. normalized panel width subject to transitional heat flux ($\boldsymbol{Q_{os}}$=0.0); from top to bottom: Ti/TPS, Ti/TiB2 1D FGM and TiTiB2 2D FGM. From left to right: inside and outside wall.

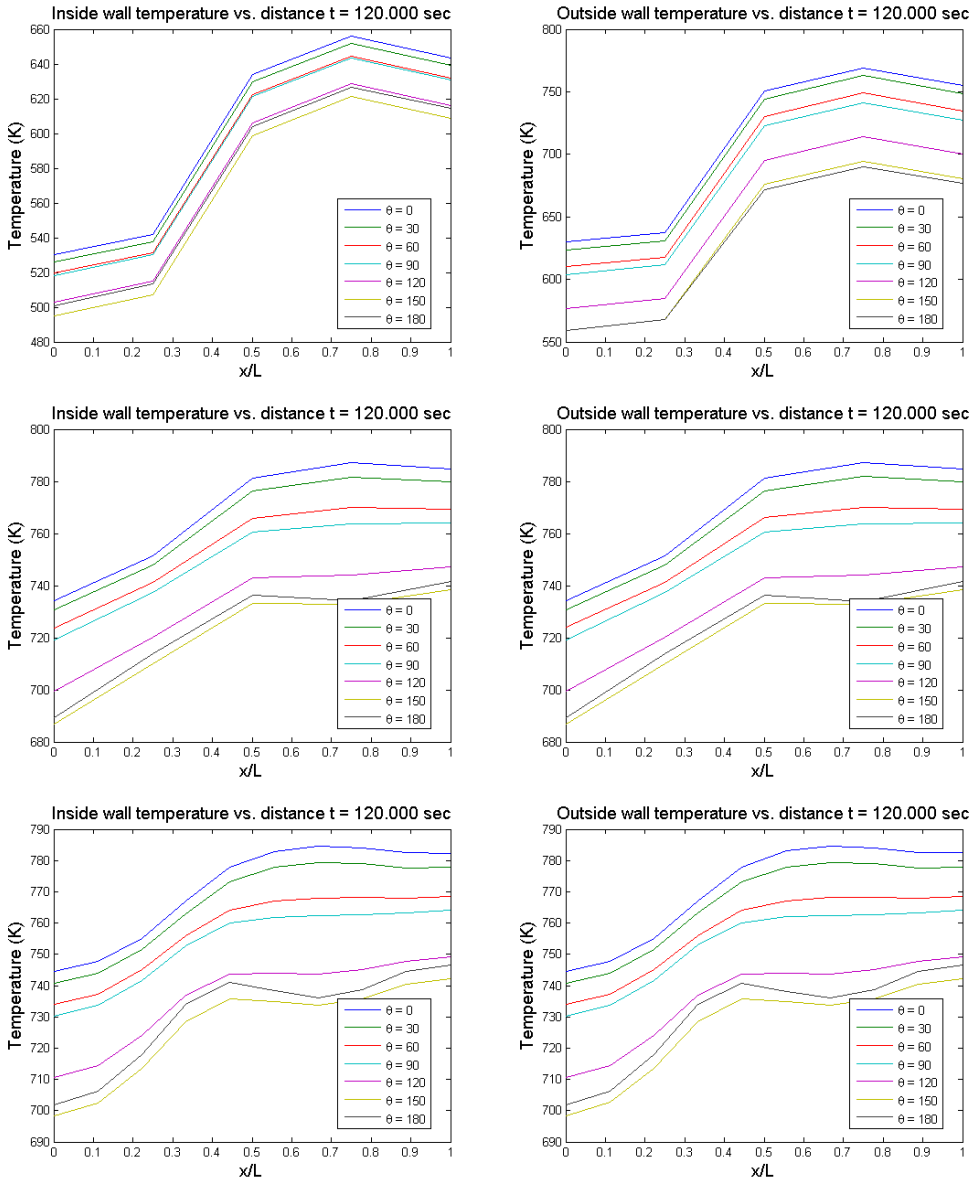

Figure 5.18. Wall temperature vs. normalized panel width subject to transitional heat flux ($\boldsymbol{Q_{os}}$=0.5); from top to bottom: Ti/TPS, Ti/TiB2 1D FGM and TiTiB2 2D FGM. From left to right: inside and outside wall.

When comparing the outside to inside wall temperatures in the above plots, it can be realized that a through-thickness temperature gradient exists in the Ti/TPS system for both transitional heat flux loading cases. Additionally, an in-plane temperature gradient is present on the inside and outside surface of the Ti/TPS system when observing the temperature profiles across the normalized panel width. Both of these thermal gradients

can be clearly seen in Figs. 5.19 and 5.20 for overshoot parameters of 0.0 and 0.5, respectively. Similar to the previous case of laminar heat flux, the graded material systems eliminate the through-thickness temperature gradients that are present in the Ti-6Al-4V/TPS system. Moreover, the longitudinal temperature gradients have been significantly reduced from approximately 133 K for the Ti-6Al-4V/TPS panel to 47 and 38 K for the 1D and 2D FGM panels, respectively. For the particular transitional model parameters chosen in this study, only a 9 K temperature difference is observed. However, for different heating parameters and material system combinations, the efficiency in reducing in-plane temperature gradients may be exploited further. The aim of the current work was to provide a proof of concept for future modeling and investigation.

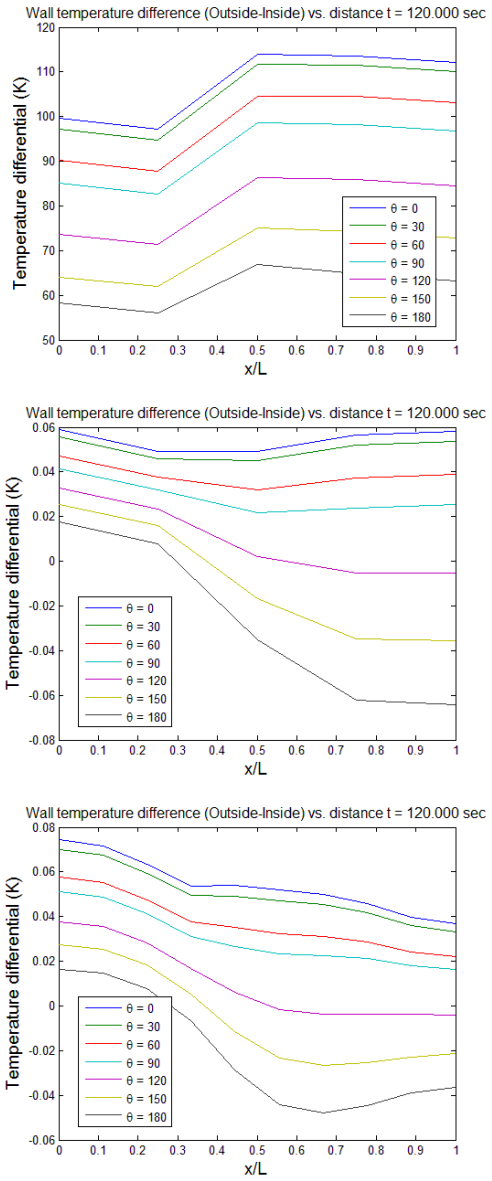

Figure 5.19. Outside and inside wall temperature difference subject to transitional heat flux ($\boldsymbol{Q_{os}}$=0.0) at *t*=120 seconds. From top to bottom: Ti/TPS, Ti/TiB2 1D FGM and TiTiB2 2D FGM.

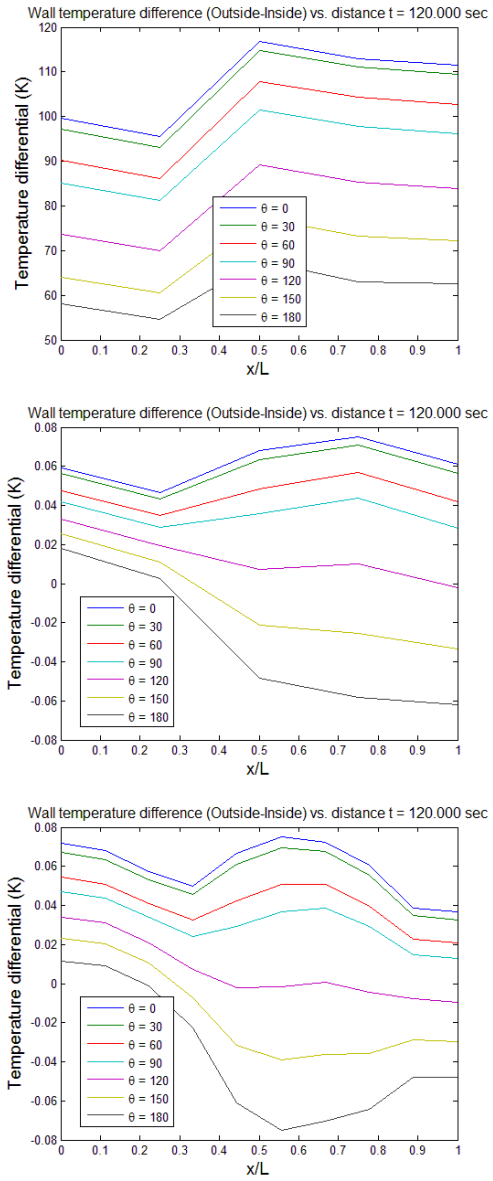

Figure 5.20. Outside and inside wall temperature difference subject to transitional heat flux ($\boldsymbol{Q_{os}}$=0.5) at *t*=120 seconds. From top to bottom: Ti/TPS, Ti/TiB2 1D FGM and TiTiB2 2D FGM.

5.4 Optimization of Spatially Tailored Materials

In the previous sections, grading profiles (through-thickness and in-plane), were chosen using engineering judgement to create a structure with an enhanced, but not necessarily optimal, thermomechanical response,. However, in most cases, this approach will not be useful as surveying multiple material combinations, grading parameters,

trajectories, etc., will become cumbersome to analyze manually. Therefore, the aim of this section is to present a methodology for determining material distribution and topology resulting in an optimal thermostructural response subject to design constraints.

5.4.1 Optimization Procedure

The appeal of spatially tailored materials is the ability to vary the microstructural properties via phase volume fraction manipulation to produce a macro structure that produces an enhanced or desirable thermostructural response. In the context of this work, an enhanced response can be seen as a structure that meets design requirements and constraints at a reduced mass. To present this optimization framework, we once again consider a portion of the entire missile geometry shown in Fig. 5.1. Additionally, we assume that the material variation is continuous following the grading distribution functions in Eq. (3.1) and (3.2). The proposed approach is highlighted by the use of detailed micromechanical models discussed in 0 along with representative thermostructural analysis shown in Sections 5.2 and 5.3, to determine optimal parameters such as spatial distribution, materials and topology over a bounded space and design constraints.

Determination of optimal design parameters is performed using a “black box” approach, where solutions from the structural FEA are piped into an optimization solver. Here, the solver is used to evaluate and determine the next design point in the process. In this work, a sequential quadratic programming (SQP) Matlab algorithm *fmincon*, is used to determine optimal design parameters. This iterative procedure is efficient at finding numerical solutions to constrained nonlinear optimization problems. However, like many optimization techniques, in certain scenarios, SQP is known to succumb to finding local and not global minima. To overcome this potential issue, genetic algorithms (GAs) have been implemented for situations where it is known or expected that many local minima may exist in the design space. Because an analytical solution cannot be used, the

downfall of the FEA "black box" approach is that many function evaluations and duplicate calls are required by the optimization processes, resulting in additional computational expense. To overcome the computational cost, this approach leverages Kriging surrogate models to approximate the response of the system with various configurations. With this hybrid tactic, optimal configurations can be quickly identified with the least amount of computer resources.

The procedure for this approach is to first define the design space and constraints. For this study, this involves defining the minimum and maximum panel thickness and a range of grading parameters for 1D and 2D material variations. Next, a sample of the design space is taken using Latin Hypercube Sampling (LHS) to provide a randomly distributed envelope of parameters. The thermostructural response of these "training" points are then computed using the proposed FEM. Next, a surrogate response surface is generated using Kriging regression modeling. Kriging and the construction of the response surface is accomplished using the design of computer experiments, commonly referred to as DACE, Matlab toolbox [121]. After the response surface is constructed, random points inside the domain (typically, 5x the number of design variables) are used to determine the accuracy of the surrogate by computing the root mean squared error (RMSE), given as

$$RSME = \sqrt{\frac{1}{n}\sum_{i=1}^{n}(x_i - \hat{x}_i)^2} \tag{5.5}$$

where n is the number of samples and x_i and $\hat{x}_i$ are the estimated and true values, respectively, where the estimated value is taken from the surrogate response surface and the true value is assumed to be the FEA solution. The RMSE is used to gauge whether or not the response surface is accurate enough in predicting values needed for the design constraints, such as stress, deflection, temperature and temperature gradient. Acceptable values vary depending on the field response, but in this work values within 10% are

deemed acceptable as initial response surfaces. Outside of this error, it is advised to add additional training points (design points) or place points in regions were the model is more prone to error. With a satisfactory surrogate surface, the optimization solver is then initialized with a starting point, and an optimal design point x^* is determined. Finally, x^* is analyzed using the FEM and compared to the estimated value. If the difference is within some tolerance (typically 2.5%), the optimal value is accepted and the analysis terminated. However, if the difference is outside of the tolerance, the optimal point along with its true value are added to the initial design space, a new response surface is constructed and the analysis is continued. This entire procedure is shown graphically in Fig. 5.21.

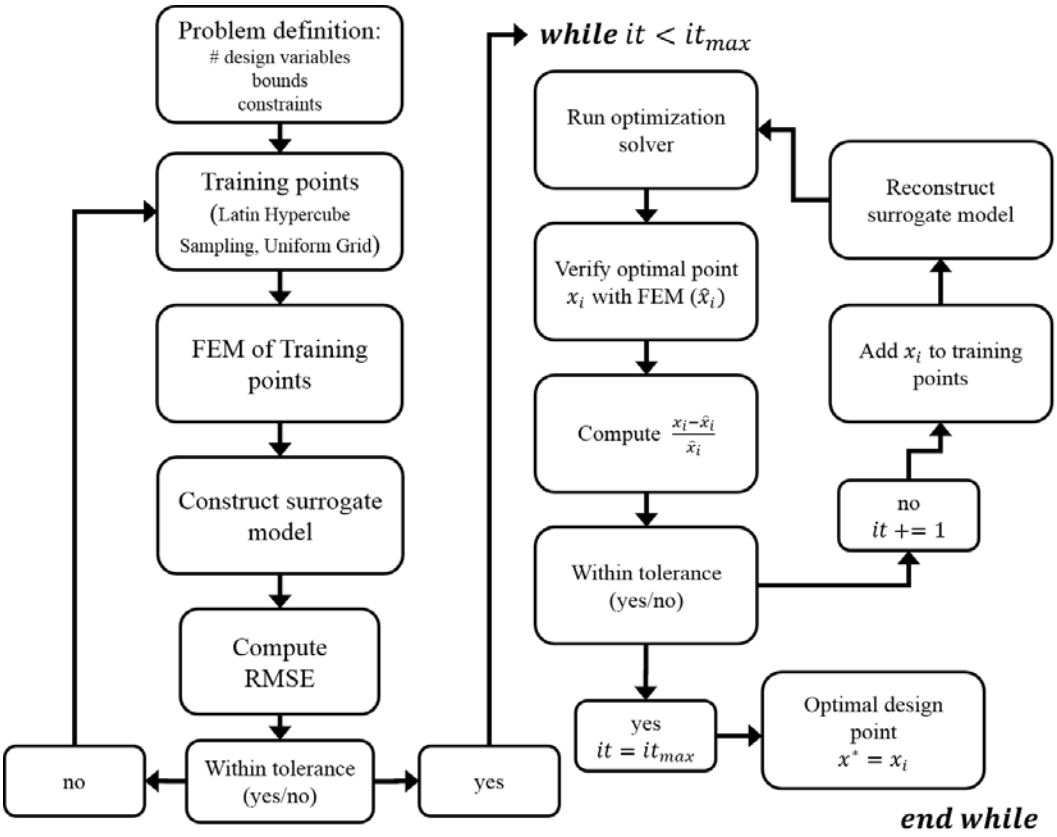

Figure 5.21. Outline of functionally graded panel optimization procedure.

5.4.2 Optimization Examples

To illustrate the various aspects of the optimization procedure, two examples optimizing a FGM hypersonic panel are provided. For this optimization, consider the two-phase Titanium (Ti-6Al-4V) and Zirconia (ZrO_2) FGM, with Ti-6Al-4V and ZrO_2 serving as the metallic and ceramic phases, respectively. The material composition in each example is assumed to be continuous and varies along a single dimension (through-thickness), resulting in the spatially variant volume fractions $v(z)_i$ with $i = 1, 2$, as defined by Eq. (3.1). Throughout the optimization procedure, possible optima designs are assumed to be valid so long as they meet the prescribed constraints. Limitations such as manufacturing to the optimal thickness or grading parameter is not considered. The material properties for Ti-6Al-4V are provided in Table 4-1 and Figs. 4.7-4.9, while material parameters for ZrO_2 are provided in Table 5-4 and Figs. 5.22-5.24. It is also worth mentioning that the density of ZrO_2 used in the following examples is not typical of experimental values found in the literature for low-porosity samples (approximately 4800 to 5600 kg/m^3). Specifics regarding the porosity content and fabrication method used were not disclosed by the authors. The reduced density points towards high-porosity samples fabricated with a low sintering temperature. None-the-less, for the sake of consistency, the authors' experimentally obtained values will be used.

Table 5-4. Material properties of ZrO_2 at 20/500 C [107].

Material	E (GPa)	ν	α (10^{-6}/K)	k (W/m-K)	C_p (kJ/kg-K)	ρ (kg/m^3)
ZrO_2	117/82	0.33	8.85/6.5	1.78/1.98	459/610	3657

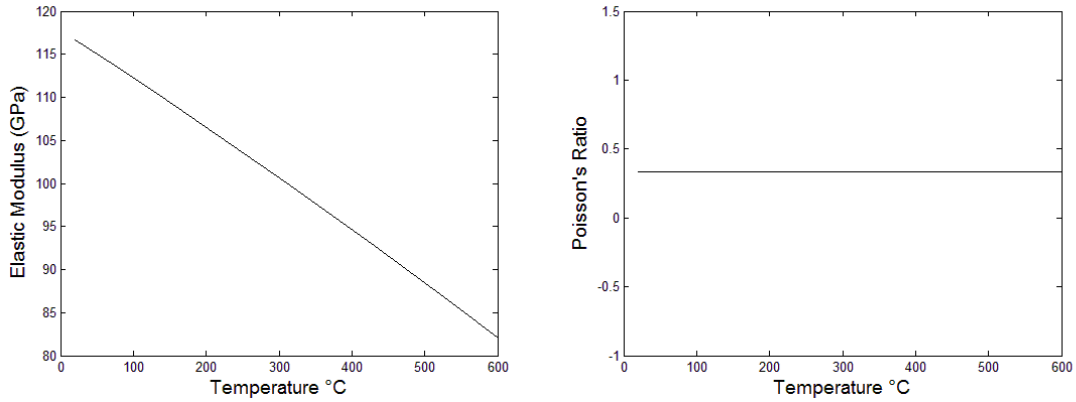

Figure 5.22. Temperature-dependent elastic modulus and Poisson's ratio of ZrO_2 [107].

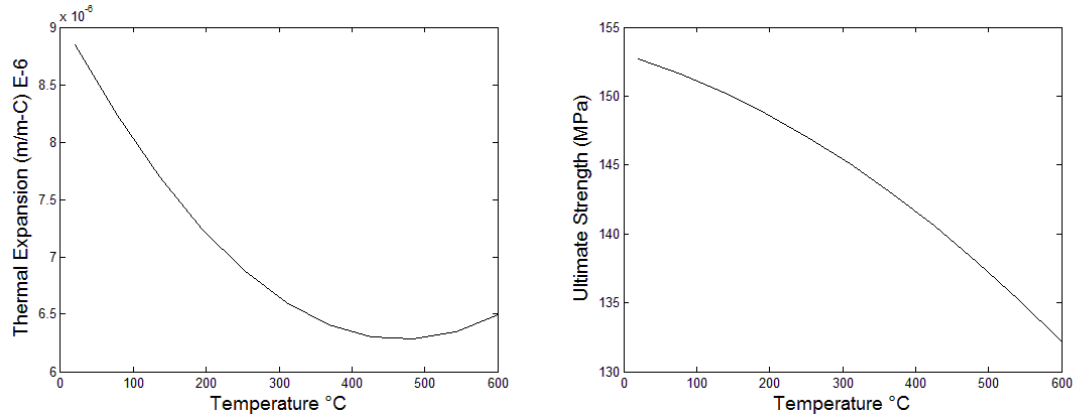

Figure 5.23. Temperature-dependent coefficient of thermal expansion and ultimate strength of ZrO_2 [107].

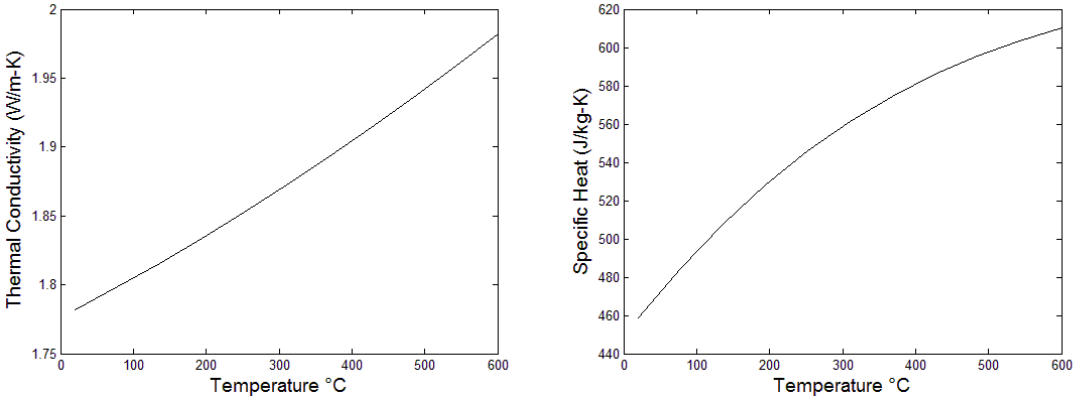

Figure 5.24. Temperature-dependent thermal conductivity and specific heat of ZrO_2 [107].

For the 1D graded panels, the constrained optimization problem is formulated as

$$minimize: m = m(t, n)$$

$$subject\ to: \begin{cases} \sigma - \sigma_{allow} \leq 0 \\ t_{min} \leq t < t_{max} \\ n_{min} < n < n_{max} \\ \eta_{min} < \eta < \eta_{max} \end{cases}. \tag{5.6}$$

Here, m is the system mass as a function of the panel thickness t, through-thickness grading parameter n and density of each material phase, while σ and σ_{allow} are the maximum stress and allowable stress in the outer layer of the panel. The mass for a theoretically continuous material variation is calculated by integrating the effective density through the normalized thickness $\bar{t}$ and/or in-plane directions (normalized panel length $\bar{L}$) for 1D and 2D grading, respectively. For 1D grading in the thickness direction only, m is described by

$$m = \int_0^{\bar{t}} v\rho(\bar{z})d\bar{z} \tag{5.7}$$

where $\bar{t} = 1$ and $\rho(\bar{z})$ is the density as a function of the normalized thickness coordinate $\bar{z}$, which is calculated by

$$\rho(\bar{z}) = \phi_1\rho_1 + \phi_2\rho_2$$
$$\phi_1 = 1 - \phi_2 \tag{5.8}$$

with ϕ_1 and ϕ_2 being the volume fractions of the first and second material phases. The volume v for a cylinder is calculated using the well-known equation

$$v = \pi L(r_o^2 - r_i^2). \tag{5.9}$$

Here, L is the panel length, and r_o and r_i are the outer and inner radius of the cylindrical section. Substitution of Eqs. (5.8) and (5.9) and the 1D grading profile of Eq. (3.1) into (5.7) results in the following relationship

$$m = \pi L(r_o^2 - r_i^2) \int_0^t \left[\left(1 - \eta_z \left({}^{z}/_{h}\right)^{n_z}\right)\rho_1 + \eta_z \left({}^{z}/_{h}\right)^{n_z} \rho_2\right] d\bar{z}. \tag{5.10}$$

Using the variable $\bar{z} = z/h$ and integrating through $\bar{t}$, the mass is found as

$$m = \pi L(r_o^2 - r_i^2)\left[\rho_1 + \frac{\eta_z}{(n_z + 1)}(\rho_2 - \rho_1)\right]. \tag{5.11}$$

A Similar analysis can be completed for material variation in two dimensions. It is worth noting that in Eq. (5.6) only a stress constraint is enforced. While it is possible, and in some scenarios necessary, enforcement of other constraints such as maximum inside wall temperature, outboard deflection, etc., are possible but not considered in the following thermostructural optimization. For each example, we assume that the outer ceramic layer is the limiting mechanical factor, such that failure will first occur on the outermost layer and is limited by the strength of the material at the current temperature. In this case, the maximum principle stress criterion is used, which assumes that the material will fail when the maximum principal stress σ_1 exceeds the uniaxial tensile strength σ_t. Equally, the material is also said to have failed when the minimum principal stress σ_3 is less than the uniaxial compressive strength σ_c. A safe region for the material is defined to be when

$$\sigma_c < \sigma_3 < \sigma_1 < \sigma_t. \tag{5.12}$$

The structural design constraint is enforced by the maximum principal stress σ of the outer material layer, which is normalized by the ultimate strength S_{ut} at a given temperature T of the panel described by

$$\tilde{\sigma} = \frac{\sigma}{S_{ut}(T)} \tag{5.13}$$

During post-processing, the maximum normalized principal stress $\tilde{\sigma}$ is calculated to determine the status of the structural constraint. Elements with values greater than one are presumed to have violated the mechanical stress constraint.

For most structural ceramic materials, the strength is commonly measured in a flexural mode with the strength of the brittle material limited by the quantity and distribution of flaws in the specimen. To account for variability within each specimen, a two-parameter Weibull analysis is recommended and frequently used [122]. In this statistical model, the probability of failure P_F at an applied stress σ is given by

$$P_F = 1 - exp\left[-\left(\frac{V}{V_0}\right)(\sigma/\sigma_0)^m\right] \tag{5.14}$$

where V and V_0 are the specimen volume and volume scaling parameter, and σ_0 and m are the characteristic strength and Weibull modulus. Here, m is a measure of flaws within the specimen, with larger values indicating less variability, and larger values of σ_0 implying greater strength. While the flexural strength is a common measure for structural ceramics, the uniaxial tensile strength is a more convenient form from a structural analysis point of view. Therefore, a statistical representation of the uniaxial tensile strength is adopted from Munro [122], which, assuming the specimen volumes are the

same, relates the four-point bend test with the quarter-point loading mean strength $\bar{\sigma}_{4-point}$ to the uniaxial tensile mean strength $\bar{\sigma}_t$, using the following:

$$\frac{\bar{\sigma}_{4-point}}{\bar{\sigma}_t} = \left[\frac{4(m+1)^2}{m+2}\right]^{1/m}. \tag{5.15}$$

Similar relationships can be made for other loading conditions such as three-point bending. For further information and details, the reader is directed to Wachtman's thorough discussion [123]. For scenarios when the material strength is not provided in terms of a tensile values, this conversion from flexural strength to tensile strength $\bar{\sigma}_t$ is used to determine the structural design constraint for the optimization procedure.

5.4.2.1 Critical Loading Condition, Stress Constraint

This first example entails determining the optimal material variation and thickness of a Ti/ZrO_2 FGM panel subject to a critical loading conditions. These conditions include a uniform temperature distribution of 800 K (in-plane and through-thickness), mechanical bending moments applied normal to the cylindrical cross-sections longitudinal axis, forces in the shearing and axial directions and aerodynamic pressure load. The magnitude of the loads is taken from the trajectory data during the transition from cruise to descent phase as indicated by the red circle in Fig. 5.25. This time step in the trajectory is chosen because it has been noted to generate peak structural and thermal loads.

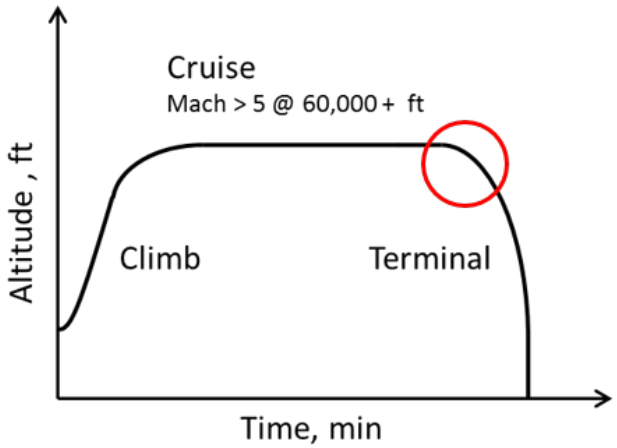

Figure 5.25. Outline of functionally graded panel optimization procedure.

Appling the method outlined in the previous section, the two-variable design optimization is carried out assuming a material variation profile described by Eq. (3.1) with a maximum ceramic content parameter $\eta_z = 1$. The optimization problem for this example, hence forth referred to as Example 1, is formulated as

$$minimize: m = m(t, n)$$

$$subject\ to: \begin{cases} \tilde{\sigma} - 1 \leq 0 \\ 0.25 \leq t < 3.0\ mm. \\ 0.25 < n < 3.0 \end{cases} \tag{5.16}$$

A uniform distribution of 16 design points was used to construct the initial surface response along with the cost function surface (mass vs. thickness and grading parameter) both of which are provided in Fig. 5.26. From here it can be seen that the unconstrained optimal point lies at the minimum thickness and grading parameter point (0.25, 0.25). However, examining the surrogate stress ratio $\tilde{\sigma}$ response surface in Fig. 5.27, it can be seen that the feasible region must lie on $\tilde{\sigma} \leq 1$.

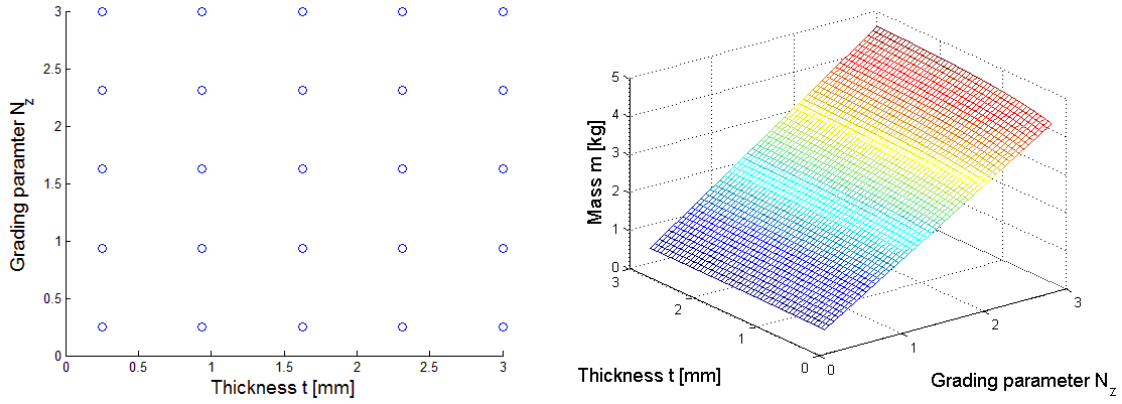

(a) (b)

Figure 5.26. Example 1 (a) design space sample points (b) cost function surface.

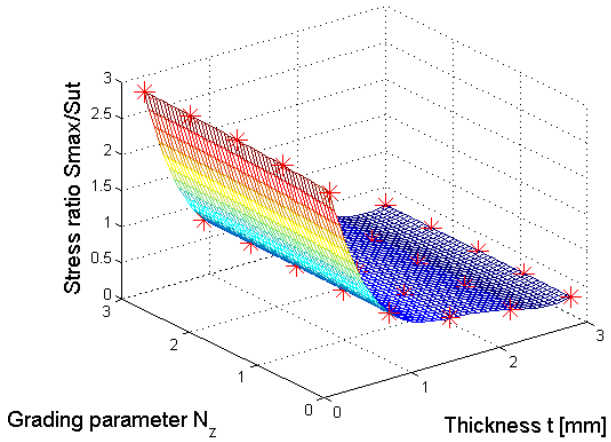

Figure 5.27. Example 1 initial stress ratio surrogate response surface with red markers indicating the points used to construct the surface.

The accuracy of the of the initial stress ratio surrogate using the RMSE provided in Eq. (5.5) was found to be 0.0879, using a random sampling of 10 points within the design envelope. Setting the initial point x_0 equal to the average of the minimum and maximum of both variables, the constrained optimal design variables leads to a 58.4% reduction in mass when compared to the Ti/TPS configuration of 2.25 kg. The resulting optimal design variables for varying values of $\tilde{\sigma}$ constraints and the corresponding volume

fraction distribution can be seen in Table 5-5 and Fig. 5.28, respectively. During this analysis five surrogate regenerations were performed using a tolerance value of 5%.

Table 5-5. ZrO_2 1D FGM panel optimal values: Critical loads.

Normalized stress	Optimal Values		
	Thickness (mm)	Grading Parameter	Mass (kg)
σ/S_{ut}	t	n_z	m
1.0	0.686	0.25	0.937
0.9	0.815	0.25	1.114
0.8	0.883	0.25	1.207
0.7	0.9662	0.25	1.321

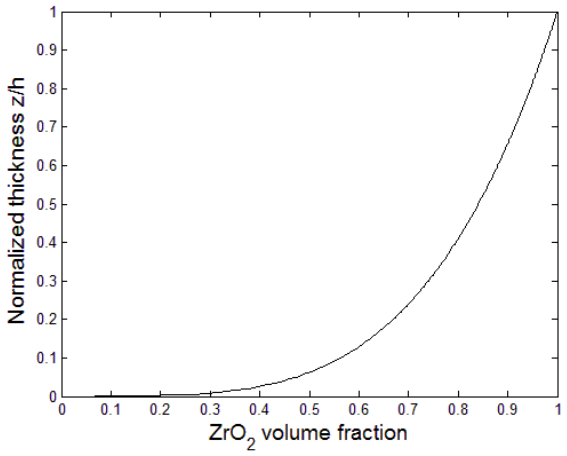

Figure 5.28. Example 1 resulting optimal material distribution.

As can be seen above, the panel is ceramic dominated due to ZrO_2 having a mass density significantly lower than that of Ti-6Al-4V (4420 vs 3657 kg/m^3). Additionally, the lower the grading parameter n_z, the more uniform the stress distribution is within the panel, eliminating stress concentrations due to the mismatch in the phase material's Young's modulus and CTE. While this example can be seen as trivial due to the shape of the cost function and response surface, it serves as a verification of the proposed optimization process and garners confidence for more complicated models.

5.4.2.2 Full Trajectory Analysis, Stress Constraint

The objective of this example (Example 2) is to highlight the capabilities of the proposed optimization procedure by determining the optimal design parameters of an FGM panel with material variation in one dimension (through-thickness). In this analysis, the representative geometry is subjected to temporal- and spatial-dependent heating and axial and shearing forces in addition to bending moments and aerodynamic pressure as a function of the characteristic hypersonic trajectory, as outlined in Section 5.1. As with Example 1, the material variation is prescribed by Eq. (3.1) with a maximum ceramic content parameter $\eta_z = 1$, with the design bounds and constraints defined by Eq. (5.16). The analysis uniform sample space and the cost function surface are the same, as shown previously in Fig. 5.26. The stress ratio response surface with an RSME of 0.1057 over 10 random points is provided in Fig. 5.29.

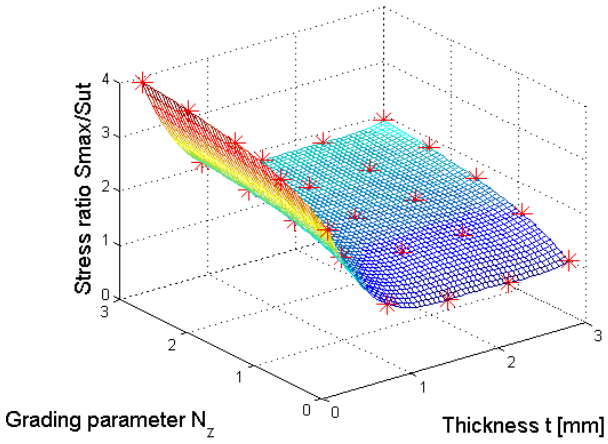

Figure 5.29. Maximum stress ratio surrogate response surfaces with red markers indicating the points used to construct the surface.

With no surrogate model regenerations required using a 5% tolerance on $\tilde{\sigma}$, the resulting optimal design variables and response of the time-dependent optimization are provided in Table 5-6. This optimal design leads to a 31.2% reduction in mass compared to the Ti/TPS configuration of 2.25 kg. However, it is worth noting as a reminder that this

analysis was performed without consideration of maximum outboard deflection or thermal constraints such as maximum inside wall temperature or thermal gradient. The following analysis will add to the current example by considering the maximum inside wall temperature as a thermal constraint. The resulting optimal volume fraction distribution for the panel subjected to temporal- and spatial-dependent thermal and mechanical loads is the same as shown previously in Fig. 5.28. Based on the reasoning previously mentioned, the graded panel is ceramic dominated. However, in this analysis, the effects of the full trajectory are revealed as the panel in this case has an increased thickness and corresponding mass.

Table 5-6. ZrO_2 1D FGM panel optimal values: Full trajectory analysis, stress constraint.

Design Variables	Optimal values
Thickness (mm), t	1.132
Grading Parameter, n_z	0.250
Mass (kg), m	1.549

5.4.2.3 Full Trajectory Analysis, Stress and Temperature Constraints

Building on the previous analysis, a 1D optimization is carried out with consideration of structural and thermal constraints, referred to as Example 3. In this scenario, a maximum inside wall temperature T_{in}^{max} is used to reduce the feasible region to models with temperatures $\leq T_{in}^{max}$. The design space in this example are the same as the previous two examples; however, introduction of the temperature constraint leads to the following description:

$$minimize: m = m(t, n)$$

$$subject\ to: \begin{cases} \tilde{\sigma} - 1 \leq 0 \\ T_{in} - T_{in}^{max} \leq 0 \\ 0.25 \leq t < 3.0\ mm \\ 0.25 < n < 3.0 \end{cases} \tag{5.17}$$

where T_{in} is the maximum time-dependent inside wall temperature during the trajectory. Enforcement of the thermal constraint requires surrogate response surfaces of T_{in} as shown in Fig. 5.30. The RMSE of the initial response surface was determined to be 5.121 K for the uniform grid sample. Enforcement of the stress constraint is handled in the same fashion as the previous example with the stress ratio response surface in Fig. 5.29. Table 5-7 shows the optimal design parameters and resulting mass when the optimization is constrained by varying T_{in}^{max} and $\tilde{\sigma} = 1$.

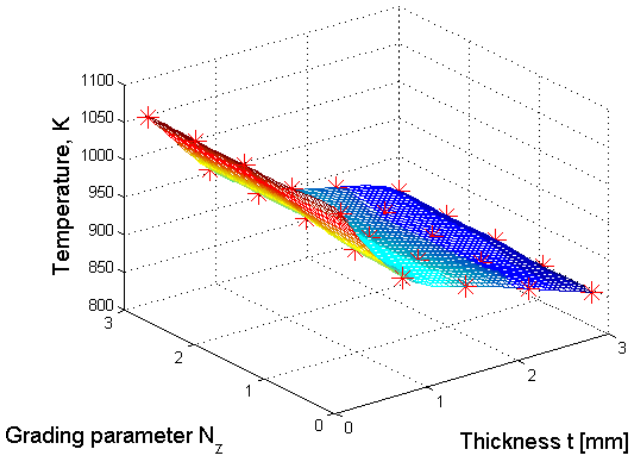

Figure 5.30. Maximum inside temperature wall temperature surrogate response surface.

Table 5-7. ZrO_2 1D FGM panel optimal values: Full trajectory analysis, stress and temperature constraint.

Max. Inside Wall Temp. (K)	Optimal Values		
	Thickness (mm)	Grading Parameter	Mass (kg)
T_{in}^{max}	t	n_z	m
950	1.132	0.25	1.549
900	1.629	0.25	2.232
850	2.866	0.25	3.939

As is shown in the above Table, introduction of the maximum inside wall temperature constraint results in an increase in the thickness and accordingly the mass of the panel. Additionally, it can be seen that for $T_{in}^{max} = 850\ K$ the mass of the panel exceeds that of the base design, thus emphasizing the importance of incorporating thermal design constraints into the optimization procedure.

CHAPTER 6

CONCLUSIONS

This dissertation investigates the effective thermostructural response of spatially tailored metal-ceramic composites for use in the hypersonic environment. To achieve this, an all-inclusive numerical framework has been proposed to study the effective material properties of graded hypersonic airframes and the effective thermostructural response when subjected to representative hypersonic thermal and structural loads. Additionally, using information regarding the effective material properties and effective thermostructural response, the developed model is used to determine desirable material distribution to create an optimal or enhanced system response using a developed optimization procedure.

6.1 Modeling of Graded Microstructures

Numerical algorithms enabling the creation of artificial graded microstructures consisting of disks and spheres, representing particulate-reinforced functionally graded composite materials, has been developed. The algorithms have been efficiently constructed by linking the packing algorithms coded in FORTRAN, with Abaqus/CAE using the Python scripting interface to create high-resolution graded microstructures with dense packing fractions up to 0.61 and 0.91 for 2D and 3D geometries, respectively. Realization of dense packing fractions enables one to investigate the effective properties of particulate-reinforced composites over a wider reinforcement volume fraction range when compared to those reported in the literature.

6.2 Effective Material Properties of Graded Composites

Effective thermomechanical properties of Ti/TiB_2 metal-ceramic functionally graded composite materials have been obtained over a wide temperature range up to 500 °C. A comprehensive study has been performed to determine the validity of using

classical homogenization techniques, which were originally developed for fixed volume fraction composites, for FGMs with 1D and 2D grading. Both variational bounds and finite element numerical homogenization of RVEs were studied. Two different types of RVEs (Piecewise Layered RVE and Continuous FGM RVE) were created and analyzed to determine an adequate representative model for numerical homogenization. Moreover, the effect of grading on the estimation of the effective property was also studied. To evaluate this potential influence, three types of material grading were analyzed: a linear smooth transition from metal to ceramic, a quadratic distribution resulting in a slow transition and a square root distribution with a rapid transition from metal to ceramic. Each choice of RVE was found to produce similar results when compared to the others. Furthermore, both models were found to produce similar effective properties to those obtained from 3D Layered RVE models. Lastly, models were found to be within or close to the rigorous Hashin and Shtrikman, Schapery and Rosen and Hashin bounds of elasticity, thermal conductivity, thermal expansion and specific heat, respectively. In short, it was found that the choice of RVE and the influence of grading did not have a significant effect on the estimation of the effective properties of the metal-ceramic graded composites.

Detailed investigations were performed on the effects of transition zones, which are regions where the properties of the FGM are neither matrix, nor reinforcement dominated (i.e., the volume fractions of the constituents are comparable). It was found that effective properties obtained using numerical homogenization are greatly dependent on the assumptions regarding the evolution of the microstructure and the assignment of the matrix and reinforcement phases. Therefore, image-based modeling of actual microstructures might be beneficial for obtaining the effective properties at the transition zones.

The proposed holistic model was validated by extending the modeling capabilities to incorporate a third material phase. By assigning void material properties to this third

phase, the obtained effected properties were compared to those obtained experimentally for each respective material parameter. It was found that the proposed model can accurately predict the effective material response of materials exhibiting spatially dependent material concentration and thus spatially dependent material properties.

Lastly, using the extended three-phase model, the effect of manufacturing defects or enhancements, such as voids and porosity, were studied. Here, the quantity and distribution profile of porosity was examined to understand the role of voids on the effective thermostructural response. In general, this study found that the magnitude of the porosity had a greater influence on the effective response when compared to the morphology or variation of porosity in the heterogeneous material system.

6.3 Thermostructural Analysis of Functionally Graded Hypersonic Panels

The thermomechanical response of Ti/TPS and Ti/TiB_2 FGM structural panels for a high-speed airframe was evaluated. In this analysis, heating loads with spatial dependence on the clocking angle (known here as uniform) were applied to the structures. Thermal response of the Ti/TiB_2 FGM exhibiting material variation in the through-thickness direction only were found to drastically reduce the through-thickness temperature gradient found in the Ti/TPS benchmark investigation. As a result of reducing the through-thickness temperature gradients and the amount of contrast in the stiffness and thermal expansion, a reduction in the through-thickness stress concentrations in this time range were observed. Moreover, in addition to a uniform temperature and reduction in stress gradients, the deformation and overall panel weight was also reduced.

The concept of spatial variation was further exploited by considering the thermal response of Ti/TPS and Ti/TiB_2 FGM structural panels with 1D and 2D material variation. Heating loads with spatial dependence on the clocking angle and longitudinal axis (known here as non-uniform) were applied to the structural panels. Results of this

study indicate that 1D and 2D graded structures can eliminate the through-thickness temperature gradients in addition to significantly reducing the in-plane surface temperature gradients, with 2D grading offering the greatest reduction.

6.4 Optimization of Spatially Tailored Materials

The optimization of heterogeneous materials has been demonstrated by investigating a Ti/Zr metal-ceramic FGM thermostructural panel operating in the hypersonic environment. In this study, an adaptive surrogate modeling technique was employed to reduce the computation cost associated with analyzing a wide design space along with a sequential quadratic programing algorithm to determine desirable material variation. Three different optimization problems were formulated to study the effect of constraints and loading history on the optimal material distribution. In the first exploration, a steady-state analysis was performed using a uniform temperature distribution and maximum structural loading in the supplied data. The second and third analyses utilized thermal and structural loads with full temporal dependence and stress only and stress/temperature constraints, respectively. Results of each of these studies demonstrate that incorporating spatially tailored materials into structural designs allows them to operate in the harsh hypersonic environment and at the same time creates a structure with reduced system mass by exploiting the concept of multifunctionality.

REFERENCES

1. Witeof, Z.D. and C.L. Pasiliao, Fluid-Thermal-Structural Interation Effects in Preliminary Desing of High Speed Vehicles, in 56th AIAA/ASCE/AHS/ASC Structures, Structural Dynamics, and Materials Conference. 2015: Kissimmee, FL.
2. Birman, V., et al., Response of spatially tailored structures to thermal loading. J Eng Math, 2008. 61: p. 201-217.
3. Voigt, W., Theoretische studien über die elasticitätsverhältnisse der krystalle. 1887: Königliche Gesellschaft der Wissenschaften zu Göttingen.
4. Reuss, A., Berechnung der Flieggrenze yon Mischkristallen auf Grund der Plastizithtsbedingung fiir Einkristalle. Z. Angew. Math. Mech. 9.
5. Hill, R., The elastic behaviour of a crystalline aggregate. Proceedings of the Physical Society. Section A, 1952. 65(5): p. 349.
6. Hashin, Z. and S. Shtrikman, A variational approach to the theory of the elastic behaviour of multiphase materials. Journal of the Mechanics and Physics of Solids, 1963. 11(2): p. 127-140.
7. Hill, R., A self-consistent mechanics of composite materials. Journal of the Mechanics and Physics of Solids, 1965. 13(4): p. 213-222.
8. Budiansky, B., On the elastic moduli of some heterogeneous materials. Journal of the Mechanics and Physics of Solids, 1965. 13(4): p. 223-227.
9. Lydzba, D., Effective properties of composites: Introduction to Micromechanics. Wroclaw University of Technology, PRINTPAP, Wroclaw, 2011.
10. Turner, P.S., Thermal Expansion Stresses in Reinforced Plastics, in U.S. Department of Commerce, National Bureau of Standards. 1946.
11. Kerner, E., The elastic and thermo-elastic properties of composite media. Proceedings of the physical society. Section B, 1956. 69(8): p. 808.
12. Levin, V., On the Coefficients of Thermal Expansion of Heterogeneous Materials. Mekhanika Tverdogo Tela, 1967.
13. Schapery, R.A., Thermal expansion coefficients of composite materials based on energy principles. Journal of Composite Materials, 1968. 2(3): p. 380-404.
14. Rosen, B.W. and Z. Hashin, Effective thermal expansion coefficients and specific heats of composite materials. International Journal of Engineering Science, 1970. 8(2): p. 157-173.
15. Budiansky, B., Thermal and thermoelastic properties of isotropic composites. Journal of composite Materials, 1970. 4(3): p. 286-295.
16. Wiener, O., Die Theorie des Mischkorpers fur das Feld der stationaren Stromung. Abh. Math.-Phys. Kl. Konigl. Sachs. Ges. Wissen, 1912. 32: p. 509-604.
17. Bruggeman, V.D., Berechnung verschiedener physikalischer Konstanten von heterogenen Substanzen. I. Dielektrizitätskonstanten und Leitfähigkeiten der Mischkörper aus isotropen Substanzen. Annalen der physik, 1935. 416(8): p. 665-679.
18. Landauer, R., The electrical resistance of binary metallic mixtures. Journal of Applied Physics, 1952. 23(7): p. 779-784.
19. Hashin, Z., Assessment of the self consistent scheme approximation: conductivity of particulate composites. Journal of Composite Materials, 1968. 2(3): p. 284-300.

20. Hashin, Z. and S. Shtrikman, A variational approach to the theory of the effective magnetic permeability of multiphase materials. Journal of applied Physics, 1962. 33(10): p. 3125-3131.
21. Rosen, B.W., Ph.D. Dissertation. 1968, University of Pennsylvania.
22. Sevostianov, I. and M. Kachanov, Connections between elastic and conductive properties of heterogeneous materials. Advances in applied mechanics, 2009. 42: p. 69-252.
23. Kamiński, M., Homogenization of transient heat transfer problems for some composite materials. International journal of engineering science, 2003. 41(1): p. 1-29.
24. Shabana, Y.M. and N. Noda, Numerical evaluation of the thermomechanical effective properties of a functionally graded material using the homogenization method. International Journal of Solids and Structures, 2008. 45(11): p. 3494-3506.
25. Yu, W. and T. Tang, A variational asymptotic micromechanics model for predicting thermoelastic properties of heterogeneous materials. International Journal of Solids and Structures, 2007. 44(22): p. 7510-7525.
26. Chen, Y., R. Huang, and Z. Huang, Effect of residual interface stresses on effective specific heats of multiphase thermoelastic nanocomposites. Acta Mechanica, 2014. 225(4-5): p. 1107-1119.
27. Sutradhar, A. and G.H. Paulino, The simple boundary element method for transient heat conduction in functionally graded materials. Computer Methods in Applied Mechanics and Engineering, 2004. 193(42): p. 4511-4539.
28. Ochiai, S., Mechanical properties of metallic composites. 1993: CRC Press.
29. Thorpe, T.E., Kopp memorial lecture. L.—The life work of Hermann Kopp. Journal of the Chemical Society, Transactions, 1893. 63: p. 775-815.
30. Hill, R., Elastic properties of reinforced solids: some theoretical principles. Journal of the Mechanics and Physics of Solids, 1963. 11(5): p. 357-372.
31. Chawla, N., V. Ganesh, and B. Wunsch, Three-dimensional (3D) microstructure visualization and finite element modeling of the mechanical behavior of SiC particle reinforced aluminum composites. Scripta Materialia, 2004. 51(2): p. 161-165.
32. Ganesh, V. and N. Chawla, Effect of particle orientation anisotropy on the tensile behavior of metal matrix composites: experiments and microstructure-based simulation. Materials Science and Engineering: A, 2005. 391(1): p. 342-353.
33. Gudlur, P., A. Muliana, and M. Radovic, Effective thermo-mechanical properties of aluminum–alumina composites using numerical approach. Composites Part B: Engineering, 2014. 58: p. 534-543.
34. Chawla, N., et al., Microstructure-based simulation of thermomechanical behavior of composite materials by object-oriented finite element analysis. Materials Characterization, 2002. 49(5): p. 395-407.
35. Kumlutaş, D., I.H. Tavman, and M.T. Çoban, Thermal conductivity of particle filled polyethylene composite materials. Composites science and technology, 2003. 63(1): p. 113-117.
36. Sozhamannan, G., S.B. Prabu, and R. Paskaramoorthy, Failures analysis of particle reinforced metal matrix composites by microstructure based models. Materials & Design, 2010. 31(8): p. 3785-3790.
37. Prabu, S.B. and L. Karunamoorthy, Microstructure-based finite element analysis of failure prediction in particle-reinforced metal–matrix composite. journal of materials processing technology, 2008. 207(1): p. 53-62.

38. Adams, D.F. and D.R. Doner, Transverse normal loading of a unidirectional composite. Journal of composite Materials, 1967. 1(2): p. 152-164.
39. Adams, D.F. and D.R. Doner, Longitudinal shear loading of a unidirectional composite. Journal of Composite Materials, 1967. 1(1): p. 4-17.
40. Tucker III, C.L. and E. Liang, Stiffness predictions for unidirectional short-fiber composites: review and evaluation. Composites science and technology, 1999. 59(5): p. 655-671.
41. Hua, Y. and L. Gu, Prediction of the thermomechanical behavior of particle-reinforced metal matrix composites. Composites Part B: Engineering, 2013. 45(1): p. 1464-1470.
42. Mishnaevsky, L. and S. Schmauder, Advanced finite element techniques of analysis of the microstructure-mechanical properties relationships in heterogeneous materials: a review. Physical Mesomechanics, 1999. 2(3): p. 5-20.
43. Mishnaevsky, L.L. and S. Schmauder, Continuum mesomechanical finite element modeling in materials development: A state-of-the-art review. Applied Mechanics Reviews, 2001. 54(1): p. 49-67.
44. Segurado, J. and J. Llorca, A numerical approximation to the elastic properties of sphere-reinforced composites. Journal of Mechanics and Physics of Solids, 2002. 50: p. 2107-2121.
45. LLorca, J. and J. Segurado, Three-dimensional multiparticle cell simulations of deformation and damage in sphere-reinforced composites. Materials Science and Engineering: A, 2004. 365(1): p. 267-274.
46. Aboudi, J., S.M. Arnold, and B.A. Bednarcyk, Micromechanics of composite materials: a generalized multiscale analysis approach. 2013: Butterworth-Heinemann.
47. Paley, M. and J. Aboudi, Micromechanical analysis of composites by the generalized cells model. Mechanics of Materials, 1992. 14(2): p. 127-139.
48. Moulinec, H. and P. Suquet, A numerical method for computing the overall response of nonlinear composites with complex microstructure. Computer methods in applied mechanics and engineering, 1998. 157(1): p. 69-94.
49. Moulinec, H. and P. Suquet, Comparison of FFT-based methods for computing the response of composites with highly contrasted mechanical properties. Physica B: Condensed Matter, 2003. 338(1): p. 58-60.
50. Michel, J., H. Moulinec, and P. Suquet, Effective properties of composite materials with periodic microstructure: a computational approach. Computer methods in applied mechanics and engineering, 1999. 172(1): p. 109-143.
51. Ghossein, E. and M. Lévesque, A fully automated numerical tool for a comprehensive validation of homogenization models and its application to spherical particles reinforced composites. International Journal of Solids and Structures, 2012. 49(11): p. 1387-1398.
52. Khan, K.A. and A.H. Muliana, Effective thermal properties of viscoelastic composites having field-dependent constituent properties. Acta mechanica, 2010. 209(1-2): p. 153-178.
53. Özdemir, I., W. Brekelmans, and M. Geers, Computational homogenization for heat conduction in heterogeneous solids. International journal for numerical methods in engineering, 2008. 73(2): p. 185-204.
54. Nam, T.H., G. Requena, and P. Degischer, Thermal expansion behaviour of aluminum matrix composites with densely packed SiC particles. Composites Part A: Applied Science and Manufacturing, 2008. 39(5): p. 856-865.

55. Hazanov, S. and C. Huet, Order relationships for boundary conditions effect in heterogeneous bodies smaller than the representative volume. Journal of the Mechanics and Physics of Solids, 1994. 42(12): p. 1995-2011.
56. Hazanov, S., Hill condition and overall properties of composites. Archive of Applied Mechanics, 1998. 68(6): p. 385-394.
57. Huet, C., Application of variational concepts to size effects in elastic heterogeneous bodies. Journal of the Mechanics and Physics of Solids, 1990. 38(6): p. 813-841.
58. Amieur, M., S. Hazanov, and C. Huet. Numerical and experimental assessment of the size and boundary conditions effects for the overall properties of granular composite bodies smaller than the representative volume. in IUTAM Symposium on Anisotropy, Inhomogeneity and Nonlinearity in Solid Mechanics. 1995. Springer.
59. Huet, C., Coupled size and boundary-condition effects in viscoelastic heterogeneous and composite bodies. Mechanics of Materials, 1999. 31(12): p. 787-829.
60. Al Kassem, G., Micromechanical material models for polymer composites through advanced numerical simulation techniques. 2009, Aachen University
61. Dassault Systemes, Abaqus 6.12 documentation. 2012: Providence, Rhode Island.
62. Karch, C., Micromechanical Analysis of Thermal Expansion Coefficients. Modeling and Numerical Simulation of Material Science, 2014. 4(03): p. 104.
63. Koizumi, M., FGM activities in Japan. Composites Part B: Engineering, 1997. 28(1): p. 1-4.
64. Miyamoto, Y., et al., Functionally graded materials: design, processing and applications. Vol. 5. 2013: Springer Science & Business Media.
65. Torquato, S., O. Uche, and F. Stillinger, Random sequential addition of hard spheres in high Euclidean dimensions. Physical Review E, 2006. 74(6): p. 061308.
66. Rintoul, M.D. and S. Torquato, Reconstruction of the structure of dispersions. Journal of Colloid and Interface Science, 1997. 186(2): p. 467-476.
67. Lubachevsky, B.D. and F.H. Stillinger, Geometric properties of random disk packings. Journal of statistical Physics, 1990. 60(5-6): p. 561-583.
68. Ghossein, E. and M. Levesque, A fully automated numerical tool for a comprehensive validation of homogenization models and its application to spherical particles reinforced composites. Int. J. Solids and Structures, 2012. 49: p. 1387-1398.
69. Jaeger, H.M. and S.R. Nagel, Physics of the granular state. Science, 1992. 255(5051): p. 1523-1531.
70. Jacobson, A., Maximal Sphere Packing. 2010, Aug.
71. Donev, A., S. Torquato, and F.H. Stillinger, Neighbor list collision-driven molecular dynamics simulation for nonspherical hard particles.: II. applications to ellipses and ellipsoids. Journal of Computational Physics, 2005. 202(2): p. 765-793.
72. Lee, Y. and F. Erdogan, Residual/thermal stresses in FGM and laminated thermal barrier coatings. International Journal of Fracture, 1994. 69(2): p. 145-165.
73. Shaw, L.L., Thermal residual stresses in plates and coatings composed of multi-layered and functionally graded materials. Composites Part B: Engineering, 1998. 29(3): p. 199-210.
74. Williamson, R., B. Rabin, and J. Drake, Finite element analysis of thermal residual stresses at graded ceramic-metal interfaces. Part I. Model description and geometrical effects. Journal of Applied Physics, 1993. 74(2): p. 1310-1320.

75. Kim, J.-H. and G.H. Paulino, An accurate scheme for mixed-mode fracture analysis of functionally graded materials using the interaction integral and micromechanics models. International Journal for Numerical Methods in Engineering, 2003. 58(10): p. 1457-1497.
76. Zuiker, J.R., Functionally graded materials: choice of micromechanics model and limitations in property variation. Composites Engineering, 1995. 5(7): p. 807-819.
77. Yin, H.M., L.Z. Sun, and G.H. Paulino, Micromechanics-based elastic model for functionally graded materials with particle interactions. Acta Maetialia 2004. 52: p. 3535-3543.
78. Hiroshi, H. and T. Minoru, Equivalent inclusion method for steady state heat conduction in composites. International Journal of Engineering Science, 1986. 24(7): p. 1159-1172.
79. Jha, D., T. Kant, and R. Singh, A critical review of recent research on functionally graded plates. Composite Structures, 2013. 96: p. 833-849.
80. Birman, V. and L.W. Byrd, Modeling and analysis of functionally graded materials and structures. Applied Mechanics Reviews, 2007. 60(5): p. 195-216.
81. Markworth, A., K. Ramesh, and W. Parks Jr, Modelling studies applied to functionally graded materials. Journal of Materials Science, 1995. 30(9): p. 2183-2193.
82. Muliana, A.H., A micromechanical model for predicting thermal properties and thermo-viscoelastic responses of functionally graded materials. International Journal of Solids and Structures, 2009. 46(9): p. 1911-1924.
83. Anthoine, A., Second-order homogenisation of functionally graded materials. International Journal of Solids and Structures, 2010. 47(11): p. 1477-1489.
84. Reiter, T., G.J. Dvorak, and V. Tvergaard, Micromechanical models for graded composite materials. J. Mech. Phys. Solids, 1997. 45(8): p. 1271-1302.
85. Mori, T. and K. Tanaka, Average stress in matrix and average elastic energy of materials with misfitting inclusions. Acta Metallurgica, 1973. 21: p. 571-574.
86. Reiter, T. and G.J. Dvorak, Micromechanical models for graded composite materials: II. thermomechanical loading. J. Mech. Phys. Solids, 1998. 45(9): p. 1655-1673.
87. Grujicic, M. and Y. Zhang, Determination of effective elastic properties of functionally graded materials using Voronoi cell finite element method. Materials Science and Engineering, 1998. A251: p. 64-76.
88. Ma, J., Z. He, and G. Tan, Fabrication and characterization of Ti-TiB2 functionally graded material system. Metallurgical and Materials Transactions A, 2002. 33(3): p. 681-685.
89. Cubberly, W.H., J.R. Davis, and K. Mills, Metals Handbook: Nonferrons Alloys and Pure Metals. Properties and Selection. 1979: American Soc. for Metals.
90. Munro, R.G., Material properties of titanium diboride. Journal of Research of the National Institute of Standards and Technology, 2000. 105(5): p. 709-720.
91. Wiley, D., W. Manning, and O. Hunter, Elastic properties of polycrystalline TiB 2, ZrB 2 and HfB 2 from room temperature to 1300 K. Journal of the Less Common Metals, 1969. 18(2): p. 149-157.
92. Parameswaran, V. and A. Shukla, Processing and characterization of a model functionally gradient material. J. Mater. Sci., 2000. 35: p. 21-29.
93. Zhai, P., et al., Ceramic transaction: functionally gradient materials. American Ceramic Society, Westerville, OH, 1993: p. 34.

94. Grujicic, M. and Y. Zhang, Determination of effective elastic properties of functionally graded materials using Voronoi cell finite element method. Materials Science and Engineering: A, 1998. 251(1): p. 64-76.
95. Shen, H. and L. Brinson, Finite element modeling of porous titanium. International Journal of Solids and Structures, 2007. 44(1): p. 320-335.
96. Wong, C.P. and R.S. Bollampally, Thermal Conductivity, Elastic Modulus, and Coefficient of Thermal Expansion of Polymer Composites Filled with Ceramic Particles for Electronic Packaging. Journal of Applied Polymer Science, 1999. 74: p. 3396-3403.
97. Hashin, Z. and S.A. Shtrikman, A variational approach to the theory of the elastic behavior of polycrystals. Journal of the Mechanics and Physics of Solids, 1963. 20: p. 343-352.
98. Ishibashi, H., et al., Characterization of Mo-SiO2 functionally graded materials. Metallurgical and Materials Transactions A, 2000. 31A: p. 299-308.
99. Yin, H.M., et al., Micromechanics-based thermoelastic model for functionally graded particulate materials with particle interactions. Journal of the Mechanics and Physics of Solids, 2007. 55: p. 132-160.
100. Neubrand, A., et al., Residual stresses in functionally graded plates. Journal of Materials Research, 2002. 17(11): p. 2912-2920.
101. Khor, K.A. and Y.W. Gu, Thermal properties of plasma-sprayed functionally graded thermal barrier coatings. Thin Solid Films, 2000. 372: p. 104-113.
102. Yin, H.M., et al., Effective thermal conductivity of two-phase functionally graded particulate composites. Journal of Applied Physics, 2005. 98.
103. Sanchez-Herencia, A.J. and R.M.J.R. Jurado, Electrical transport properties in zirconia/alumina functionally graded materials. Journal of the European Ceramic Society, 2000. 20: p. 1611-1620.
104. Scheffler, M. and P. Colombo, Cellular ceramics: structure, manufacturing, properties and applications. 2006: John Wiley & Sons.
105. Ju, J. and K. Tseng, Effective elastoplastic behavior of two-phase ductile matrix composites: a micromechanical framework. International Journal of Solids and Structures, 1996. 33(29): p. 4267-4291.
106. Touloukian, Y.S. Thermophysical Properties of Materials. in IFI/Plenum. . 1973.
107. Nemat-Alla, M., K.I. Ahmed, and I. Hassab-Allah, Elastic–plastic analysis of two-dimensional functionally graded materials under thermal loading. International Journal of solids and Structures, 2009. 46(14): p. 2774-2786.
108. Moran, M.J., et al., Fundamentals of engineering thermodynamics. 2010: John Wiley & Sons.
109. Ho, S.-Y., et al., FGM (Functionally Graded Material) Thermal Barrier Coatings for Hypersonic Structures-Design and Thermal Structural Analysis. 2007, DTIC Document.
110. Lee, W.Y., et al., Concept of functionally graded materials for advanced thermal barrier coating applications. Journal of the American Ceramic Society, 1996. 79(12): p. 3003-3012.
111. White, M.E. and W.R. Price, Affordable hypersonic missiles for long-range precision strike. Johns Hopkins APL technical digest, 1999. 20(3): p. 415.
112. Hunt, J., et al., Performance Potential and Research Needs of a Hypersonic, Airbreathing, Lifting Missile Concept. Journal of Aircraft, 1979. 16(10): p. 666-673.
113. Exelis. Solutions. 2015 May 20]; Available from: http://www.exelisinc.com/solutions.

114. Coesa, U., Standard Atmosphere 1976. US Government Printing Office, Washington, DC, 1976.
115. Dassault Systemes, Abaqus 6.12 User Subroutines Reference Manual, in Providence, Rhode Island. 2012.
116. Witeof, Z.D., Boundary Layer in Hypersonic Flow, P.D. Deierling, Editor. 2015.
117. Anderson, J.D., Hypersonic and high temperature gas dynamics. 2000: AIAA.
118. Riley, Z.B., et al., Characterization of Structural Response to Hypersonic Boundary Layer Transition, in 56th AIAA/ASCE/AHS/ASC Structures, Structural Dynamics, and Materials Conference. 2015: Kissimmee, FL. p. 1-16.
119. Wadhams, T.P., et al., Ground Test Studies of teh HIFiRE-1 Transition Experiment Part 1: Experimental Results. Journal of Spacecraft and Rockets, 2008. 45(6): p. 1134-1148.
120. Franko, K.J. and S.K. Lele, Breakdown mechanisms and heat transfer overshoot in hypersonic zero pressure gradient boundary layers. Journal of Fluid Mechanics, 2013. 730: p. 491-532.
121. Nielsen, H.B., S.N. Lophaven, and J. Søndergaard, A matlab kriging toolbox.
122. Munro, R.G., Evaluated Material Properties for a Sintered alpha-Alumina. Journal of the American Ceramic Society, 1997. 80(8): p. 1919-1928.
123. Wachtman, J.B., W.R. Cannon, and M.J. Matthewson, Mechanical properties of ceramics. 2009: John Wiley & Sons.